Laboratory models of geophysical flows:

lava domes on slopes

and

wind-driven convection at ocean fronts

David Osmond

A thesis submitted for the degree of

Doctor of Philosophy

The Australian National University.

Research School of Earth Sciences

May 2003

Typeset in Computer Modern by TEX and LATEX 2ε.

Except where otherwise indicated, this thesis is my own original work.

9 October 2003

Acknowledgements

This thesis would not have been possible without the advice and support of many people. First and foremost, I must thank my supervisor, Prof. Ross Griffiths, for his advice and support throughout this study. Whenever it seemed as if my experiments or results were not leading anywhere, Ross's insightful advice delivered through kind words could always be counted on to bring things back on track. I was also very lucky to have the support of Dr Ross Kerr, Dr Graham Hughes, Dr Andrew Kiss and Emer. Prof. Stewart Turner. Regardless of whether I needed help in understanding or correcting my experiments, theory, grammar or getting back into my office after locking myself out, there was always someone available to help out, and to do so with enthusiasm.

Many thanks to Aaron Lyman, Andrew Kiss, Mum and particularly Ross Kerr for their help with proof reading. Thank you to Xavier Chavanne, who conducted preliminary experimental work which paved the route to the rotating tank experiments presented in this thesis. Tony Beazley, Chris Morgan and Derek Corrigan were also invaluable in getting the experiments working.

I am also very grateful to many of the participants at the 1999 WHOI Summer program in GFD. To my advisor George Veronis, principal lecturer William Young and director Neil Balmforth, and all the other fellows, thank you for sharing your knowledge and friendship.

Thank you to Mum, Dad, Meg, Helen, Leon, Ingrid and Gill for their support and well wishes away from the office.

Finally, I have been extremely fortunate to have spent these past years within the GFD group at the ANU. To all those people previously mentioned, as well as Mathew Wells, Julia Mullarney, Bridget Ayling, Geoff Davies, Louis Moresi, Ross Wylde-Brown and the many visitors to this group, thank you for your company and for making the work environment here that much more enjoyable.

Abstract

Part I: *A theoretical solution is presented for the static three-dimensional shape of a fluid having a finite yield strength after it is extruded slowly from a small source on an inclined plane. The solution is compared to the shapes obtained in laboratory experiments in which slurries of kaolin in polyethylene glycol wax were ejected, slowly and in small incremental volumes, onto a slope. This study is aimed at understanding the shape of highly silicic lava flows, such as large rhyolite flows which occur on steep mountain sides or on gentle slopes, and the role of a finite yield strength in governing the slow spreading and the final static shape. The results indicate that it is possible to obtain an estimate of the yield strength of a fluid which is emplaced under such circumstances, using only horizontal aspect ratios and the slope of the underlying ground.*

Part II: *A series of experiments was conducted on a rotating table in order to simulate wind driven convection at ocean density fronts. A two layer density stratification was spun so that the parabolic interface between the two layers outcropped on the lid. Anticyclonic forcing by a differentially rotating lid over short intervals of time drove an Ekman current radially inwards and across the density front. Theoretical arguments indicate that the stratification was sufficiently weak so that the standard, homogeneous Ekman layer solution applied. Measurements of the time taken for the onset of convection are found to correlate well with the non-rotating theory for the growth of the mixed region in standard Rayleigh-Taylor convection. The magnitudes of the times differ by a factor of four, indicating that the addition of rotation slowed the growing instability. Laser induced fluorescence was used to measure the density field before and after the forcing event, and empirical formulas are given for the increase in the mass and volume of mixed fluid, as well as the mixing efficiency of the convection process. The volume of mixed water increased by between 20% and 87% of the volume of the Ekman transport across the front. The convective Rossby number is found to be the most im-*

portant parameter in determining the dimensionless production of mixed water, with a decrease in the convective Rossby number leading to an increase in the production of mixed water. We believe this is due to the higher levels of vorticity which entrain more surrounding fluid into the convecting plumes for smaller convective Rossby numbers. The much weaker role of rotation in oceanic convection means that estimates of the production of mode water in the ocean can not be made with confidence.

Contents

List of Figures

List of Tables

Part I

Yield Strength Domes on Slopes

Chapter 1

Introduction

1.1 Background

Lava domes, such as the one pictured in figure 1.1, are typically $10^2 - 10^3$ m across and $10 - 10^2$ m high, and form by the effusion of very viscous magma at slow rates from a volcanic vent. There are many characteristics of these eruptions which indicate non-Newtonian behavior (Fink and Griffiths, 1998). Indeed, were the lavas Newtonian fluids and remained so as they spread, they would continue to flow until they pooled in a depression. Instead, once the extrusion of lava from the source has stopped, lava domes undergo only limited spreading and eventually reach a final size and shape. Other deviations from Newtonian behavior include fractures and slip surfaces. Most of these flow features can be explained in terms of cooling and solidification during eruption, leading to the formation of a strong crust with a finite yield strength (Fink and Griffiths, 1990, 1992; Griffiths and Fink, 1993).

For highly silicic lavas, a finite yield strength of the erupting lava before cooling may also be important in restricting the spreading (Hulme, 1974; Blake, 1990; Griffiths and Fink, 1997; Fink and Griffiths, 1998), and it is possible that in some cases the internal strength dominates the effect of cooling.

The simplest model for a yield strength fluid is the Bingham rheology, and this has often been used in the analysis of lava flows. Hulme (1974) analyzed the flow of a uniform isothermal Bingham fluid on a sloping plane, assuming the flow to be very long in the downslope direction and of constant cross-slope width. He related the flow rate to the width and depth of the flow and showed that the yield strength leads to stationary fluid (levees) along the edges of the flow. The height and width of the

Figure 1.1: An aerial view of the Medicine Lake Dalcite Flow.

levees were related to the yield strength and slope angle. In this problem the levees are characterized by a static balance, while the downslope flow rate in the centre of the channel is controlled by viscous stresses at the base of the flow.

A simpler problem is that of an axisymmetric lava dome on a horizontal surface. Blake (1990) discussed the growth of such a dome in terms of an initial regime (while the dome is very small) in which viscous stresses are important and a later regime in which those are negligible compared to the yield stress. For sufficiently small effusion rates and sufficiently large yield strengths (i.e., at Bingham numbers $B \gg 1$, where $B = \sigma_0/\eta\dot{\epsilon}$, σ_0 is the yield strength in shear, η is the plastic viscosity, and $\dot{\epsilon}$ is the shear rate (Griffiths and Fink, 1997; Griffiths, 2000)), viscous deformation at the base of the flow can be neglected, and the problem reduces to a static balance between gravity and yield strength. The (quasi-static) growth of such a dome generates a parabolic radial depth profile first derived by Nye (1952) in the context of glaciers and which appears again in Hulme's (1974) analysis of the cross-slope profile of long downslope lava flows. Blake (1990) showed that the ratio R^2/H (where R is the dome radius and H is the axial height) is constant with time as a dome enlarges. Following Hulme's calculation of yield strengths from observed levee heights, Blake argued that it is possible to derive the yield strength of the dome-forming material by comparing the height of the domes to their width.

A consistent but more complete analytical solution for the same axisymmetric domes, allowing for motion and viscous stresses, is given by Balmforth et al. (1999). They also computed numerical solutions assuming the more general Herschel-Bulkley constitutive law, which allows for both a yield strength and a power law viscosity, and they considered the effects of basal sliding.

The effects of an internal yield strength have also been studied in the case of extrusions from a small source on a horizontal base when surface cooling is important (Griffiths and Fink, 1997; Fink and Griffiths, 1998). The surface cooling and solidification gave rise to a stronger outer layer, a number of instabilities, and a marked flow asymmetry. By comparing these observations with previous flow instabilities and flow morphologies found in solidifying extrusions of viscous fluid (Fink and Griffiths, 1990, 1992; Griffiths and Fink, 1993), the above authors concluded that the internal shearing

strength had a clear influence on the types of flow instabilities and the overall shape of the dome.

Work on the shape of domes on slopes has advanced more slowly, as the absence of axial symmetry makes the analysis considerably more difficult. Lister (1992) considered the problem of purely viscous flows from a source on a sloping plane, for which he provided similarity solutions. However, it was not until Coussot and Proust (1996) and then Wilson (1998) that Hulme's (1974) work on two-dimensional flows down slopes was extended to include the constitutive equation in its full three-dimensional form. In addition to the viscous flow downslope, Coussot et al. (1996) considered the final static shape of such flows. They derived the profile of the fluid near its boundary, in any arbitrary direction relative to the downslope direction.

1.2 This thesis

In this thesis we extend the work of Coussot et al. (1996) in deriving the final static shape of yield strength fluids on slopes. By making the following assumptions, we consider perhaps the simplest model for lava domes, or any other slowly extruded yield strength material, on sloping topography. We assume that the fluid layer is thin, the effusion rate is small and yield strength dominates ($B \gg 1$), and we ignore surface cooling. In chapter 2 we formulate the theory of the problem, nondimensionalise the governing equations, and find exact and approximate analytical solutions for the dimensions of the fluid. We also find the full numerical solution of the shape of the dome. In chapter 3 we perform experiments with mixtures of polyethylene glycol wax and kaolin clay, and compare the experimental results with the theory of the previous chapter. In chapter 4, we apply the results to a real lava dome to obtain four estimates of its yield strength, discuss the solutions, and provide our concluding remarks.

Much of the work presented in these chapters has been published in the paper Osmond and Griffiths (2001).

Chapter 2

Theory

2.1 The governing equations

Let us consider a static, isothermal yield strength fluid on a gently sloping planar base, whose thickness is much less than its width or length. We assume a uniform internal yield strength σ_0 and neglect the effects of surface tension. Although the following equations are based on a static dome, the analysis should also be valid for very slowly growing domes in which the yield strength σ_0 is always much greater than viscous stresses $\eta\dot{\epsilon}$. The following derivation is similar to that shown by Coussot et al. (1996).

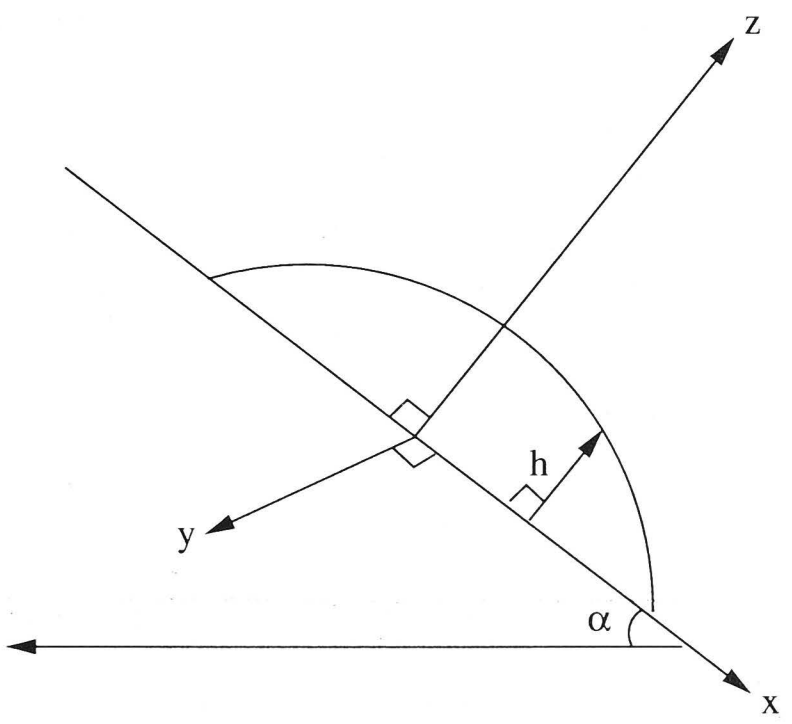

Figure 2.1: The Coordinate system. The x axis is aligned parallel to the sloping ground directed downhill, the y axis is directed across the slope, and the z axis is directed perpendicular to it. The thickness h is measured parallel to the z axis. The source is at the origin.

The magnitude of the deviatoric stress exerted by the fluid on the base and acting in a plane parallel to the base is equal to the internal yield strength. Referring to the

geometry in Figure 1, we may write this as

$$\sigma_x^2 + \sigma_y^2 = \sigma_0^2, \tag{2.1}$$

where $\sigma_x = \tau_{zx}$ and $\sigma_y = \tau_{zy}$ at $z = 0$ and where τ_{ij} is the deviatoric stress tensor. The yield strength is the maximum value that the shear stress can take in this quasi-static dome. Stress tensor theory tells us that when a shear stress component is at its maximum value, the normal deviatoric stress components are zero. Thus

$$\tau_{xx} = \tau_{yy} = \tau_{zz} = 0 \tag{2.2}$$

on the base, and we shall also assume it is zero throughout the fluid. This is equivalent to saying that the direction of maximum shear is always parallel to the base. The fluid to leading order in this approximation does not deform anywhere but at its base, where the yield strength is reached. It is also important to note that the assumption that the shear stress at the base is not less than the yield strength relates to the manner in which the dome is emplaced. The dome could not have obtained its size and shape from a small source without deformation over its entire planform area.

The force balance in the z direction is given by

$$\frac{\partial \tau_{xz}}{\partial x^*} + \frac{\partial \tau_{yz}}{\partial y^*} + \frac{\partial \tau_{zz}}{\partial z^*} - \rho g \cos\alpha - \frac{\partial P}{\partial z^*} = 0, \tag{2.3}$$

where g is gravity, ρ is the density (or density excess over the density of the environment), α is the slope of the ground from horizontal, and the asterisks indicate dimensional lengths. As the dome is much wider than it is thick, we use the thin layer approximation that gradients are greatest in the z direction. Thus the first two terms of (2.3) are negligible, the third term is zero according to (2.2), and we may integrate to yield the pressure field:

$$P = P_0 + (h^* - z^*)\rho g \cos\alpha, \tag{2.4}$$

where P_0 is the atmospheric pressure. Note that the deviation in (2.4) from atmospheric

pressure is proportional to the thickness of the dome perpendicular to the ground. This is different from the hydrostatic pressure that we associate with Newtonian fluids, which is proportional to the vertical thickness. This pressure is identical to that derived for glaciers of near constant thickness (Paterson, 1994).

In the x direction the force balance is given by

$$\frac{\partial \tau_{xx}}{\partial x^*} + \frac{\partial \tau_{yx}}{\partial y^*} + \frac{\partial \tau_{zx}}{\partial z^*} + \rho g \sin\alpha - \frac{\partial P}{\partial x^*} = 0. \tag{2.5}$$

After applying the thin layer approximation (including $\partial \tau_{zx}/\partial z^* = \sigma_x/h^*$) and using (2.2) and (2.4), (2.5) reduces to

$$\frac{\sigma_x}{h^*} + \rho g \sin\alpha - \rho g \cos\alpha \frac{\partial h^*}{\partial x^*} = 0. \tag{2.6}$$

Similarly, a force balance in the y direction yields

$$\frac{\sigma_y}{h^*} - \rho g \cos\alpha \frac{\partial h^*}{\partial y^*} = 0. \tag{2.7}$$

Combining (2.1), (2.6), and (2.7) yields

$$(g\rho\cos\alpha)^2 \left[\left(\frac{\partial h^*}{\partial x^*} - \tan\alpha \right)^2 + \left(\frac{\partial h^*}{\partial y^*} \right)^2 \right] = \left(\frac{\sigma_0}{h^*} \right)^2. \tag{2.8}$$

We nondimensionalise the slope parallel length scales by the quantity

$$L_0 = h_0 \cos\alpha / \sin^2\alpha, \tag{2.9}$$

and we nondimensionalise the slope normal length scale by the length

$$H_0 = h_0 / \sin\alpha, \tag{2.10}$$

where $h_0 = \sigma_0/(g\rho)$. Note that these scales do not correspond to actual lengths. Rather, they indicate the extent to which gravity pulls the dome downhill. If the length scale L_0 is large, then the dimensionless lengths will be small, and the dome will spread almost axisymmetrically on the slope. Large dimensionless lengths, on the other

hand, indicate that the dome spreads mainly down the slope. With these scalings, (2.8) becomes

$$\left(\frac{\partial h}{\partial x} - 1\right)^2 + \left(\frac{\partial h}{\partial y}\right)^2 = \left(\frac{1}{h}\right)^2, \tag{2.11}$$

where all lengths are now dimensionless. Equation (2.11) is identical to that derived by Coussot et al. (1996), although our origin has been chosen to coincide with the source, rather than at the limit of the upslope extent.

2.2 The downslope axis of symmetry solution

Along the $y = 0$ axis, symmetry requires $\partial h/\partial y = 0$, which leads to a solution of (2.11),

$$x = h - H + \ln\left|\frac{1-h}{1-H}\right| \tag{2.12}$$

on the downslope side of the source, where $h = H$ when $x = 0$. On the upslope side of the source the solution is

$$-x = H - h + \ln\left|\frac{1+h}{1+H}\right|. \tag{2.13}$$

The downslope and upslope extent of the flow may be found by substituting $h = 0$ into (2.12) and (2.13), giving

$$x_d = -H - \ln|1 - H|, \tag{2.14}$$

$$-x_u = H - \ln|1 + H| \tag{2.15}$$

and a total length of

$$L = -\ln|1 - H^2|. \tag{2.16}$$

There are a couple of points to notice about this solution. First, when the dimensionless thickness $H \to 1$, the length of the dome on the upslope side is finite ($-x_u \to 1 - \log 2 \approx 0.307$), whereas the length of the dome on the downslope side becomes infinite ($x_d \to \infty$). Thus there is a maximum permissible thickness of the

flow. Beyond this thickness the yield strength of the fluid is unable to support the dome on the slope in a static balance with gravity. In dimensional units the maximum thickness is $H^* = h_0/\sin\alpha$. We shall only concern ourselves with domes that can be supported in the static balance, so we assume $H < 1$.

Note also that when the slope approaches zero, the length scales L_0 and H_0 tend to infinity, and hence the dimensionless quantities H, x_d, x_u, and L tend to zero. This limiting case also applies when the fluid has a very large yield strength and when the thickness (or volume) of the dome is extremely small. For small values of any variable u, $\ln(1+u) \approx u - u^2/2$, so that (2.12) and (2.13) both reduce to the one equation:

$$|x| \approx \frac{1}{2}(H^2 - h^2), \tag{2.17}$$

or in dimensional quantities,

$$|x^*| \approx \frac{\cos\alpha}{2h_0}(H^{*2} - h^{*2}). \tag{2.18}$$

This thickness profile is consistent with the formula derived by Nye (1952) for the cross-sectional shape of a glacier on level ground, using assumptions identical to our own.

The cross-sectional shape of the dome along its axis of symmetry, given by (2.12) and (2.13), is plotted in Figure 2.2 for several values of H. Notice how the gradients of the dimensionless dome become increasingly large for smaller values of the central thickness. This results in the gradient terms in the left-hand side of (2.11) becoming much greater than one, thus dwarfing the unitary term and removing the asymmetry of the problem. Thus the domes become increasingly symmetric as $H \to 0$.

Perhaps the most striking aspect of the profiles is the discontinuity in the surface slope at the origin. This can be explained through our assumption that the stress exerted by the fluid on the ground is everywhere equal in magnitude to the internal yield strength. On the upslope side of the source the fluid has had to move upslope, and so the direction of the force that the dome exerts on the underlying ground is in an upslope direction. On the downslope side the opposite is true. In our thin layer

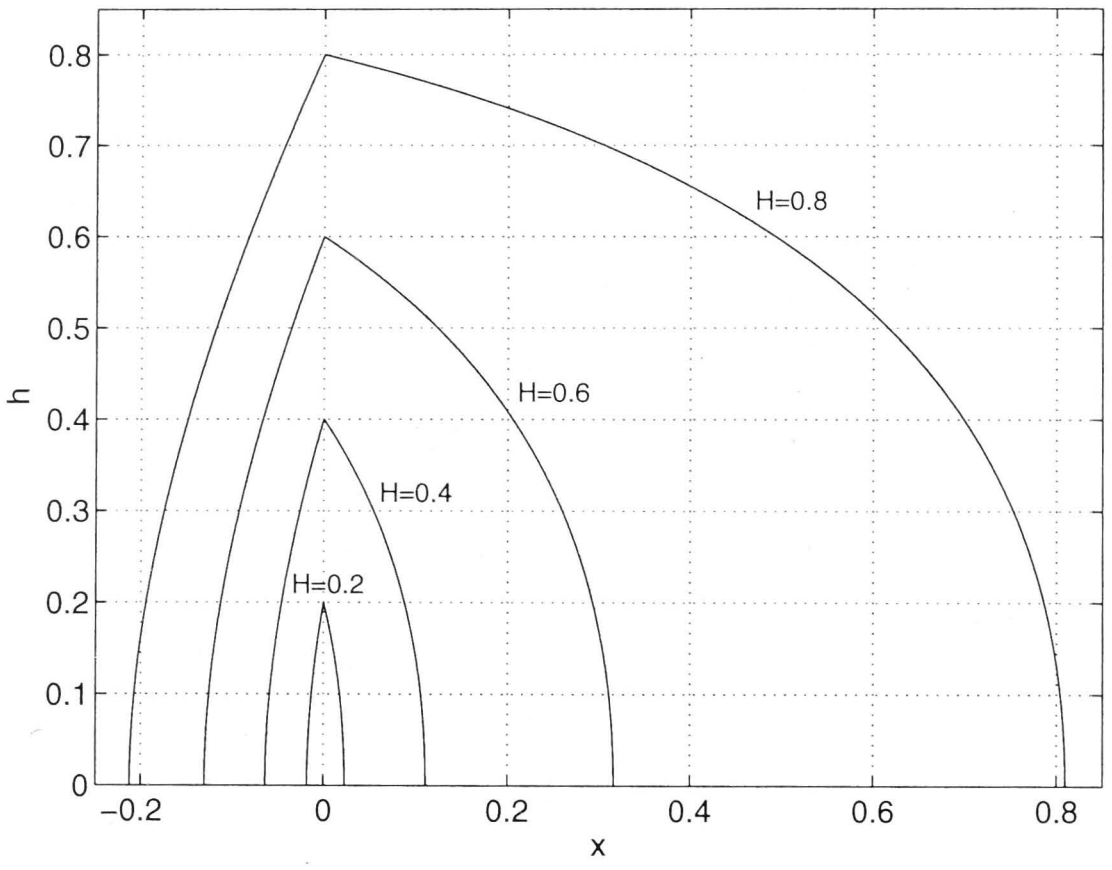

Figure 2.2: Cross-sectional shape of the dome along the upslope-downslope axis of symmetry, as a function of the thickness of the dome in dimensionless terms.

approximation one can see from (2.6) that this discontinuity in the direction of the stress acting on the ground must result from a discontinuity in the surface slope. In real life the thin layer approximation is not valid near the source, and it would be possible to obtain the required basal stress without the discontinuity in the surface slope. However, it should be noted that the appearance of the discontinuity in the surface slope is greatly enhanced by our nondimensionalization, as the aspect ratio has been deformed by a factor of $\tan\alpha$. In most cases the actual shape of the dome is much shorter and flatter than suggested in Figure 2.2.

2.3 The approximate across-slope solution

An approximate expression for the across-slope width may also be derived from (2.11). We assume $\partial h/\partial x << 1$ at the maximum width of the dome, which is valid along $x = 0$ when the dome is reasonably axisymmetric ($H \to 0$), or along some other downslope value of x when the dome is much longer than it is wide ($H \to 1$). Then (2.11) reduces to

$$1 + \left(\frac{\partial h}{\partial y}\right)^2 \approx \left(\frac{1}{h}\right)^2, \tag{2.19}$$

which has the solution

$$y \approx \pm(\sqrt{1-h^2} - \sqrt{1-H^2}), \tag{2.20}$$

where it has been assumed that the height at $y = 0$ is $h = H$ even when the maximum width is not at $x = 0$. Setting $h = 0$ into (2.20) gives an approximation to the across-slope width of the dome:

$$W \approx 2(1 - \sqrt{1-H^2}), \tag{2.21}$$

which is in agreement with equation (20) from Coussot et al. (1996). This equation offers a more accurate formula for the relationship between the width and height of a dome on a slope than the often used formula of Nye (1952), $R = H^2/2$, obtained from the horizontal ground theory.

2.4 The approximate solution for volume

Using the expressions for the cross-sectional shape of the dome along its downslope-upslope axis of symmetry, and for its width, we may deduce a scaling law for the volume:

$$\begin{aligned} V &\sim W \int_{x_d}^{x_u} h(y=0)dx \\ &\sim 2(1-\sqrt{1-H^2}) \left(\ln \left| \frac{1+H}{1-H} \right| - 2H \right). \end{aligned} \tag{2.22}$$

If we choose a scaling constant so that (2.22) becomes

$$V \approx \frac{2\pi}{5}(1-\sqrt{1-H^2}) \left(\ln \left| \frac{1+H}{1-H} \right| - 2H \right), \tag{2.23}$$

then for the case of small H, and when $\alpha = 0$, the volume is in agreement with that derived from Nye's [1952] glacial cross section,

$$V = \frac{2\pi}{15} H^5. \tag{2.24}$$

2.5 Numerical Solutions

Unlike Coussot et al. (1996), we propose that there is a unique solution to (2.11), based on the proviso that we only allow a surface slope discontinuity at the origin. We shall comment on other solutions to (2.11) which do not satisfy this condition at the end of this section.

Equation (2.11) may be solved numerically by treating it in the same way as an initial value problem, but instead of integrating forward in time, we integrate forward in θ. We recast (2.11) in polar coordinates,

$$\left(\frac{\partial h}{\partial r}\right)^2 + \left(\frac{1}{r}\frac{\partial h}{\partial \theta}\right)^2 + 1 - 2\cos\theta\,\frac{\partial h}{\partial r} + \frac{2\sin\theta}{r}\,\frac{\partial h}{\partial \theta} - \frac{1}{h^2} = 0, \tag{2.25}$$

and then solve for $\partial h/\partial\theta$:

$$\frac{\partial h}{\partial \theta} = -r\sin\theta \pm \sqrt{\frac{1}{h^2} - \left(\frac{\partial h}{\partial r} - \cos\theta\right)^2}, \tag{2.26}$$

where r and θ are defined by the usual equations, $r^2 = x^2 + y^2$ and $\theta = \arctan(y/x)$. In particular, $\theta = 0$ corresponds to the downslope direction.

Equation (2.12), with x replaced by r, is used as the initial condition, $h(r, 0)$. Equation (2.26) may then be used to solve for $h(r, \theta)$ for all θ. Since the domes are symmetric about the x axis, or $h(r, \theta) = h(r, -\theta)$, we require (2.26) to be an odd function. The first term on the right-hand side of (2.26) is odd. The second term is odd if we choose one root for positive θ and the opposite root for negative θ. We shall integrate from $\theta = 0$ toward $\theta = \pi$. Since the dome has a maximal cross section when $\theta = 0$, we require $\partial h/\partial\theta$ to be negative and thus use the negative root. Discretizing (2.26) using the forward-time-centered-space (FTCS) differencing scheme yields

$$h_{i,j+1} = h_{i,j} - r_i\Delta\theta\left(\sin\theta_j + \sqrt{1/h_{i,j}^2 - \xi^2}\right), \tag{2.27}$$

where

$$\xi = (h_{i+1,j} - h_{i-1,j})/(2\Delta r) - \cos\theta_j. \tag{2.28}$$

Numerical instabilities arise in this scheme, and it is necessary to perform some smoothing after each step in θ by averaging neighbouring terms. The accuracy of the method was verified by comparing the numerical result to the theoretical solution for $h(r, \pi)$ given by (2.13). It was found that the scheme converged best when there were $\sim$ 16-32 times as many steps in θ than the number of grid points in r.

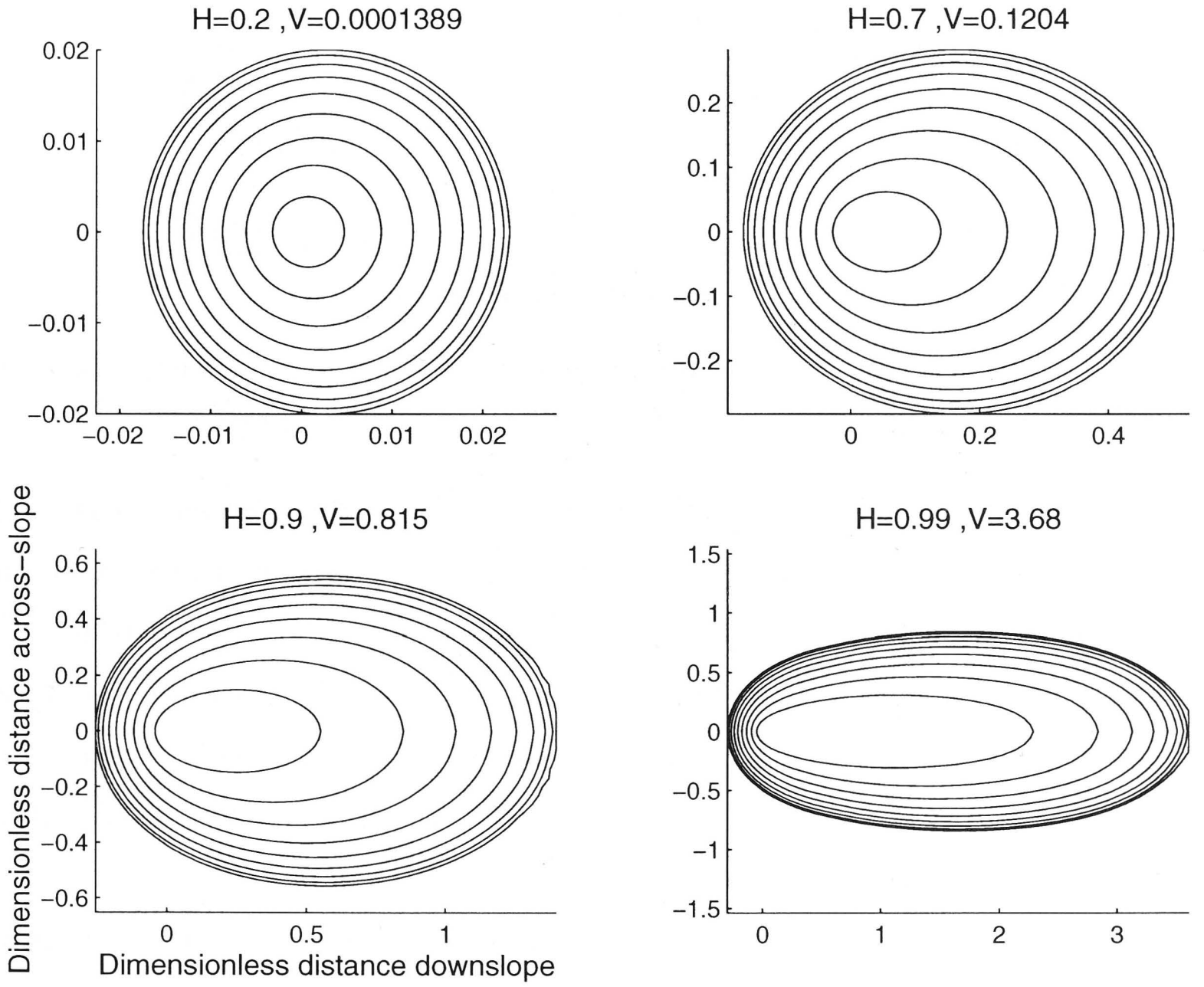

Figure 2.3: Contour plots of the numerical solution to equation (2.11), for four values of the central thickness H. Note the change of the scale of the axis between the various plots.

Results of the numerical integrations, with 8192 steps in θ and 256 steps in r, showing the three-dimensional topography, are given in Figure 2.3 for various dimensionless values of the central thickness H. At this resolution the numerical solution for $h(r, \pi)$ was visually indistinguishable from the theoretical solution. Figure 2.4 shows a composite plot of the footprints ($h = 0$) of nine domes, with values of H ranging from 0.1 to 0.9. Figure 2.4 is similar to Figure 2.2, except instead of showing a vertical cross section, it shows a horizontal cross section at the base. As in Figure 2.2, for smaller

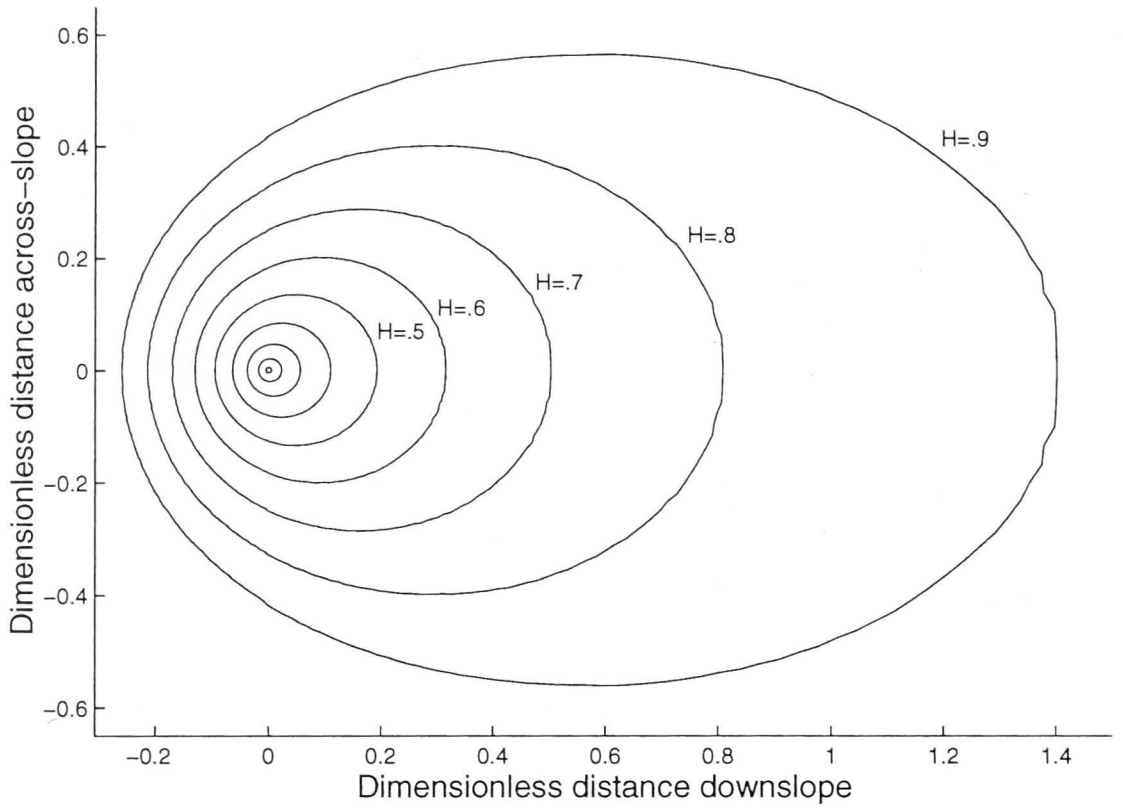

Figure 2.4: The footprint of the domes with heights $H = 0.1 - 0.9$, in steps of 0.1. This can be interpreted as the time evolution of the horizontal extent of a very slowly growing dome.

values of H, the dome is very closely centered on the origin, however, as $H \to 1$, the dome grows increasingly elongated in the downslope direction. In this limit, the across-slope half width approaches 1, and the upslope spreading $1 - \ln 2 \approx 0.307$.

The numerical solutions also provide a value for the volume of each dome, shown for the examples in Figure 2.3. These computed volumes are plotted in Figure 2.5 as a function of H and compared to the approximate theoretical result of (2.23). There is an excellent agreement between the theory and the numerical results.

At the beginning of this section we mentioned that there were other solutions to (2.11), but which involve surface discontinuities at places other than the origin. In particular, if we took any of the solutions plotted in Figure 2.3, sliced them down the middle along the $y = 0$ axis of symmetry, pulled each half apart by any arbitrary distance y_0, and then filled in the gap with the axis of symmetry solution given by (2.12) and (2.13), then the resultant shape would still satisfy (2.11). However, these solutions would have discontinuities in the surface slope along the y axis from $y = -y_0$ to $y = y_0$. We rationalized earlier that this surface discontinuity was required to provide the stress at the base which was consistent with the direction that the fluid had moved from the source to get to its current position. Thus we now argue that the solution described above is only valid if the dome was emplaced by a line source of fluid, extending along

the y axis from $y = -y_0$ to $y = y_0$. Similarly, the numerical solutions we have derived are only valid for point sources, or in more practical terms, where the horizontal extent of the source is negligible compared to the horizontal extent of the dome.

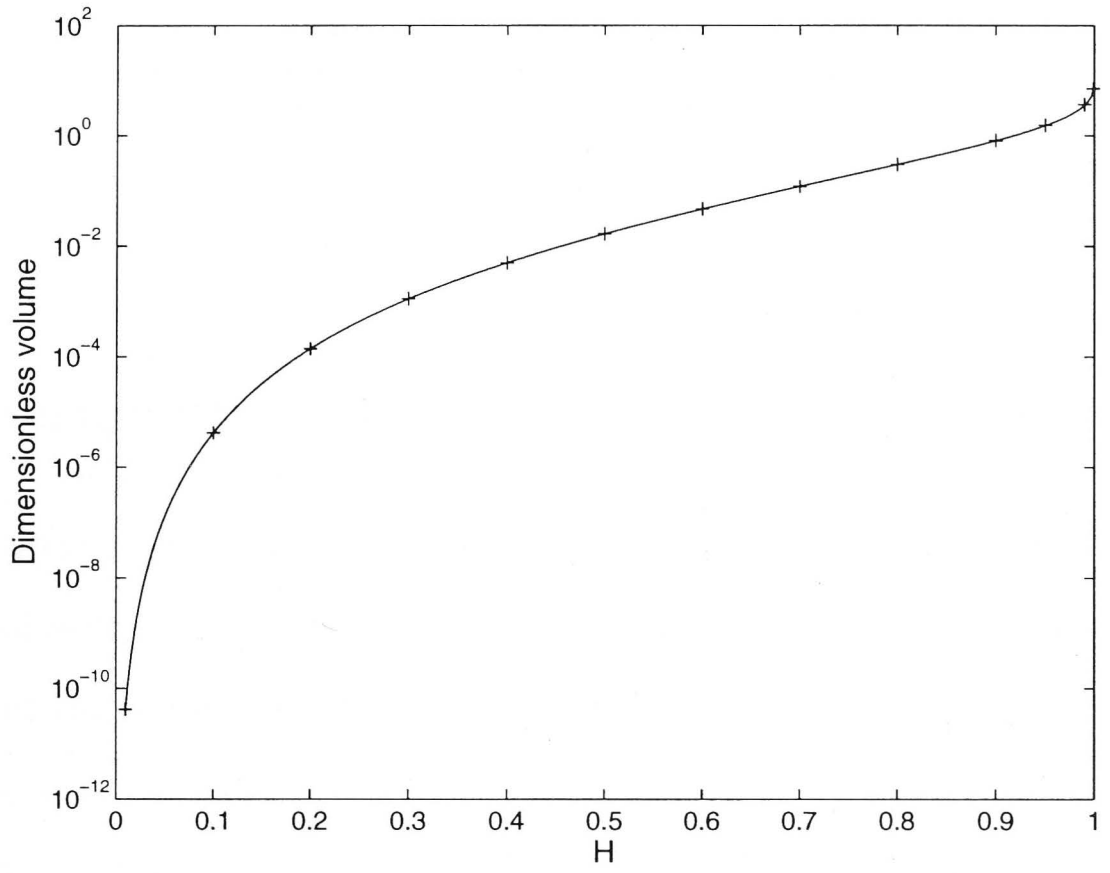

Figure 2.5: The numerical (crosses) and theoretical (line) volumes of domes as a function of their dimensionless thickness H. The error estimates for the numerical results are of order 1%, and are too small to be visible in this plot.

Chapter 3

Experimental method and results

3.1 Experimental set-up and yield strength calculation

Experiments designed to test the theoretical results were carried out using a slurry made from polyethylene glycol (PEG600) wax and kaolin clay. The clay particles have a similar effect on the rheology of the slurry as crystals have on the rheology of lava, both creating a finite yield strength. The stress-strain relationships of slurries have been extensively studied (Hulme, 1974; Blake, 1990; Griffiths and Fink, 1997) and have been found to approximate Bingham fluids. We only require the slurry to have a nonzero yield strength, and the first part of our experiment is designed to verify and evaluate this and also to show that it is the yield strength which governs the static shape of the produced domes.

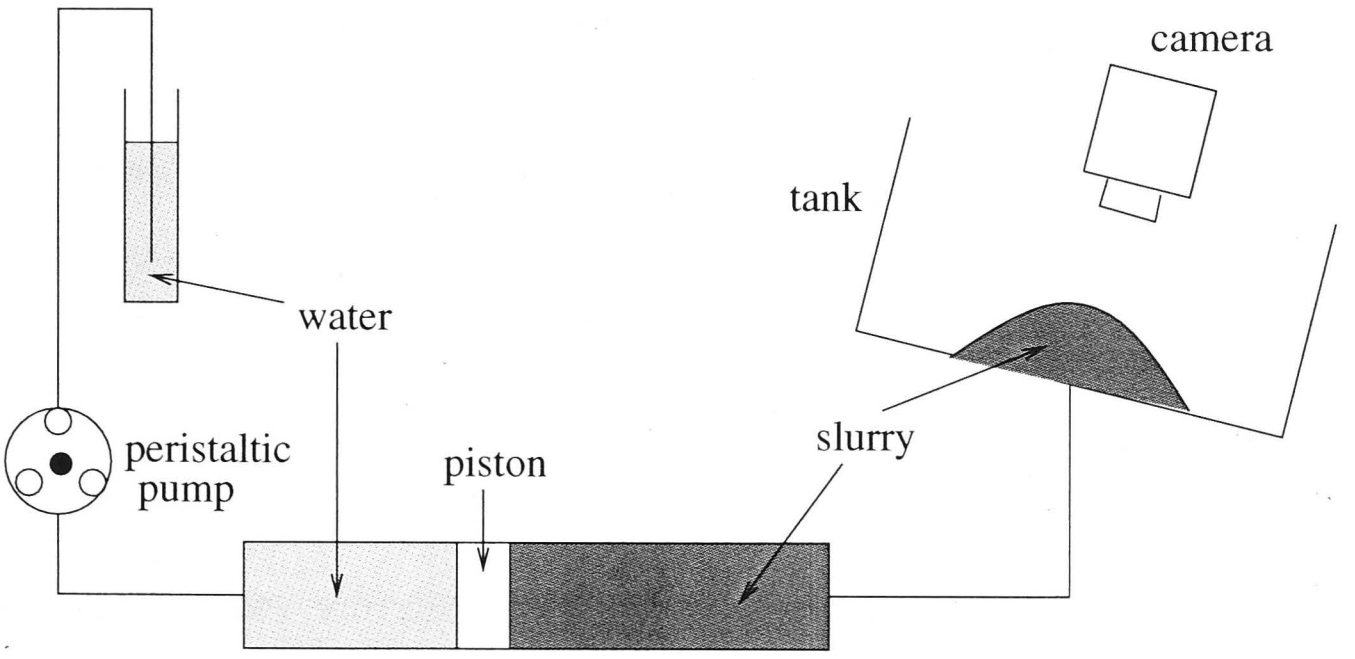

Figure 3.1: Experimental setup. Water is pumped into a cylinder forcing the piston to eject the slurry out through a tube and through a hole into the base of a tank.

The experimental setup is shown in Figure 3.1. In the control experiments for each

batch of slurry the tank was positioned so that its floor was horizontal and a known quantity of the slurry was very slowly injected (volume flux rates of $q \approx 15$ cm^3 min^{-1}) at room temperature through a hole of diameter 10 mm in the base of the tank. When the desired volume had been injected, pumping was ceased, and after a couple of minutes of waiting to ensure the termination of any residual motion, the average radius of the slurry dome was recorded. This process was repeated for about a dozen different volumes. The yield strength of the fluid, or rather the length scale $h_0 = \sigma_0/(g\rho)$, was then calculated using (2.24) and (2.17), after setting $h = 0$ and replacing $|x|$ with R, where R is the maximum radius of the dome. After converting to dimensional quantities the desired equation becomes

$$h_0 = \frac{\sigma_0}{g\rho} = \left(\frac{15}{8\pi C}\right)^2 \frac{V^2}{R^5}, \tag{3.1}$$

where $C = \sqrt{2}$. This method of evaluating the yield strength is preferred to that determined by using a viscometer as the stress can vary very rapidly and nonlinearly at very small strain rates, making it difficult to interpolate to the appropriate stress value at zero strain rate.

If the shape of the slurry dome is governed by its yield strength, then we would expect the calculated value of h_0 to be independent of the dome volume. Figure 3.2 shows a typical plot of h_0 versus volume for a given slurry. As with most of the mixtures we used, the calculated yield strength tends to decrease with volume. However, the rate of decrease slows as the volume increases, and to within the uncertainty of each calculation it converges to a final value once the volume exceeds ~ 1000 cm^3.

3.2 Results

Once a value of the yield strength for a particular mixture was determined, we repeated the experiment in a tank with a sloping base, recording the volume injected, dome width, upslope length, and downslope length. A list of experiments with their slurry properties is given in Table 3.1, while figures 3.3 and 3.4 shows photographs of some domes. After nondimensionalizing the measured horizontal lengths by L_0 and

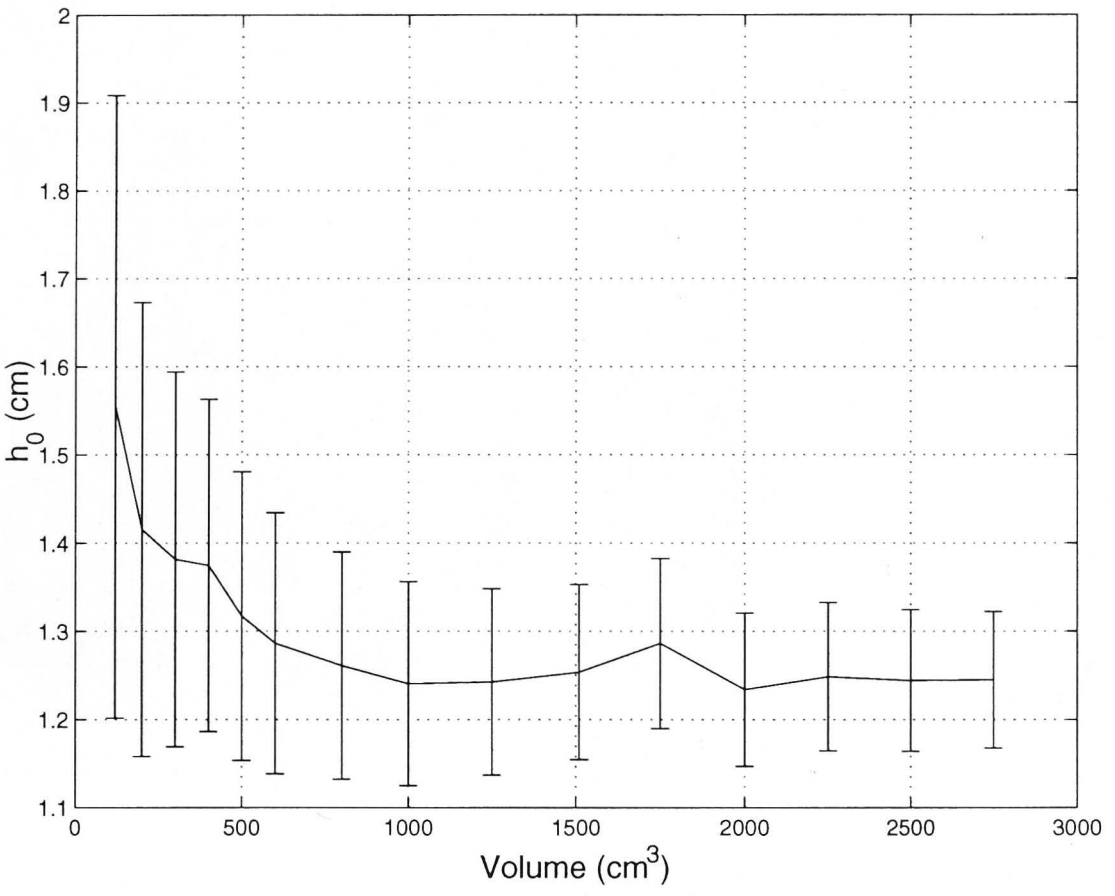

Figure 3.2: A typical plot of the calculated value of the height scale h_0 (3.1) for various volumes of a slurry dome (from experiment a0). The error bars are based on the uncertainty in the measurement of the dome radii.

Table 3.1: Slurry properties and conditions for each experiment

Experiment	PEG:Kaolin	σ_0 Pa	h_0 cm	Slope ^{o}	Vol. Range cm^3	No. of Measurements
a0	3:2	175 ± 11	$1.24 \pm .08$	0	120-2750	15
a8	3:2	175 ± 11	$1.24 \pm .08$	8	100-2500	13
a10	3:2	175 ± 11	$1.24 \pm .08$	10	100-2500	13
a12	3:2	175 ± 11	$1.24 \pm .08$	12	100-1500	10
a20	3:2	175 ± 11	$1.24 \pm .08$	20	100-1502	9
a24	3:2	175 ± 11	$1.24 \pm .08$	24	100-1000	9
b0	8:5	131 ± 11	$.94 \pm .08$	0	100-2500	13
b8	8:5	131 ± 11	$.94 \pm .08$	8	100-2250	12
b10	8:5	131 ± 11	$.94 \pm .08$	10	100-2250	12
b12	8:5	131 ± 11	$.94 \pm .08$	12	100-1750	10
b15	8:5	131 ± 11	$.94 \pm .08$	15	112-1506	9
b18	8:5	131 ± 11	$.94 \pm .08$	18	100-1500	9
c0	5:3	29 ± 2	$.22 \pm .02$	0	50-2735	13
c3	5:3	29 ± 2	$.22 \pm .02$	3	100-2000	11
c4	5:3	29 ± 2	$.22 \pm .02$	4	100-1750	9
c5	5:3	29 ± 2	$.22 \pm .02$	5	100-1300	9

the volume by $L_0^2 H_0$, we then compared the results to the corresponding theoretical solutions. The results are shown in figure 3.5.

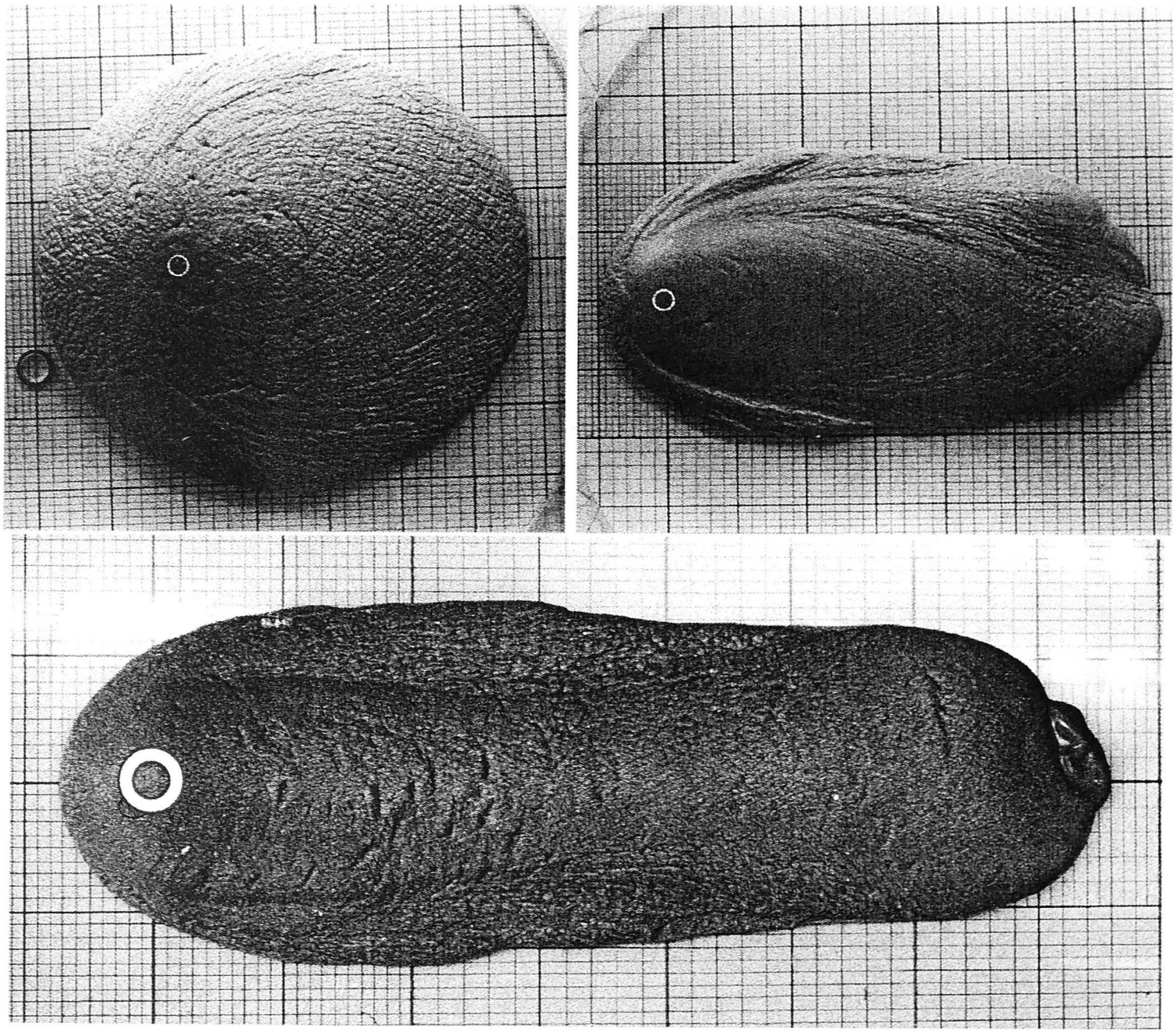

Figure 3.3: Three slurry domes on a base that slopes downwards to the right. The dome on the top left is from experiment a10, which was run on a tank slope of 10^o. It has a dimensionless volume of 0.06. Visible in this photograph are two sets of slip planes which spiral out from the source in opposite directions on the free surface of the slurry. The dome on the top right is from experiment b18, which was conducted on a tank slope of 18^o. It has a dimensionless volume of 3.7. The slip planes are also visible in this photograph, becoming more highly distinct as they near the sides of the dome, as they did in all experiments with large dimensionless volumes. The third dome is from experiment a24, was conducted on a slope of 24^o, and has a dimensionless volume of 5.9. The white circles indicate the location of the source. The grid scale on the base indicate 1 centimetre and 5 centimetre intervals.

In general, there is a good match between the experiments and theory. After nondimensionalizing, the experiments reduce convincingly to a single curve, and this closely matches the theory. The domes are slightly wider than predicted, particularly at large dimensionless volumes, where the width sometimes exceeds the theoretical limit. The agreement with the length is good. The one measure which has large discrepancies

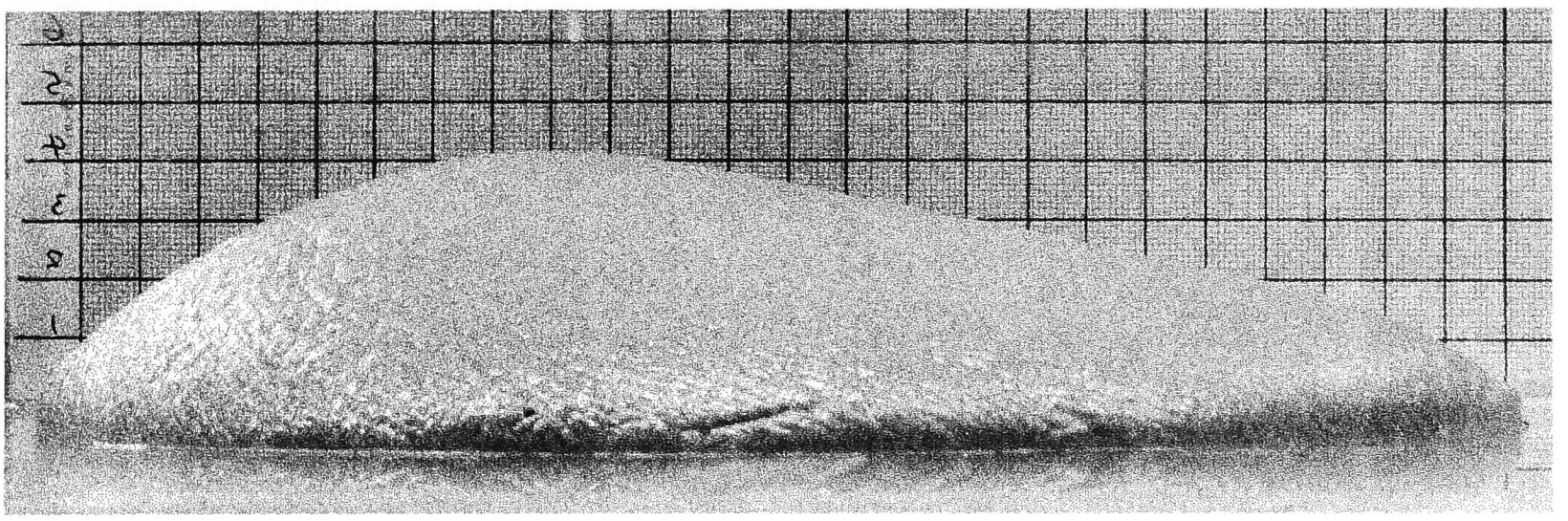

Figure 3.4: A side view of a slurry dome, from experiment b10. The base slopes downwards to the right at an angle of 10°. The heavy grid lines in the background are drawn at 1 cm intervals.

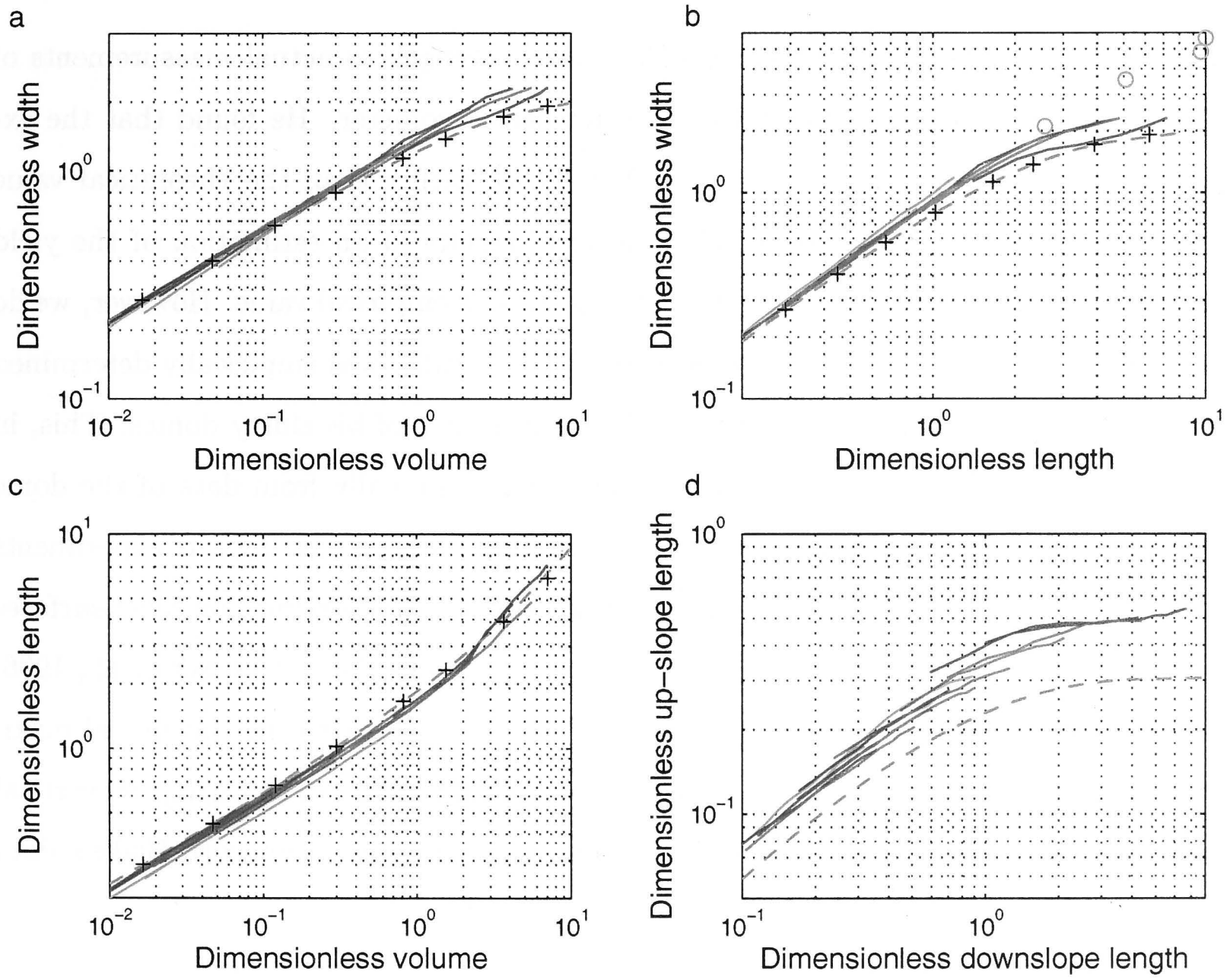

Figure 3.5: (a-d) A comparison of numerical (black crosses), theoretical (red dashed lines) and experimental (solid lines) results for domes based on the experimental conditions. Experimental results taken from Figure 3 of Coussot et al. (1996) are also shown in Figure 9b (cyan circles). The experimental lines are coloured according to PEG:Kaolin ratio. The blue, green and magenta lines correspond to PEG ratios of 3:2, 8:5 and 5:3 respectively.

between theory and experiment is the distance the dome spreads upslope. However, in many of our measurements this distance is comparable to the dome thickness, so that our use of the thin layer approximation is not accurate for that region of the dome.

Despite the apparent agreement between our experimental results and theory, we note that some caution should be taken, owing to an apparent disagreement with a previous study. In (3.1) we derived a method of calculating the dimensional length scale h_0 and hence yield strength of a dome on level ground using its volume and radius. Blake (1990) used a similar expression using height and radius,

$$h_0 = \frac{H^2}{C^2 R}, \tag{3.2}$$

and compared those deduced values of the yield strength to actual measurements of the yield strength made using a Haake Rotovisko viscometer. He found that the experiments suggested a value of $C = 1.76 \pm 0.043$, rather than the theoretical value of $C = \sqrt{2} \approx 1.41$. The theoretical value of C results in an estimation of the yield strength 55% larger than that gained by using Blake's empirical value. However, we do not use Blake's value, for two reasons. First, Blake's value was empirically determined from experimental data of the central height and radius of his slurry domes. This, in practice, would differ from a constant determined empirically from data of the dome volume and radius. Second, we must be consistent when comparing our experiments to theory. We should not use one constant when considering domes on level surfaces and another for domes on slopes. Previous studies (Hulme, 1974; Coussot et al., 1996; Coussot and Proust, 1996) have indicated a good agreement with the theoretical maximum thickness of static domes, $h_0/\sin\alpha$, so we should be wary of changing the vertical length scale used in our general theory in order to force agreement with Blake's data in the level case.

In Figure 3.5b, we have plotted results from the experiments carried out by Coussot et al. (1996). Their flows are considerably wider than those our theory predicts, though some of that disagreement may be explained by their method of spilling the slurry onto the inclined plane from above. While they did not report figures for the volume flux or the width of the spilling fluid, it is likely that their experiments involved significantly

larger velocities than those in our domes and a greater source width than our 10 mm diameter injection tube. These differences would result in their domes having a larger region surrounding the source where viscous forces contribute to the stress during flow emplacement.

Chapter 4

Application and conclusions

4.1 Determining the yield strength of real lava domes

A major aim of this study was to create new methods of determining the yield strength of some simple lava flows by considering only their final static shape. Having derived a theory of their shape in chapter 2 and finding good agreement between this theory and experimental results in chapter 3, we are now in a position to do so. But first, let us revisit an existing formula with which our new methods will be compared.

Hulme (1974) first derived the maximum thickness of a static yield strength fluid as $H^*_{\max} = h_0 / \sin\alpha$. This can be rearranged to provide a formula for the yield strength

$$\sigma_A = \rho g H^*_{\max} \sin\alpha, \tag{4.1}$$

and this has been found to provide reasonable estimates of the yield strength in several studies (Hulme, 1974; Coussot et al., 1996; Coussot and Proust, 1996). This formula is recommended if the vertical thickness can be measured, and is found to satisfy $\frac{\partial h}{\partial x} \ll \tan\alpha$. It may also provide a lower limit for the yield strength where this condition is not met.

Equation 4.1 uses only the thickness of the dome, and assumes the dome is close to its maximal thickness. An equivalent formula may be obtained by assuming the dome is close to its maximal width. According to equation (2.21), $W_{\max} = 2$. Expressed in dimensionless quantities, it can be rearranged to provide the yield strength

$$\sigma_B = \frac{\rho g W^*_{\max} \sin^2\alpha}{2\cos\alpha}. \tag{4.2}$$

Note that the quantities $H^*_{\max}$ and $W^*_{\max}$ do not represent the maximum height and width measured from a particular dome. Rather they represent the maximum height and width theoretically achievable by the dome subject to the assumptions made by our theory. The dome may not have grown to a sufficient size for it to have neared these theoretical limits. Alternatively, if the relevant assumptions did not hold during the dome's formation, then these limits may have been exceeded. For example, a bulbous lobe protruding from a lave dome should not be included in a measurement of its width or height as its formation clearly indicates that our assumption of uniform rheology is invalid. This is particularly clear from the results of Coussot et al. (1996) shown in figure 3.5. These domes spread to widths much greater than the theoretical limit, possibly due to viscous forces being appreciable during the dome formations. In contrast, the theoretical height of a yield strength dome cannot be exceeded without some other non-Newtonian behaviour applying. For this reason, estimating the yield strength of a dome from its height alone is much preferred to using its width alone.

If a dome has not spread to near its theoretical maximum height or width, then equations (4.1) and (4.2) will not provide a good estimate of the yield strength. This may be overcome by using both dimensions. Rearranging (2.21) and expressing in dimensional quantities yields

$$\sigma_C = \frac{\rho g H^{*2} \cos\alpha}{W^*} \left[1 + \frac{W^{*2} \tan^2\alpha}{4H^{*2}}\right]. \tag{4.3}$$

However, it is not always easy to obtain a value for the thickness of a lava dome. A more practical alternative is to estimate the yield strength using the two lateral dimensions. These are usually the easiest dimensions to obtain for a lava flow because they are visible in aerial photographs. Figure 4.1 shows how our theoretical and experimental results may be used to estimate the yield strength without knowing the thickness of the dome. By calculating the width to length ratio of a real lava dome, one can use the graph (Figure 4.1a) to predict the dome's dimensionless length. The scatter in the experimental curves and the difference between the experimental and the theoretical curves provide an estimate of the precision of this length. By comparing the measured length to the predicted dimensionless length, and using estimates of the ground slope

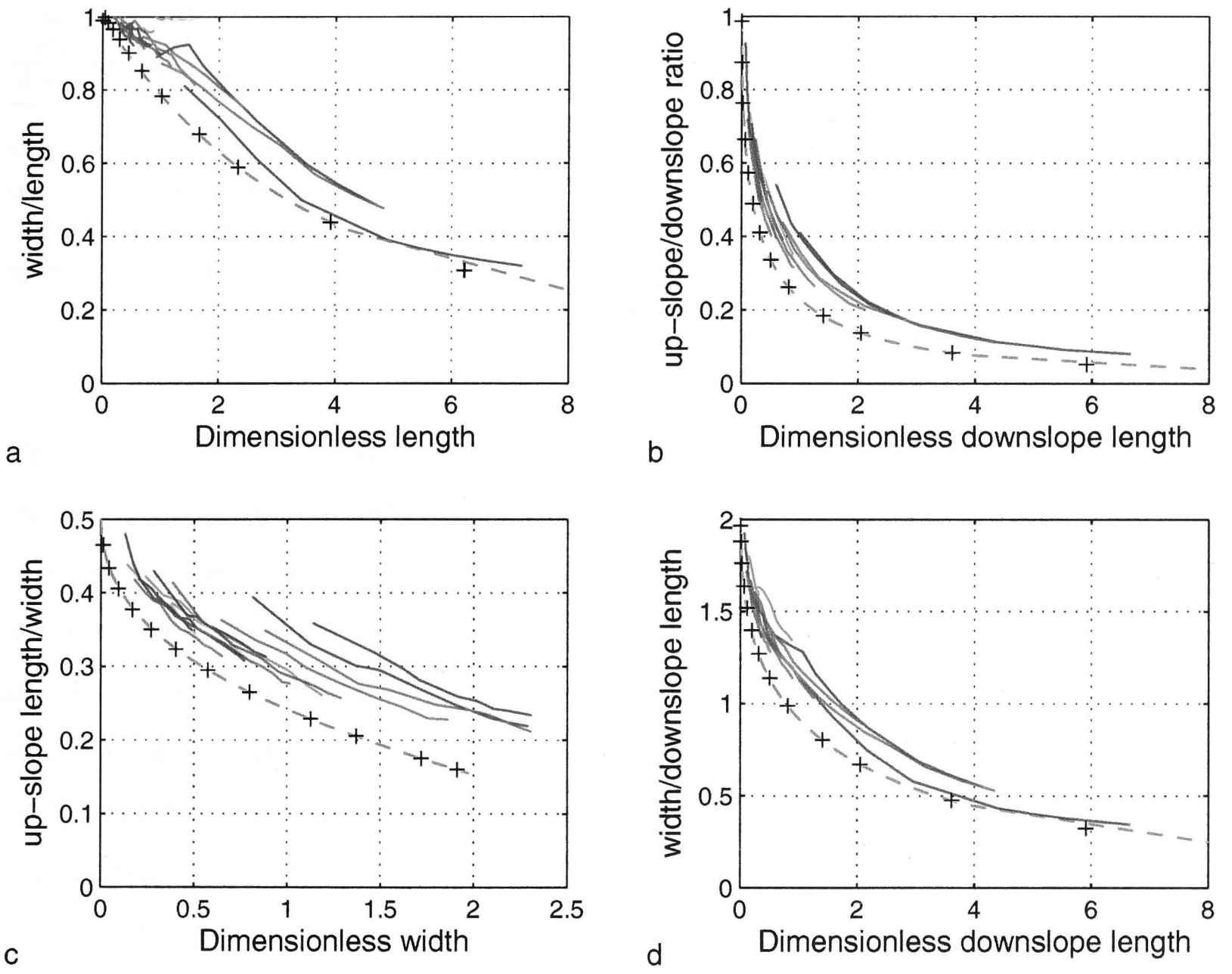

Figure 4.1: (a-d) A comparison of experimental (solid lines), numerical (black crosses) and theoretical (red dashed lines) results for the ratio of various horizontal length scales against corresponding dimensionless lengths. The experimental lines are coloured according to PEG:Kaolin ratio. The blue, green and magenta lines correspond to PEG ratios of 3:2, 8:5 and 5:3 respectively.

and lava density, it is possible to determine the yield strength of the lava using the formula

$$\sigma_D = \frac{\rho g L^* \sin^2 \alpha}{L \cos \alpha}. \tag{4.4}$$

Table 4.1 contains the physical properties of the Medicine Lake Dacite Flow, from Lyman et al. (2002). Also displayed in this table are four values of the yield strength, determined using equations (4.1)-(4.4). To within the uncertainty specified, the results are in very good agreement.

Since the dome in question is only 50% longer than it is wide, and the quoted height was obtained from a series of measurements of its thickness near its perimeter, the value of σ_A is likely to be a lower limit of the true yield strength. A similar argument could be

Slope °	Density kg/m^3	Height m	Length m	Width m	σ_A kPa	σ_B kPa	σ_C kPa	σ_D kPa
1.97	2500	27 ± 8	2100 ± 100	1400 ± 100	23 ± 7	20 ± 2	23 ± 13	30 ± 8

Table 4.1: Properties of the Medicine Lake Dacite Flow, as pictured in figure 1.1, together with four different calculations of the yield strength. Height is the only length scale used to calculate σ_A from equation (4.1), while the width is the only length used to calculate σ_B from equation (4.2). Equation (4.3) uses both the height and the width to determine σ_C, while σ_D is based on the width to length ratio, figure 4.1(a) and equation (4.4). The properties of the dome were obtained from Lyman et al. (2002)

applied to the value σ_B obtained from the dome's width, though for reasons mentioned previously, we believe the dome height provides a more reliable indicator of the yield strength's lower limit. The uncertainty in the value σ_b is also greatly underestimated as we have not included the uncertainty in the slope angle. The value of σ_C was obtained using the dome's thickness and width through equation (4.3). In the past, this has sometimes been attempted by using Blake's (1990) formula for the width (diameter) of a lava dome on level ground, which gives $\sigma_0 = \frac{2}{1.76^2}\rho g H^{*2}/W^* = 8 \pm 5$ kPa. Given the good agreement between the other four values, it is clear that it is preferable to use a formula based upon a theory that includes the influence of slope on the width of a dome.

In calculating σ_D, we used figure 4.1(a) to predict that a width to length ratio of $2100/1400 \approx 0.67$ corresponded to a dimensionless length of $L = 2.0 \pm 0.5$. Equation (4.4) then provided the final result.

The remaining graphs in Figure 4.1 show other ratios of horizontal lengths which may also be used to estimate the yield strength of a dome from observed dimensions. However, the use of these relies on being able to determine the vent location and the distance the dome has spread upslope or downslope. If this location is known, then these graphs may provide a more accurate determination of yield strength than will the use of the planform aspect ratio.

4.2 Summary

We have obtained a solution for the shape of a dome of yield strength fluid emplaced on a slope, in the simple case of very slow emplacement and constant rheology. This

solution predicts that domes of small size and density, lying on gentle slopes and with large yield strengths, will tend to be axisymmetric. For other domes, the effect of gravity will be more influential on the shape of the dome, and the dome will be more elongated in the down-slope direction.

Our solution complements existing solutions for Newtonian viscous flows on a sloping plane and forms a (highly idealized) base for studies of the planform and morphology of more complex flows on sloping topography, including Bingham rheology, heterogeneous rheology, nonplanar topography, cooling, and solidification. We found that isothermal experiments with slurries agreed well with the theory. However, caution is warranted, owing to the fact that we have not been able to make satisfactory direct measurements of the yield strength of the slurries. Instead, we have evaluated yield strength by carrying out separate experiments on a horizontal base and applying Nye's (1952) symmetrical solution. In this evaluation of yield stress we have used the theoretical constant $C = \sqrt{2}$, which leads to a good agreement between experiment and theory on sloping planes. This value of C differs from an empirical value obtained by Blake (1990) with reference to direct rotating vane viscometer measurements of yield strength. Using the theoretical constant results in an estimation of the yield strength 55% larger than that using Blake's empirical value.

Our results were used to predict the yield strength of the Medicine Lake Dacite Flow, using the flow width, thickness or width to length ratio. Good agreement was found between these values and existing measurements based solely on its thickness.

Part II

Wind-driven Convection at Ocean Density Fronts

Chapter 5

Introduction

5.1 Overview

Oceanic fronts are regions in the oceans which have an enhanced horizontal gradient of temperature, salinity or density. They are a common and significant feature in many of the world's oceans, and are of great interest due to their association with increased levels of biological activity, mixing, and as sites of water subduction.

Adjacent to fronts, large volumes of water are often found with near homogeneous properties of temperature, salinity and density. This water is called mode water, and forms due to convection which mixes heat and salt within the water column. The cause of the convection is not always clear, though in some cases it may be due to a wind-driven surface Ekman layer. Depending on the wind direction, dense water may be forced across the front and over the top of the lighter water, leading to gravitational instabilities. This process has been postulated to lead to the formation of Subantarctic Mode Water to the north of the Subantarctic front in the Southern Ocean. (England et al., 1993; Hirst and Godfrey, 1993; Rintoul and England, 2002).

Very little is known about this method of generating convection. Numerical studies that simulate this process often use a convective adjustment scheme, which assumes perfect mixing between the overlying dense fluid and the less dense fluid beneath. However, experimental evidence suggests that the mixing is not perfect (Linden and Redondo, 1991). In this thesis we design and conduct a series of experiments using a rotating table to investigate the generation of convection through the forcing of dense water across a front. We focus in particular on the amount of mixed water produced by such a convective event, and the resulting mixing efficiency.

5.2 Background

In general terms, the surface water near the equator is warmer and saltier than the surface water at higher latitudes. The gradient in temperature between the equatorial and polar waters has an opposing effect on the water density to the salinity gradient. The effect of temperature tends to dominate, marginally at the surface, though by a factor of two beneath the mixed layer (Schmitt, 1999), and thus the polar water is more dense than the equatorial water.

The transition from the less dense equatorial waters to the more dense polar waters is not uniform. Instead it tends to be concentrated at fronts, a feature first noticed by Deacon (1937) in the sea surface temperature of the southern ocean. Many of these temperature fronts are coincidental with salinity fronts and are nearly density compensated, though some, particularly those associated with the Antarctic Circumpolar Current (ACC), have strong density gradients (Sokolov and Rintoul, 2002). These density fronts are able to persist for long times in the ocean due to the thermal wind balance (Rossby, 1937, 1938). The horizontal gradient in density is related to a vertical gradient in velocity.

When winds blow in the vicinity of ocean density fronts, the Ekman layer transport can cause water to be advected across the front. Under certain circumstances the denser water from one side can be carried over the less dense water. Such a situation inevitably leads to instability and convection.

North of the ACC, deep convection forms a vertically well-mixed layer known as the Subantarctic Mode Water (SAMW). The formation and subduction of this water is believed to play an important part in the vertical mixing and uptake of gases such as carbon dioxide (Poisson et al., 1993; Metzl et al., 1999). Whether or not the cross-frontal Ekman transport mentioned above is one of the main mechanisms governing this convection is a matter of some controversy. McCartney (1977, 1982) proposed that most convection in the mid-latitudinal regions is related to oceanic heat loss. That is, as ocean currents flow from warm to cold regions, the water's surface cools, leading to deep convection. This was supported by work showing that regions with the greatest rate of oceanic heat loss coincided with regions containing maximal convection depths

(England et al., 1993; Hirst and Godfrey, 1993). However, the general correlation between heat loss and convection depth was not as good. England et al. (1993) and Ribbe and Tomczak (1997) both proposed the northward directed Ekman flux of cold water leading to convection as a means to explain the discrepancies. This was given support by the work of Rintoul and England (2002), who indicate that the seasonal variations in SAMW properties can only be explained by convection due to Ekman transport.

In addition to uncertainty about the relative importance of cross-frontal Ekman transport in leading to the formation of mode water, the process is also not well represented in ocean general circulation models (OGCMs). OGCMs use large computational power to model the earth's ocean, often to predict long term global climate change, but also to understand present flow and dynamics. Low resolution OGCMs fail to resolve the fine features associated with ocean fronts and are thus not good at predicting density inversions and convection caused by cross-frontal Ekman transport (Bryden, 1983). Moreover, most computational models, including finer scale models designed to resolve fronts, use a convective adjustment scheme. If an unstable density profile is found between two vertically adjacent cells, the temperature and salinity of those cells are averaged. This process is repeated if density inversions remain, until a stable density profile is formed. Convective adjustment schemes thus assume perfect mixing, an assumption which is at odds with the results of Linden and Redondo (1991) in their study of Rayleigh-Taylor mixing. They found mixing efficiencies of 0.35 for Atwood numbers greater than approximately 0.02, and even smaller efficiencies for smaller Atwood numbers. Their definition of mixing efficiency was such that perfect mixing resulted in a mixing efficiency of 0.5. This result led them to deduce that the magnitude of the final stable density gradient after a Rayleigh-Taylor mixing event with a mixing efficiency of 0.35 is approximately 11% of the originally unstable density gradient, in contrast to the homogeneous density profile that would result from perfect mixing. For the smaller Atwood numbers likely to arise in the ocean the final stable density gradient is likely to be even stronger. On the other hand, convection driven by a sustained buoyancy flux may behave differently (Jellinek et al., 1999).

There remains little knowledge of the degree to which wind-driven convection at

ocean density fronts can generate mixed water, as very few studies have investigated the phenomenon without using numerical simulation with convective adjustment schemes. Soloviev et al. (2002) considered the existence of sharp fronts and their orientation relative to wind direction, and developed a theory to predict the presence of turbulent bores to create mixing. This theory was for fronts in tropical waters, where the fronts were the leading edge of spreading gravity currents. It did not consider the Coriolis force which enables fronts to be stationary, neither did the bore theory predict the amount of mixing produced by the turbulent bores. Ivey et al. (2000) studied a similar problem related to frontal mixing associated with coastal upwelling. They introduced a parameter to reflect the degree of mixing produced by the convection, though they did not attempt to determine its value, or what it depended on.

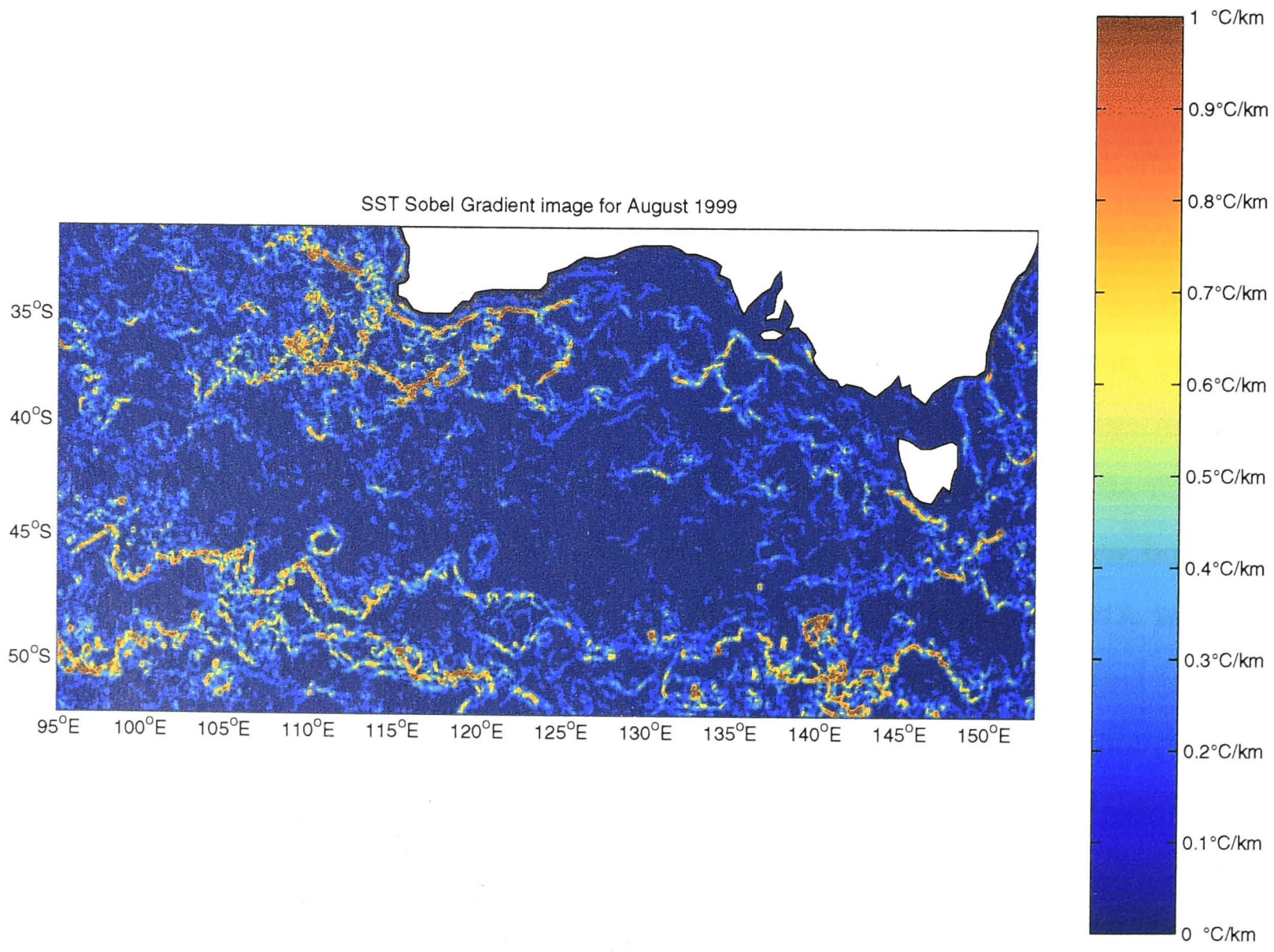

Figure 5.1: An image of sea surface temperature gradients in the Southern Ocean south of Australia.

5.3 This project

This thesis presents laboratory experiments that were conducted as a first step towards understanding the process of wind-driven convection at density fronts. The experiment is introduced in chapter 6, along with some qualitative observations of the flow. In chapter 7 the momentum equations and scaling estimates are used to show that the standard Ekman layer equations apply to these experiments, despite the presence of stratification. The relevant theoretical results from Rayleigh-Bénard convection and Rayleigh-Taylor instability are also reviewed to show that convection should occur once the density profile becomes unstable, and to provide a scaling theory for the timescale for the onset of convection.

In chapter 8 the experimental results are presented. They show how long it takes for convection to start, and how the amount of mixed water and the potential energy of the system are increased by the forcing event. The relevance of these results to oceanic fronts are discussed, followed by the conclusions in chapter 9.

Chapter 6

Experimental method and qualitative observations

6.1 Apparatus and experimental procedure

The experiments were conducted in the cylindrical rotating tank pictured in Figure 6.1. The tank had a radius of 49 cm and was surrounded by a rectangular box and a water filled cavity to provide undistorted side views. The tank also had a water tight lid which could be rotated at a speed different to that of the tank. The lid was approximately 8.1 cm above the base of the tank creating a working volume of 61 litres.

In order to create a two layer density stratification, the upper layer of seven litres volume was first placed into the stationary tank. The lower layer was then slowly emplaced underneath the upper layer using a tube inserted through a hole in the lid. We filled the working volume of the tank completely so that no air pockets remained underneath the lid. This process took about 3 hours.

Once the two layers were in place, the computer-controlled rotation rate of the tank was linearly increased from rest to full speed (2.2 rad/s) over a 2.5 hour period. The tank and its contents were given an additional 1.5 to 2 hours to settle to solid body rotation, a time scale that was decided upon by observing the interface between the two layers and waiting for it to reach its final parabolic shape. The volume of the upper layer and the tank rotation speed were chosen so that the interface outcropped on the lid, at a radius approximately three quarters that of the tank radius. This created the required front, which was therefore maintained through centrifugal force rather than a geostrophic balance.

Figure 6.1: The rotating table used for the experiments.

The experiment proper was begun by rotating the lid at a slightly slower speed than the tank (anticyclonic forcing), usually for a period of one minute. The relative rotation rate was constant during each forcing event, though it ranged from 0.06 to 0.2 rad/s between experiments.

Planar laser-induced fluorescence (PLIF) was used to measure the production of mixed fluid due to the forcing event, using the setup illustrated in Figure 6.2. A 500mW argon ion laser was attached to the rotating framework, with the beam passing through an expander and then reflected off an angled mirror which created a sheet of light directed vertically upwards. It was reflected off two 45° mirrors above the tank back down towards the tank, where it illuminated a vertical sheet of water of approximately 4 mm in thickness along a radius of the tank. The upper layer of the two layer density stratification was premixed with a sodium fluorescein dye to make a 5×10^{-7}M solution, which fluoresced in the laser light.

A digital video camera was attached to the rotating framework approximately 1.7 metres higher, and at a slightly larger radius than, the outer edge of the tank. It was pointed downwards towards another angled mirror, which reflected an image of the illuminated sheet of fluid as viewed from an angle perpendicular to the laser sheet. A low pass optical filter was placed in front of the camera to remove the shorter wavelength incident laser light, while passing the longer wavelength light emitted by the dye. Still images of the illuminated fluid were taken every five minutes throughout the experiment. To reduce the amount of noise, each image was constructed from an average of 16 separate video frames. These images were then used to calculate an approximate representation of the density field in the tank, using the process described in Appendix A.

The density difference between the two layers varied from 1.8 to 17.6 kg/m^3. For most of the experiments, this was achieved by dissolving sodium chloride salt into the lower layer. However this created a mismatch in the refractive index between the two layers. The resultant optical distortions meant that quantitative measurements could not be made while there was any motion in the interface between the two layers. For this reason, measurements were only made before, and a long time after, the wind forcing event, when there was minimal residual flow within the tank.

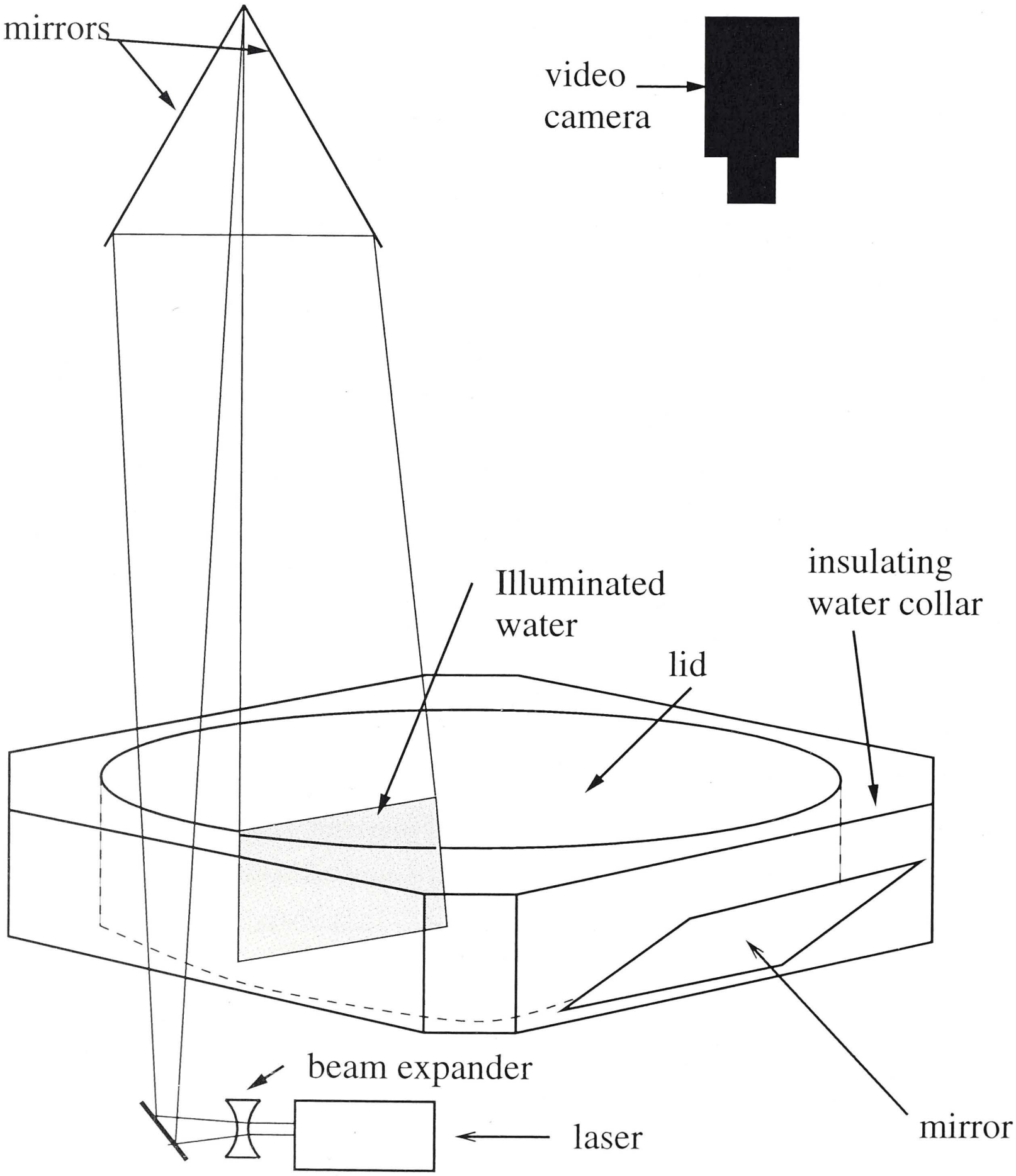

Figure 6.2: Schematic of the experimental apparatus.

Optical distortions across the interface still played a role even when there was no flow in the tank. Thus, for the experiments with larger density differences between the two layers, where distortions would have otherwise been largest, we used the method described by McDougall (1979) and Atsavapranee and Gharib (1997) to match the refractive index of the two layers. Diffusing agents were used in both layers, sucrose in the upper layer and epsom salt (magnesium sulfate) in the lower. Concentrations were adjusted so that the refractive indices of the two layers matched, though the desired density difference remained. Having two solutes introduces the possibility of double diffusive convection, and in particular, of salt fingering, given that epsom salt has a larger diffusivity ($\kappa_{\mathrm{ep}} = 0.61 \times 10^{-9}\mathrm{m}^2/\mathrm{s}$) than sucrose ($\kappa_{\mathrm{su}} = 0.45 \times 10^{-9}\mathrm{m}^2/\mathrm{s}$). Introducing the diffusivity ratio, $\tau = \kappa_{\mathrm{su}}/\kappa_{\mathrm{ep}} \approx 0.74$, and the density anomaly ratio, $R_\rho = \Delta\rho_{\mathrm{ep}}/\Delta\rho_{\mathrm{su}}$ (where $\Delta\rho_{\mathrm{ep}}$ is the density anomaly in the lower layer due to epsom salt, and $\Delta\rho_{\mathrm{su}}$ is the density anomaly in the upper layer due to sucrose) salt fingers may form when $R_\rho < \tau^{-3/2} \approx 1.58$ (Huppert and Manins, 1973). For our experiments, the minimum value of R_ρ was 1.81, indicating that fingers would not complicate our experiments.

In some experiments we also altered the viscosity of the water using the polymer sodium carboxymethyl cellulose (CMC). CMC powder was added to both layers so that the viscosities were equal, while sodium chloride was used to increase the density of the lower layer.

6.2 Qualitative description of the experimental flow

In addition to the quantitative experiments performed using the PLIF procedure described in the previous section, some qualitative experiments were also undertaken. For these experiments the water in the tank was initially undyed, though immediately before the beginning of the forcing event, red food dye was released at a constant flow rate from a tube passing though the lid. The dye emerged directly adjacent to the lid near the outer radius of the tank and outside the position of the front.

When the lid was turned on, momentum was transferred from the lid to the upper boundary layer of the water. After approximately one second the Ekman layer was

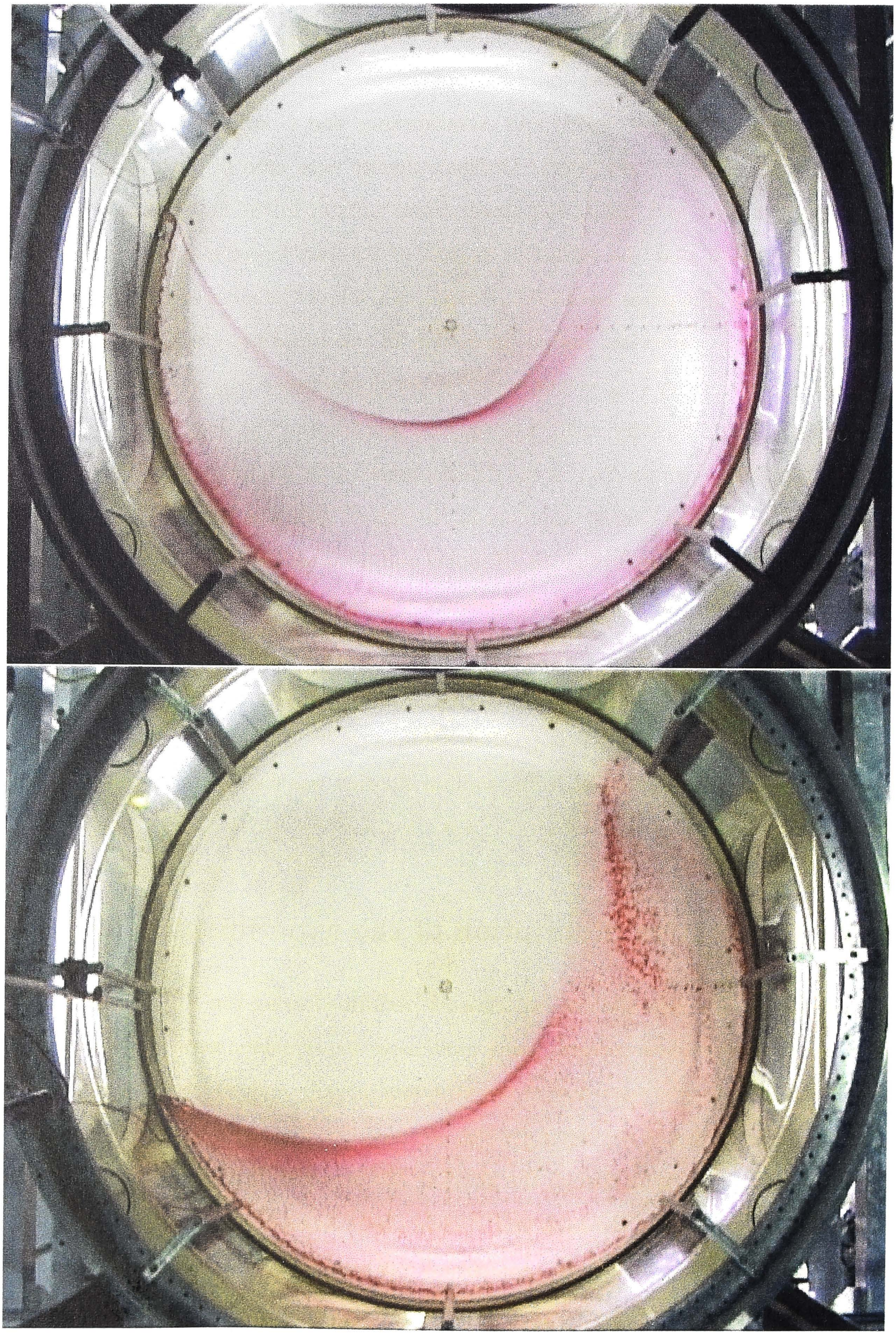

Figure 6.3: Overhead pictures of the forcing event where red dye has been released immediately underneath the lid. The tank was filled with a homogenous density fluid in the top picture, while the lower picture is of a tank filled with a two layer density stratification, with the density interface outcropping on the lid at a radius approximately three quarters of the tank radius.

near fully established. Some of the dye was sufficiently far from the lid that it was not affected by this boundary layer, and remained stationary. Dye within the Ekman layer was advected away from its initial location, and much of it spiralled in towards the centre of the tank as expected for Ekman layer flow in a circular tank.

Overhead pictures taken of two of these experiments are shown in figure 6.3. In the top picture there is no density difference between the two layers, so the tank is unstratified. The dye that was advected by the Ekman layer, and subsequently spiralled in towards the centre is visible, as is the dye that was not affected by the boundary layer flow. Note that the source of the dye was moving relative to the camera, which explains why this second dye appears as a streak around the edge of the tank, despite the dye being stationary in the tank.

The lower figure shows an experiment with a two layer density stratification, similar to those used in the remainder of the experiments presented in chapter 8. The density difference between the two layers was $\Delta\rho = 12.4$ kg/m^3, while the density of the dye was approximately that of the upper layer. The photo was taken approximately 20 seconds after the lid was turned on. The first several seconds of this experiment appeared identical to that of the homogeneous case. After about eight seconds gravitational instabilities started to become visible in the dye streak and convection followed soon after. The same two primary dye streaks that appeared in the homogeneous experiment are again visible. However there is also much more dye between those two limiting pathways. This dye makes a speckled pattern and represents dye that was originally in the Ekman layer and advected inwards, but then fell out of the boundary layer once convection started. The speckled nature of the dye illustrates the pattern of convection typical of rapidly rotating systems. The influence of the Coriolis force causes the rising and falling convecting plumes to be confined to narrow vortices, of a sufficiently small size that viscous effects enable the break down of the Taylor-Proudman theorem.

The particularly intense cluster of speckled dye patterns in the top right hand quadrant of the tank in the lower frame of figure 6.3 is the remnant of the initial convective event. The delay between the establishment of the Ekman layer and the onset of convection leads to much more dye (and dense fluid) accumulating in the Ekman layer than is possible once convection is established. Thus the initial convective

event is stronger than the convection that occurs during the remainder of the forcing event. It is apparent from the lower picture in figure 6.3 that most of the dye that was advected by the Ekman layer before the onset of convection was lost from the Ekman layer during this initial convective event.

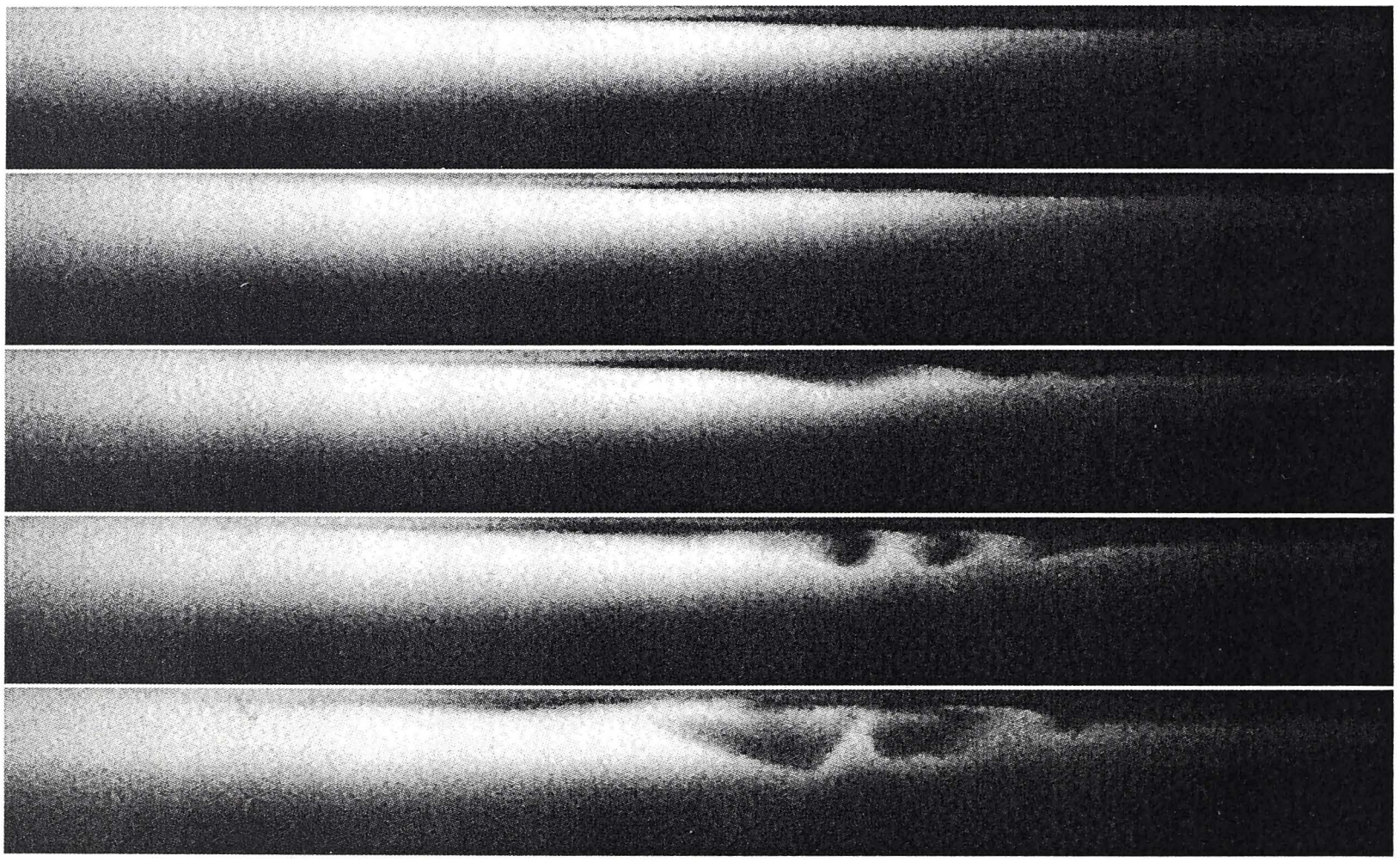

Figure 6.4: A series of side view pictures from experiment 48, in which the fluid viscosity was increased. The pictures show an illuminated vertical sheet of fluid along a radial section extending from a radius of 107mm to 432mm, and occupying a vertical range from the lid to a depth 39mm. The upper layer is dyed with a fluorescein dye and is the lighter coloured fluid visible in the top left hand side of the pictures. The pictures are taken at approximately half second intervals and show the Ekman layer advecting dense fluid from the right hand side of the pictures across the front and over the top of the less dense upper layer. Eventually, instabilities start to form and lead to the convection visible in the latter pictures.

Figure 6.4 shows pictures from experiment 48, which used the PLIF method to visualise the experiment, and which was used in all of the quantitative experiments presented in chapter 8. The pictures show a side view of the radial sheet of fluid illuminated by the vertical sheet of laser light. The upper layer contains fluorescein dye, and thus appears as a pale colour, while the lower layer is dark. The pictures were taken at approximately half second intervals, shortly before and during the onset

of convection. Visible at the top (in the right half) of each image is dense fluid being advected by the Ekman layer. This fluid originated from outside the front (the top right hand corner of the photo) and is flowing to the left over the top of the upper layer. The length of this unstable layer grows with time, and it eventually becomes unstable and starts to convect through the depth of the upper layer, as is visible in the subsequent pictures. The time interval between starting the lid and convection first reaching the interface between the two layers (as is about to happen in the final picture of figure 6.4) was defined as the convection timescale. These pictures were taken from an experiment in which the fluid was quite viscous, due to the addition of CMC powder to the water. In most of the experiments, the Ekman layer and the individual convecting plumes were too small to see owing to the smaller viscosity, though the region undergoing convection was still apparent.

Once convection was fully established it was difficult to make accurate measurements using the PLIF method, even for the convection experiments in which the refractive indices of the two layers were matched. This was partly due to the density field not being axisymmetric during and for some time after the convection event, which was assumed in making the density calculations. It was also due to the method of averaging 16 separate video frames to produce each image used for the density calculations. This technique required an essentially unchanging picture over the averaging period (approximately 0.5 seconds) in order to produce accurate predictions of the density field. This requirement was not satisfied during the convective event. For these reasons we did not make measurements during the forcing event.

Once the lid was halted, convection persisted until all the dense fluid located above the upper layer had fallen. The tank then slowly settled back down to solid body rotation. As the remaining motions in the tank decayed, we were then able to detect the increased presence of mixed water near the frontal region.

Chapter 7

Model theory

This chapter brings together theories which are relevant to the flow seen in the experiments. We divide the behaviour into two stages. In section 7.1 we show that the Ekman layer equations can be used to describe the flow before gravitational instability, and we consider how they might advect the density interface. Then in section 7.2, we investigate the gravitationally unstable layer using the theories for Rayleigh-Taylor instability and Rayleigh-Bénard convection.

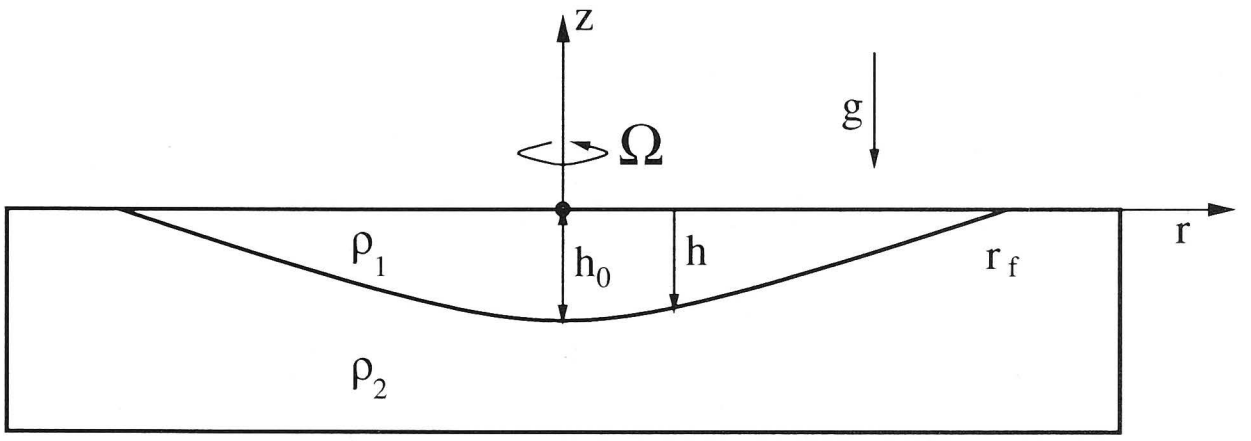

Figure 7.1: Schematic of the rotating axisymmetric two-layer system.

7.1 Before instability

Let us consider the equations of motion for the two-layer fluid pictured in figure 7.1. It has a density field given by

$$\rho = \begin{cases} \rho_1 & \text{, if } z \geq h(r) \\ \rho_2 & \text{, if } z < h(r). \end{cases} \tag{7.1}$$

The momentum equations in cylindrical co-ordinates rotating at a constant angular velocity Ω are:

$$\frac{\partial u_r}{\partial t} + u_r\frac{\partial u_r}{\partial r} + \frac{u_\phi}{r}\frac{\partial u_r}{\partial \phi} + u_z\frac{\partial u_r}{\partial z} - \frac{u_\phi^2}{r} - 2\Omega u_\phi = -\frac{1}{\rho}\frac{\partial P}{\partial r} + \nu\frac{\partial^2 u_r}{\partial z^2} + \Omega^2 r, \tag{7.2}$$

$$\frac{\partial u_\phi}{\partial t} + u_r\frac{\partial u_\phi}{\partial r} + \frac{u_\phi}{r}\frac{\partial u_\phi}{\partial \phi} + u_z\frac{\partial u_\phi}{\partial z} + 2\Omega u_r = -\frac{1}{\rho}\frac{\partial P}{\partial \phi} + \nu\frac{\partial^2 u_\phi}{\partial z^2} \tag{7.3}$$

and

$$\frac{\partial u_z}{\partial t} + u_r\frac{\partial u_z}{\partial r} + \frac{u_\phi}{r}\frac{\partial u_z}{\partial \phi} + u_z\frac{\partial u_z}{\partial z} = -\frac{1}{\rho}\frac{\partial P}{\partial z} + \nu\frac{\partial^2 u_z}{\partial z^2} - g. \tag{7.4}$$

Here u_r, u_ϕ and u_z are the radial, azimuthal and vertical components of velocity, P is the total pressure, not just the deviation from hydrostatic, ν is the kinematic viscosity, and g is the acceleration due to gravity. We have assumed that viscosity is depth independent, and strain rates are greatest in the vertical. The continuity equation is given by

$$\frac{1}{r}\frac{\partial (r u_r)}{\partial r} + \frac{1}{r}\frac{\partial u_\phi}{\partial \phi} + \frac{\partial u_z}{\partial z} = 0 \tag{7.5}$$

and the density equation is

$$\frac{\partial \rho}{\partial t} + u_r\frac{\partial \rho}{\partial r} + \frac{u_\phi}{r}\frac{\partial \rho}{\partial \phi} + u_z\frac{\partial \rho}{\partial z} = \kappa\frac{\partial^2 \rho}{\partial z^2}, \tag{7.6}$$

where κ is the diffusivity.

7.1.1 The base state: solid body rotation

Let us first consider the situation when we have solid body rotation, before any surface stresses commence, and assume we have reached a state in which no velocities are present[1]. In this situation, the radial (7.2) and vertical (7.4) momentum equations reduce to

$$\frac{\partial P}{\partial r} = \rho\,\Omega^2 r \tag{7.7}$$

[1]Phillips (1970) showed that it is impossible to achieve motionless flow in a stratified fluid when an isopycnal makes contact with a boundary at a non-perpendicular angle. However the induced velocities are small, and the resultant production of mixed fluid is negligible in comparison to that produced by the lid forcing events (see, for example, figure 8.6, which shows little indication of mixed fluid production other than that caused by the lid forcing event).

and

$$\frac{\partial P}{\partial z} = -\rho g. \tag{7.8}$$

In our two layer system for such a system to be in its lowest potential energy state, and thus stable, we require the density interface to be located on an isobaric surface. This leads to the equation of the interface

$$h = -h_0 + \frac{\Omega^2}{2g} r^2 = \frac{\Omega^2}{2g}(r^2 - r_c^2), \tag{7.9}$$

where h_0 is the depth of the interface on axis and r_c is the radius of the front as it outcrops on the lid at $z = 0$. Note that the slope of the density interface depends only on the ratio of the centrifugal acceleration to gravity and not on the density difference.

The solution to the pressure equations (7.7)-(7.8) with the density field implied by (7.1) and (7.9) is

$$P_i = \begin{cases} P_0 + \frac{1}{2}\rho_1 \Omega^2 r^2 - \rho_1 g z, & z \geq h(r) \\ P_0 + \frac{1}{2}\rho_1 \Omega^2 r^2 + \frac{1}{2}\Delta\rho\, \Omega^2 (r^2 - r_c^2) - \rho_2 g z, & z < h(r)\ , \end{cases} \tag{7.10}$$

where $\Delta\rho = \rho_2 - \rho_1$.

It is interesting to note that the pressure field in the tank complete with lid is the same as it would be without the lid. For the planar lid to form a watertight seal on the tank, it must be able to support a pressure field to the top boundary of the fluid identical to that which would form if there was a free surface, which would take on a parabolic profile parallel to the density interface given by (7.9).

We shall call this condition of solid body rotation our base state and, in the next section, we subtract this configuration of density and pressure from the momentum equations to determine what happens when a surface stress is present (the lid is turned on).

7.1.2 The Ekman layer equations

When the lid is turned on with rotation rate $-\omega$ relative to the tank, the solid body motion is perturbed. We separate the density field into the components $\rho = \rho_i + \rho'$,

where ρ_i is given by (7.1), with $h(r)$ given by (7.9), and the pressure field into $P = P_i + P'$, where P_i is given by (7.10), and is the hydrostatic part of the initial pressure field in a rapidly rotating system. As the initial flow and the lid forcing are axisymmetric, we shall assume the flow remains axisymmetric. We shall also assume the Rossby number $Ro = \omega/\Omega$ is much less than one, consider times $t \gg \Omega^{-1}$ and use the Boussinesq approximation ($\rho' \ll \rho_2$). Our governing equations (7.2)-(7.4) reduce to

$$-2\Omega u_\phi = -\frac{1}{\rho_2}\frac{\partial P'}{\partial r} + \nu\frac{\partial^2 u_r}{\partial z^2} + \frac{\rho'}{\rho_2}\Omega^2 r, \tag{7.11}$$

$$2\Omega u_r = \nu\frac{\partial^2 u_\phi}{\partial z^2} \tag{7.12}$$

and

$$\frac{\partial P'}{\partial z} = \rho' g. \tag{7.13}$$

We simplify the radial momentum equation (7.11) by considering the relative sizes of the various terms. For the moment we are primarily interested in the boundary layer just underneath the lid. Here the no-slip boundary condition requires $u_\phi \sim \omega r$. The ratio of the perturbation centrifugal force (the last term on the right hand side) to the Coriolis force (the term on the left hand side) is given by

$$\frac{\rho'\Omega^2 r}{2\rho_2\Omega u_\phi} \sim \frac{\Delta\rho\Omega}{2\rho_2\omega} \approx \frac{A}{Ro} \tag{7.14}$$

where $A = (\rho_2 - \rho_1)/(\rho_2 + \rho_1) \approx \Delta\rho/(2\rho_2)$ is the Atwood number. Although both the Atwood and Rossby numbers are much less than unity in our experiments, $A/Ro < 0.11$. Hence the Coriolis term is much greater than the perturbation centrifugal force.

The first term on the right of the radial momentum equation is the perturbation pressure gradient term. Its magnitude is found by integrating the vertical momentum equation (7.13), which tells us that the pressure perturbations will occur when the density is altered from its initial state. Density perturbations are caused by diffusion and advection of the density interface. Diffusion is likely to occur evenly along the interface, so diffusion of the interface can be mostly absorbed into the hydrostatic parts of the density and pressure fields. Thus we shall only consider the effect of the

advection of the interface. This occurs only in the upper boundary layer of thickness δ, and creates a density perturbation of magnitude $\rho' \sim \Delta\rho$. Thus the maximimum value that the pressure perturbation may take is

$$|P'|_{\max} \sim \Delta\rho g\delta. \tag{7.15}$$

If the density interface is infinitessimally thin, then it is possible for the radial perturbation pressure gradient to be infinite. However, in reality the density changes between two miscible layers over a non-zero distance. The perturbation pressure gradient term of (7.11) is then limited to

$$\left|\frac{1}{\rho_2}\frac{\partial P'}{\partial r}\right|_{\max} \sim \frac{g'\delta}{\Delta r}, \tag{7.16}$$

where $g' = g\Delta\rho/\rho_2$ is the reduced gravity and Δr is the horizontal thickness of the interface.

As before, we compare this perturbation pressure gradient term to the Coriolis term

$$\left|\frac{1}{2\Omega\rho_2 u_\phi}\frac{\partial P'}{\partial r}\right|_{\max} \sim \frac{g'\delta}{2\Omega\Delta r\omega r} \tag{7.17}$$

and find that, if

$$\Delta r \gg \frac{g'\delta}{2\Omega\omega r}, \tag{7.18}$$

then we can ignore the radial perturbation pressure gradient. For all our experiments, the right hand side of this equation ranges from 0.02 mm-0.6 mm, which is much thinner than any front we would be able to create in the laboratory. Indeed, it would only take diffusion of salt a time $t \sim (\Delta r)^2/\kappa$, (at most 4 minutes), for diffusion to widen the front by this amount. Thus we are able to ignore the pressure perturbation term.

The governing horizontal momentum equations (7.11)-(7.12) now reduce to the standard Ekman (1905) layer equations,

$$-2\Omega u_\phi = \nu\frac{\partial^2 u_r}{\partial z^2} \tag{7.19}$$

and

$$2\Omega u_r = \nu\frac{\partial^2 u_\phi}{\partial z^2}. \tag{7.20}$$

When subject to the boundary conditions of $u_r = 0, u_z = 0$ and $u_\phi = -\omega r$ at the upper boundary ($z = 0$), and $u_r = 0$ and $u_\phi = 0$ in the interior ($z \ll -\delta$), these equations have the solution

$$u_r = \omega r e^{z/\delta} \sin(z/\delta), \tag{7.21}$$

$$u_\phi = -\omega r e^{z/\delta} \cos(z/\delta) \tag{7.22}$$

and

$$u_z = -\omega\delta[1 + e^{z/\delta}(\sin(z/\delta) - \cos(z/\delta))], \tag{7.23}$$

where the Ekman layer thickness is given by

$$\delta = \sqrt{\frac{\nu}{\Omega}}. \tag{7.24}$$

Streamlines of this flow at a variety of depths are shown in Figure 7.2. In particular, figure 7.2(b) shows a very good agreement with the dye streaks (figure 6.3) that were advected by the Ekman layer in our quantitive experiments of section 6.2.

There are a few points to note before we move on from these Ekman layer equations. Firstly, we have ignored the Stewertson layers that form near the tank sidewall. This does not affect our subsequent analysis provided the front is sufficiently distant from from the tank sidewall.

Secondly, in assuming $t \gg \Omega^{-1}$, the time it takes for the Ekman layer to be established was neglected. Benton and Clarke (1974) deduce from Greenspan (1968) that the Ekman layer becomes fully developed when

$$t_{\mathrm{Ek}} \approx 2/\Omega. \tag{7.25}$$

Thirdly, we note that the boundary layer (7.24) has the standard Ekman layer thickness. Pedlosky (1987) and MacCready and Rhines (1991) show that the Ekman layer thickness on a slope is increased by a factor of $(\cos\alpha)^{-1/2}$, where α is the slope angle from horizontal. It might appear that the Ekman layer in our experiments, where we use centrifugal force to tilt the isopycnals away from horizontal, should be analagous to a sloping Ekman layer. However, the increased thickness of the Ekman layer on a

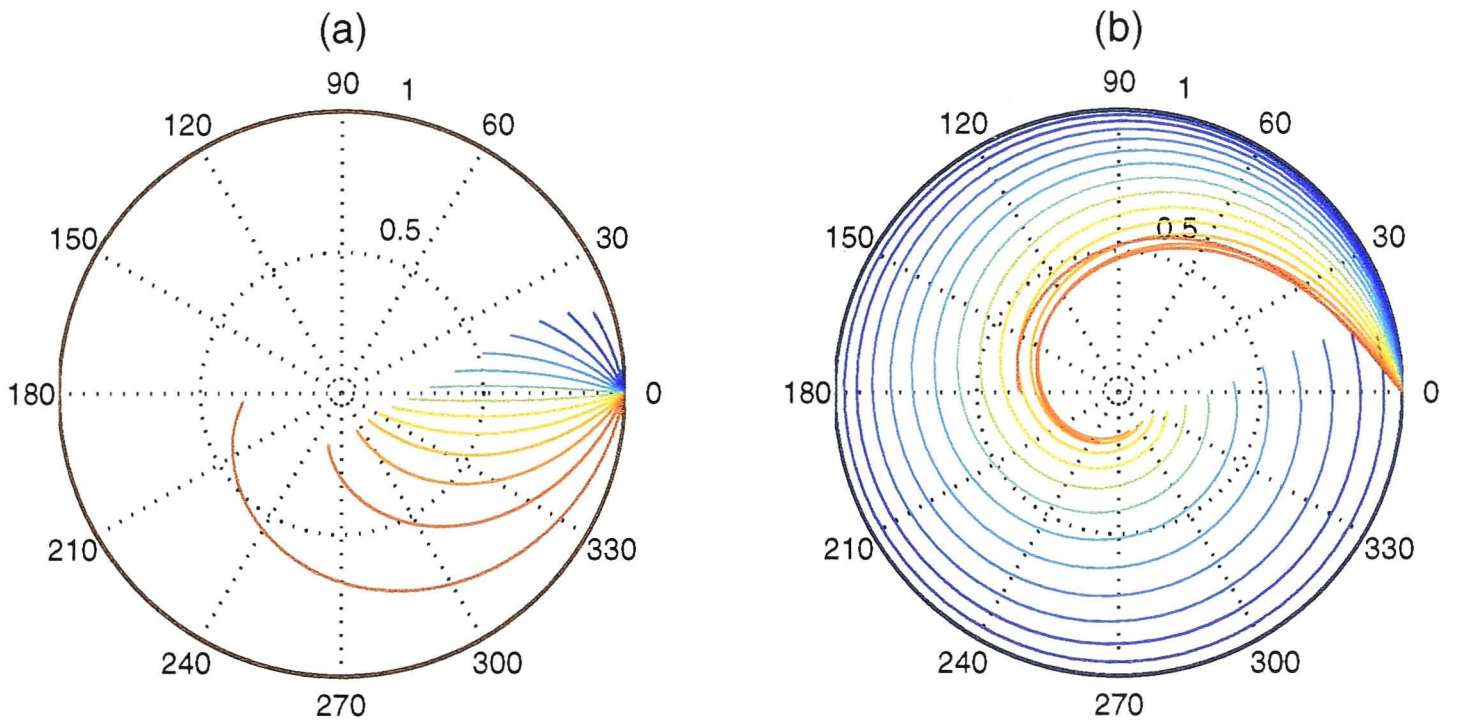

Figure 7.2: The Ekman layer solution for anticlockwise rotation Ω and clockwise lid rotation ω. In plot (a), the lines represent the streamlines as drawn in the reference frame of the rotating tank. Each colour represents a streamline for a different depth, starting from a dimensionless depth of $z/\delta = -0.01$ (the outer red spiral), and decreasing linearly to a dimensionless depth of $z/\delta = -3.14$ (dark blue). The streamlines commence at a dimensionless time of $\omega t = 0$ and continue to $\omega t = 2\pi$. Plot (b) differs in that it is drawn in the frame of reference of the rotating lid, though it can also represent the dye streaks that would emerge for a source moving with the lid when viewed from the tank's reference frame. The colour scheme is the same. Note that the streamlines that do a complete circuit of the tank are the ones at greater depths, contrasting with those in plot(a) where the longer streamlines are those from shallower depths.

sloping boundary results from the projection of the rotation vector onto the vertical axis of the sloping co-ordinate system. As the direction of the z axis in our co-ordinate system is parallel to the rotating axis, the $(\cos\alpha)^{-1/2}$ does not come into our equations.

Fourthly, the boundary condition of no interior flow is valid only if the surface stress is not present for long enough to affect significantly the interior flow. However, the Ekman layer does affect the interior flow through the spin-up process (or spin-down in this case). The vertical Ekman layer velocity described by equation (7.23) is non-zero in the interior. It is directed downward and has the effect of compressing fluid columns and inducing anticyclonic relative vorticity. The time for the lid to affect significantly the horizontal velocity of the fluid in the upper layer through the spin-down process is of order $h_0(\nu\Omega)^{-1/2}$.

Finally, by integrating (7.23), we find that the volume flux of fluid crossing the

initial position of the surface front is given by

$$Q_{\mathrm{Ek}} = \pi r_c^2 \omega \delta. \tag{7.26}$$

7.1.3 Advection of the density interface by the Ekman layer

The initial position of the front, given by (7.9), may be rewritten in terms of its radius as a function of depth,

$$r_{f0}^2 = r_c^2 + \frac{2gz}{\Omega^2} = r_c^2(1 + Mz^*), \tag{7.27}$$

where $M = 2g\delta/(\Omega^2 r_c^2) = \delta/h_0 \ll 1$ is the ratio of the Ekman layer thickness to the central thickness of the upper layer, and $z^* = z/\delta$ is the normalised depth variable.

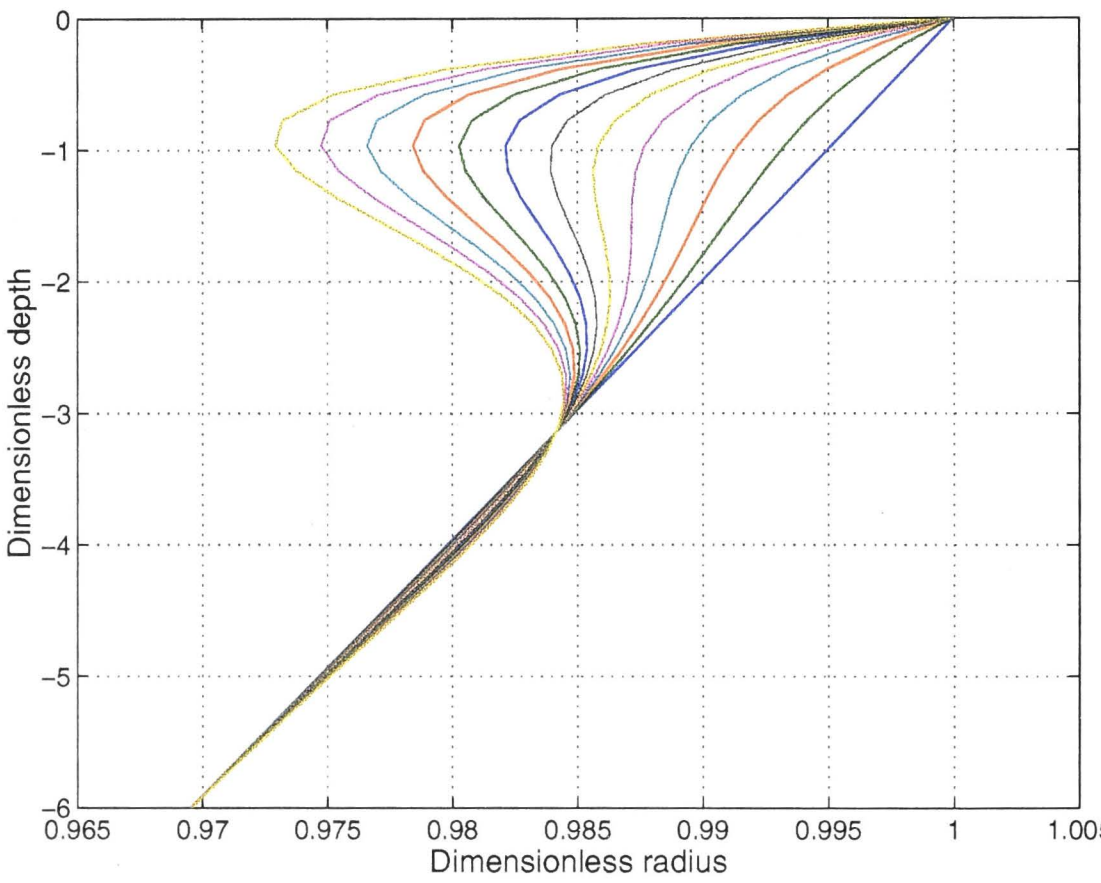

Figure 7.3: Advection of the density interface by the radial Ekman velocity, according to equation (7.28). The radius has been non-dimensionalised by the frontal radius, r_f, while the depth has been non-dimensionalised by the Ekman layer thickness. The density interface has been plotted at 13 different times ranging linearly from $t = 0$ to $t = 3t_c \approx 7.2M\omega^{-1}$ in steps of $t_c/4$. In this plot $M = 10^{-2}$.

The vertical Ekman layer velocity (7.23) is orders of magnitude smaller than the radial Ekman layer velocity (7.21), so we shall consider only the advection of the interface by the radial Ekman velocity. The time dependent equation of the interface

is then given by

$$r_f = r_c\sqrt{1+Mz^*}\exp(e^{z^*}\sin(z^*)t^*) \tag{7.28}$$

where $t^* = \omega t$ is the non-dimensional time. Figure 7.3 is a plot of this time dependent density interface for a value of $M = 10^{-2}$. A plot showing the numerical result of the time dependent density interface where vertical advection has not been ignored is virtually indistinguishable from the one shown. Note that for equation (7.28) and the plot it is assumed that the Ekman layer becomes fully established much faster than the timescale involved in advecting the density interface. We shall reconsider this assumption at the end of this section.

From figure 7.3 it is clear that, at a particular time, the interface at some depth becomes vertical, and for times after that we have a gravitationally unstable situation. By differentiating (7.28) with respect to z, setting the result to zero and using $M \ll 1$, we find that density interface first becomes vertical at a dimensionless depth of $z^* = -\pi/2$, and at a time

$$t_v = \frac{t_v^*}{\omega} = \frac{M}{2\omega}e^{\pi/2} \approx 2.4\frac{M}{\omega}. \tag{7.29}$$

By this time it has been advected a distance $Mr_c/2$ at that depth. The ratio of this time to the Ekman layer formation time (7.25) is given by

$$\frac{t_v}{t_{Ek}} \approx 1.2M\frac{\Omega}{\omega}, \tag{7.30}$$

which for our experiments is much less than one. As the two processes are occuring simultaneously, it is apparent that our assumption in equation (7.28) that the Ekman layer is fully established before significant advection occurs is false. We therefore assume that a gravitationally unstable density profile forms immediately after the lid is turned on.

7.2 Convection theories

7.2.1 Critical Rayleigh number

We demonstrated in the previous section that once the lid is turned on, the standard Ekman layer will begin to form, and this will very quickly lead to a gravitationally unstable region as the dense fluid is advected across the front. If the width of this unstable layer is much wider than it is thick, then the situation is similar to that in Rayleigh-Bénard convection, where a fluid is heated from below or cooled from above to create a gravitationally unstable density field. Diffusion acts to counter the growth of perturbations in the temperature field, however it can not always act fast enough to stop convection. The ratio of the buoyancy driven vertical velocity to the velocity of thermal diffusion is given by the Rayleigh number

$$Ra = \frac{g\Delta\rho L^3}{\kappa\nu}, \tag{7.31}$$

where L is a vertical length scale corresponding to the density difference $\Delta\rho$. Convection occurs when the Rayleigh number is greater than a critical value R_c. For non-rotating convection, $R_c = 27\pi^4/4 \approx 658$ for two free boundaries, $R_c \approx 1100$ for one free boundary, and $R_c \approx 1708$ for two no slip boundaries (Chandrasekhar, 1961).

The addition of rotation to the Rayleigh-Bénard problem increases the critical Rayleigh number. Boubnov and Golitsyn (1986) showed that the critical Rayleigh number for a convective cell with stress free upper and lower boundaries is given by the formula

$$Ra_c = 3\pi^4[1/4 + \cosh(\phi/3) + \cosh^2(\phi/3)] \tag{7.32}$$

where

$$\phi = \cosh^{-1}(1 + 2\,Ta/\pi^4) \tag{7.33}$$

and where $Ta = 4\Omega^2 L^4/\nu^2$ is the Taylor number, proportional to the square of the inverse of the Ekman number. For large Taylor numbers ($Ta > 10^6$) the critical Rayleigh number approaches the asymptotic limit $Ra_c = 8.7\ Ta^{2/3}$. The Rayleigh number of cases involving one or two no-slip boundaries increase in a similar fashion.

Returning to the present problem, if the dense fluid that has crossed the front in the Ekman layer is able to diffuse its anomalous density into the underlying layer fast enough, then convection will not occur. By definition, the Ekman number based on the Ekman layer thickness is unity, and thus the Taylor number is also of order unity. Equation (7.32) indicates that the critical Rayleigh number is virtually unchanged from its non-rotating value when the Taylor number is this small. For all our experiments, the Rayleigh number based on the Ekman layer thickness ranges in size from 2400 to 80000, indicating that the statically unstable Ekman layer will convect, without the need for thickening of the unstable layer due to Ekman pumping.

7.2.2 Convection timescale

Having used the Rayleigh-Bénard theory in the previous section to show that convection is likely to occur, we now turn to Rayleigh-Taylor theory to predict how long it should take.

Youngs (1984) describes the (non-rotating) Rayleigh-Taylor instability as being a three stage process. In the first stage, a perturbation in the interface between the two layers starts growing exponentially. The growth rate depends on the wavelength of the perturbation. The smaller the wavelength of the perturbation, the larger the pressure gradient that acts to accelerate it. However, viscosity slows the growth rate of smaller wavelengths. These two effects result in a non-zero and finite fastest growing wavelength, which becomes the dominant wavelength of the growing perturbation. For a non-rotating, semi-infinite two layer density system, Chandrasekhar (1961) showed that this wavelength is given by

$$\lambda_m \approx 4\pi[\nu^2/gA]^{1/3}, \tag{7.34}$$

and has a growth rate of

$$n_m \approx \sqrt{g\pi A/\lambda_m}. \tag{7.35}$$

These equations lead to a timescale for the growing instability,

$$t_{\text{Chand}} \sim 2\pi \left(\frac{4\nu}{g'^2} \right)^{1/3}. \tag{7.36}$$

Hide (1956a,b) showed that rotation can slow down the process of convection, though the effect is not significant if the timescale for convection (equation 7.36) is much less than the inertial period. This is true for all but two of our experiments.

A further difficulty in applying (7.36) is the fact that the Ekman layer is thin, compared to the semi-infinite layers assumed in Chandrasekhar's theory. In particular, if the wavelength of the fastest growing instability is greater than the thickness of the upper unstable layer (which is the case for many of our experiments), then an alternative theory is required. Kerr (1994), following from Lister and Kerr (1989), presents a non-rotating theory for the convecting timescale of a very thin layer overlying a much thicker layer

$$t_K \approx 10.3\nu/(g'h), \tag{7.37}$$

where h is the thickness of the thin layer. The fastest growing wavelength is given by

$$\lambda_m \approx 1.1822\pi h. \tag{7.38}$$

As with the timescales predicted by Chandrasekhar, none of the times predicted by (7.37) for our experiments are significantly greater than the rotation period. Hence the effect of rotation should not alter these predicted timescales greatly.

The second stage of Rayleigh-Taylor instability commences when the amplitude of the growing instability is of order $\lambda_m/2$. The growth rate slows as the instabilities interact, and the wavelength of the dominant instabilies grow. Scaling analysis shows that the growth velocity of the mixed region is of order $(\nu Ag)^{1/3}$, which implies that the time duration of this second stage is proportional to the duration of the first stage, (7.36).

When the amplitude of the growing instability is of order $10\lambda_m$, the convection enters its third phase. At this stage, the initial conditions are forgotten, viscosity is no longer important, and the thickness, Z, of the mixed layer between the two fluids

grows according to

$$Z = \alpha A g t^2, \tag{7.39}$$

where α is a constant which may depend on the density ratio. For rotating Rayleigh-Taylor instability, α may also depend on the time (measured in inertial periods). Many studies have investigated the value of α for non-rotating convection, using experimental, theoretical and numerical methods (see (Glimm, Grove, Li, W., and Sharp, 2001) for a review), with most predicting values of between 0.03 and 0.07. Hereafter, we shall use $\alpha_0 = 0.05$ as an appropriate value for α for non-rotating convection.

In the present experiments, the thickness of the upper layer, $\sim h_0$, is much greater than the wavelength of the fastest growing instability, λ_m, predicted by either equation (7.34) or (7.38). Thus (7.39) can be rearranged to give a timescale for convection to fill the depth of the upper layer whilst in the third stage of the Rayleigh-Taylor instability process[2],

$$t_3 = \sqrt{h_0/(\alpha A g)}. \tag{7.40}$$

Using a value of $\alpha = \alpha_0$, (7.40) gives timescales of between 3 and 9 seconds for our experiments. This is much greater than the growth rate timescales of 0.1 to 0.5 seconds predicted for t_{Chand} by equation (7.36) and 0.1 to 2.1 seconds for t_k predicted by (7.37) for the first stage of the Rayleigh-Taylor instability process. The second stage is likely to take roughly as long as the first stage. We conclude that most of the time taken for convection to envelop the full depth of the upper layer will be spent in the third phase of Youngs' description of Rayleigh-Taylor instability.

[2]The unstable layer in our experiments is much thinner than the upper layer ($\delta \ll h_0$). This means that we cannot be sure the mixed region will continue to grow at the rate predicted by (7.39) once its thickness exceeds the Ekman layer thickness. Effectively, the convection runs out of dense fluid to drive it. However, as we shall see in section 8.1, (7.40) proves to be a good prediction of the measured instability timescale, suggesting that the relative thinness of the unstable layer may not be important.

Chapter 8

Experimental results

For each experiment, measurements were taken of the time it took for the onset of convection, and the increase in mass, volume and potential energy of the mixed fluid. I was interested in the dependence of these quantities on the lid rotation rate, density difference, viscosity and diffusivity. The convection timescale and the production of mixed fluid might also have depended on the tank rotation rate and the volume of the upper layer, which together determine the radius of the front and the depth of the upper layer. Experimental difficulties meant that it was difficult to explore the dependence of the results on these parameters. The difficulties mostly related to the process of spinning the fluid up to solid body rotation with minimal mixing between the two layers. Diffusion alone caused a blurring of the interface while spin-up was occuring, though other mixing processes were likely to be present. The influence of this region of mixed fluid was minimised if the upper layer had a large volume. However, the interface between the two layers was required to outcrop on the lid of the tank. The larger the volume of the upper layer, the faster the tank rotation rate required to satisfy this condition. A faster rotation rate would increase the time needed to spin up the tank, and this would create more mixing during spin-up.

A volume of seven litres for the upper layer and a tank rotation rate of 2.2 rad/s gave a reasonable compromise between the condition that the front out-crop on the lid and maximising the volume of the upper layer (so that the inevitable mixing and diffusion that occurred during the set-up of the experiment had minimal impact). Given the experimental difficulty of varying these parameters significantly, in addition to time considerations, I decided to use the same rotation rate and upper layer volume for all experiments. This meant that the frontal radius and upper layer depth was also

constant. The values of all other parameters are given in Table 8.1.

8.1 Time for convection to develop

For each forcing event, measurements were taken of the time, t_E, for convection to develop. As a practicality, this was defined as the time interval between starting the lid and convection engulfing the upper layer (Table 8.1). Tests were made to see if these times were affected by turning the lid off before convection started. It was found that convection still occurred, and the times were not appreciably different. This confirmed the prediction from section 7.2.1 that the initial thickness of the unstable layer, the Ekman layer thickness, was sufficiently large for instabilities to form (ie. $\mathrm{Ra} \gg \mathrm{Ra_c}$). It did not have to be thickened through the process of Ekman pumping.

In section 7.2.2 it was predicted that throughout the majority of the measured convection timescale, the Rayleigh-Taylor instability would be in the third stage of its evolution (Youngs, 1984), when the convection is growing according to a power law (7.39). It followed that the convection timescale would be given by $t_3 = \sqrt{h_0/(\alpha_0 A g)}$, (7.40). This prediction is supported by multivariable analysis, which indicates that the best fitting power law between the measured timescale and the variables of the experiments is given by

$$t_E \sim \Delta\rho^{-0.61\pm.07}\omega^{-0.06\pm.09}\nu^{0.01\pm.03}\kappa^{0.02\pm.12}. \tag{8.1}$$

Thus the timescale is virtually independent of lid rotation rate, viscosity and diffusivity, but increases with decreasing density difference. The dependence on the density difference is slightly stronger than the $-\frac{1}{2}$ power of (7.40). I attribute this discrepancy to the early stage of the convection being governed by the exponential growth that occurs during the first stage of the Rayleigh-Taylor instability, noting that equations (7.36) and (7.37) predict the timescale of this first stage to be proportional to $\Delta\rho^{-2/3}$ and $\Delta\rho^{-1}$ respectively. The early growth phase of the Rayleigh-Taylor instability might also lead to the tiny positive exponent of viscosity present in the results.

The correlation between (7.40) and the measured convection timescale is also sup-

Properties and parameters									Results				
Exp. No.	$\Delta\rho$ kg/m^3	ω s^{-1}	ν 10^{-6}m^2/s	κ 10^{-9}m^2/s	ϵ	Re	Ro	Pr	t_E s	MixMass1 increase	MixMass2 increase	Volume increase	PE increase
36	6.59	0.18	1.0	1.5	0.30	70	0.082	670	12 ± 2	0.38	0.33	0.64	0.08
37	4.06	0.18	1.0	1.5	0.24	53	0.082	670	19 ± 2	0.45	0.36	0.80	0.09
38	4.06	0.13	1.0	1.5	0.23	55	0.059	670	18 ± 2	0.40	0.36	0.85	0.09
39	4.05	0.08	1.0	1.5	0.23	62	0.036	670	20 ± 3	0.28	0.26	0.59	0.08
40	3.11	0.18	1.0	1.5	0.21	46	0.082	670	24 ± 3	0.38	0.32	0.85	0.09
41	3.10	0.12	1.0	1.5	0.21	46	0.055	670	24 ± 3	0.33	0.28	0.78	0.09
42	1.79	0.18	1.0	1.5	0.15	42	0.082	670	34 ± 4	0.53	0.36	0.87	0.10
43	9.22	0.18	1.0	1.5	0.37	70	0.082	670	12 ± 2	0.44	0.28	0.61	0.06
44	5.89	0.18	1.0	1.5	0.30	54	0.082	670	15 ± 2	0.31	0.23	0.57	0.07
45	5.89	0.18	1.0	1.5	0.31	53	0.082	670	14 ± 2	0.22	0.19	0.61	0.07
46	5.90	0.12	1.0	1.5	0.30	57	0.055	670	16 ± 2	0.37	0.25	0.71	0.07
47	2.29	0.18	9.0	1.5	0.19	3.9	0.082	6000	26 ± 3	0.18	0.10	0.35	0.040
48	2.31	0.13	9.0	1.5	0.19	4.0	0.059	6000	27 ± 3	0.15	0.09	0.32	0.037
49	6.48	0.20	9.0	1.5	0.31	7.0	0.091	6000	15 ± 2	0.11	0.067	0.21	0.030
50	6.59	0.10	9.0	1.5	0.30	7.4	0.045	6000	18 ± 2	0.10	0.061	0.20	0.028
53	9.23	0.18	1.0	0.61	0.37	74	0.082	1640	8 ± 1	0.27	0.18	0.54	0.06
54	13.33	0.18	1.0	0.61	0.44	87	0.082	1640	8 ± 1	0.19	0.14	0.40	0.05
55	17.60	0.18	1.0	0.61	0.51	100	0.082	1640	6 ± 1	0.23	0.16	0.35	0.044
57	4.17	0.06	1.0	1.5	0.24	52	0.027	670	19 ± 2	0.43	0.27	0.67	0.07
58	4.19	0.10	1.0	1.5	0.24	53	0.045	670	17 ± 2	0.36	0.26	0.60	0.08

Table 8.1: Experimental properties and results. All experiments had a rotation rate $\Omega = 2.2$ rad/s, a frontal radius $r_c \approx 36.6$ cm, and a depth $h_0 \approx 3.32$ cm.

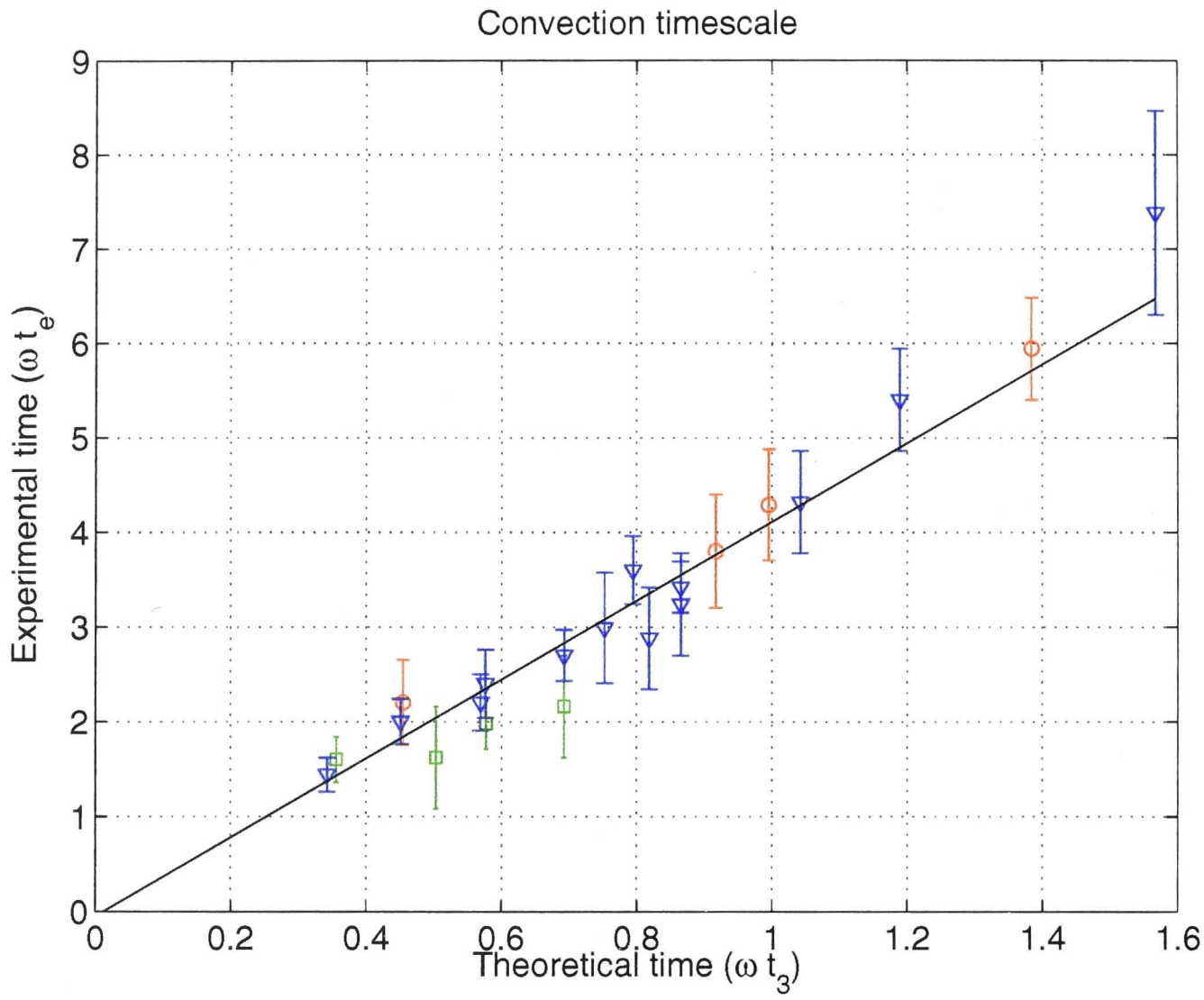

Figure 8.1: Time for convection to occur versus the theoretical time given by equation (7.40), with $\alpha = \alpha_0 = 0.05$. The red data (circles) represent experiments with increased viscosity ($\nu = 9 \times 10^{-6}\mathrm{m}^2/\mathrm{s}$), green (squares) represents reduced diffusivity data ($\kappa = 0.61 \times 10^{-9}\mathrm{m}^2/\mathrm{s}$), while the blue (triangles) data points have standard viscosity and diffusivity ($\nu = 1 \times 10^{-6}\mathrm{m}^2/\mathrm{s}$ and $\kappa = 1.5 \times 10^{-9}\mathrm{m}^2/\mathrm{s}$).

ported by figure 8.1. To within the experimental uncertainty, the line of best fit through the data intersects the origin. Given that both times were non-dimensionalised by the lid rotation rate, the direct relationship between the theoretical and experimental data suggests that there was minimal lag between turning the lid on, and instabilities starting to grow. This is in agreement with the prediction, from equation (7.30), that density inversions should form quickly compared to the Ekman layer formation time, which in turn should be much shorter than the measured convection timescales. To emphasise this point, the timescale for convection was the time since the lid was turned on; it was not measured from the time at which the density anomaly arrived at any particular distance from the front.

There is approximately a factor of 4 difference between the theoretical and experi-

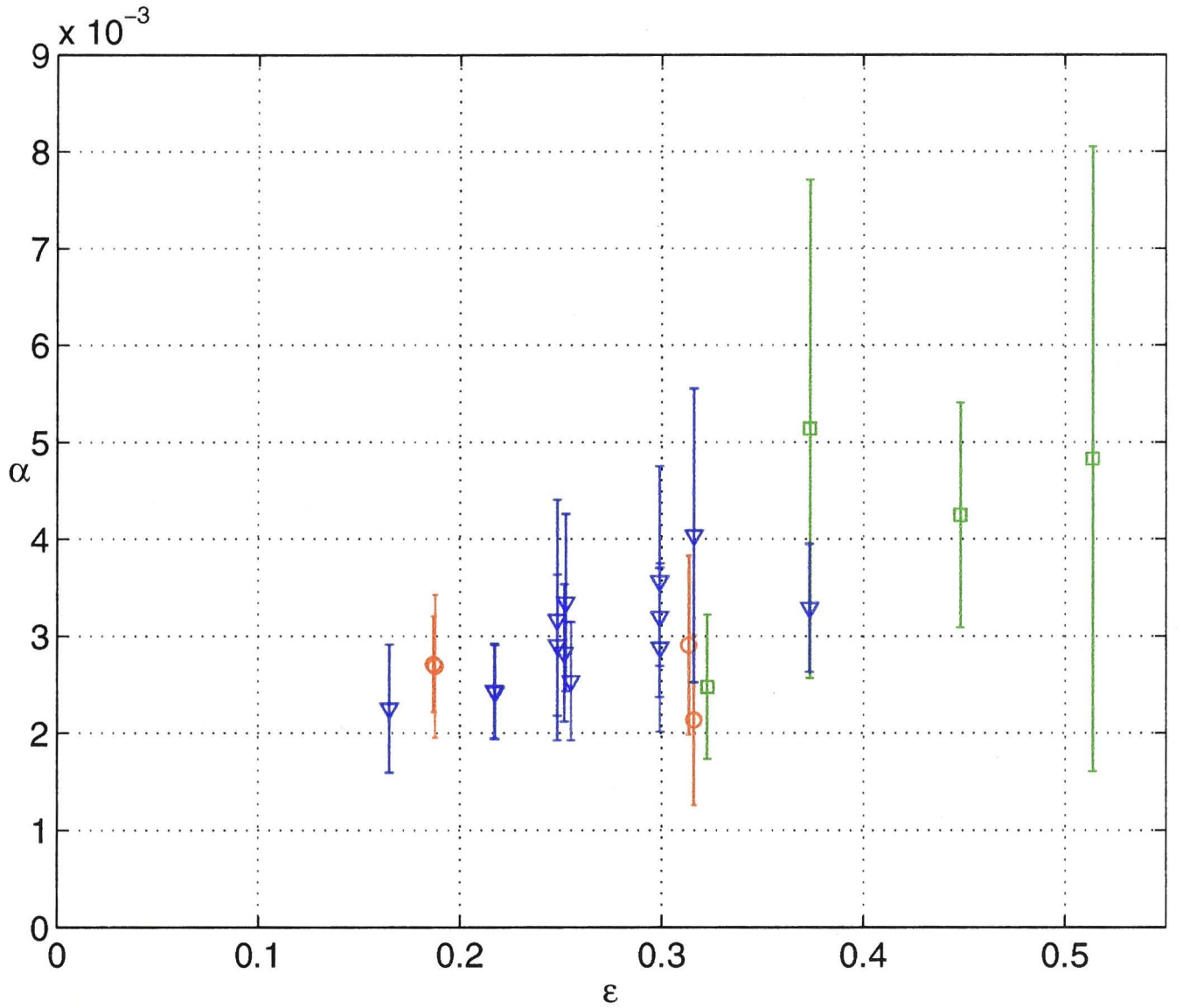

Figure 8.2: Plot of α (the empirical constant in the equation for the thickness for the mixed region, 7.39) versus the convective Rossby number, ϵ. The red data (circles) represent experiments with increased viscosity ($\nu = 9 \times 10^{-6}\mathrm{m}^2/\mathrm{s}$), green (squares) represents reduced diffusivity data ($\kappa = 0.61 \times 10^{-9}\mathrm{m}^2/\mathrm{s}$), while the blue (triangles) data points have standard viscosity and diffusivity ($\nu = 1 \times 10^{-6}\mathrm{m}^2/\mathrm{s}$ and $\kappa = 1.5 \times 10^{-9}\mathrm{m}^2/\mathrm{s}$).

mental times in figure 8.1. This is not surprising, as the theoretical values were calculated using $\alpha_0 = 0.05$, a value found to be appropriate for non-rotating Rayleigh-Taylor convection. Empirical values for α for the rotating experiments may be determined by rearranging (7.40),

$$\alpha = \frac{2h_0}{g' t_E^2}. \tag{8.2}$$

We would expect to find $\alpha \approx \alpha_0$ when the ratio of the theoretical timescale (7.40) and the inertial period is much less than one. This ratio may be represented by a *convective*

Rossby number (Julian et al., 1996; Gilman, 1977), defined by

$$\epsilon = \frac{1}{2\Omega}\sqrt{\frac{g'}{h_0}} \propto (\Omega t_3)^{-1}. \tag{8.3}$$

From the preceding arguments we predict that calculated values of α will be significantly different to α_0 when $\epsilon < (2\pi^2\alpha_0)^{-1/2} \approx 1$. Figure 8.2 shows the empirical values of α versues ϵ. All the convective Rossby numbers were much less than 1, suggesting that rotation was important for all the experiments. Indeed, the rotation has significantly slowed the convection timescales, resulting in small values of $\alpha \approx 0.003$. The measured value of α seems to increase with increasing ϵ, though it is speculation as to whether it would increase all the way to $\alpha \approx 0.05$ in the limit of infinite ϵ (ie. no rotation). There is certainly scope for exploring these larger convective Rossby numbers, although as mentioned at the start of this chapter, significant experimental difficulties arise in trying to achieve this through reducing the tank rotation rate or reducing the thickness of the upper layer. Also, as indicated by the size of the errorbars in figure 8.2, relative experimental uncertainty becomes greater when trying to measure smaller convection timescales (larger ϵ).

8.2 Increase in mixed water due to the forcing event

8.2.1 Dimensional analysis

The production of mixed fluid is expected to depend on the seven variables

$$g',\ \nu,\ \kappa,\ \omega,\ \Omega,\ r_c,\ h_0. \tag{8.4}$$

These seven variables involve two dimensions: length and time. According to the Buckingham Pi theorem, the results should depend on five independent dimensionless parameters expressed in terms of these variables. There are many combinations possible, but the five I chose are the Reynolds, convective Rossby, Prandtl, Burger and

forcing Rossby numbers, defined as follows:

$$Re = \sqrt{\frac{\alpha g' h_0^3}{2\nu^2}}, \quad \epsilon = \frac{1}{2\Omega}\sqrt{\frac{g'}{h_0}}, \quad Pr = \frac{\nu}{\kappa}, \quad Bu = \frac{g' h_0}{4\Omega^2 r_c^2}, \quad Ro = \frac{\omega}{\Omega}. \tag{8.5}$$

The velocity scale used to produce the Reynolds number[1] is based on the vertical velocity of the growing mixed region. The vertical velocity is calculated by dividing the thickness of the upper layer, h_0, by the time it takes convection to encompass the upper layer, $t_3 = \sqrt{2h_0/(\alpha g')}$ (7.40). I have used $\alpha = 3 \times 10^{-3}$, found to be appropriate for most of the experiments (see Figure 8.2).

As mentioned at the start of this chapter, experimental difficulties made it difficult to explore a large range of rotation rates and upper layer volumes. It was decided to keep these parameters constant for all experiments. This resulted in the Burger number always being directly related to the convective Rossby number, due to the relationship

$$\frac{Bu}{\epsilon^2} = \left(\frac{h_0}{r_c}\right)^2, \tag{8.6}$$

where the right hand side was not varied between experiments. Thus, the Burger number and ϵ were not varied independently in the present experiments, so it was not possible to distinguish between the effect of changing the Burger number and the effect of changing ϵ. However, the results were expected to be essentially independent of the Burger number. This is because the Burger number represents the square of the ratio of the Rossby radius, $\sqrt{g' h_0}/(2\Omega)$, to the frontal radius, r_c. The importance of this ratio is that during convection, mixed fluid will spread out for a distance equal to the Rossby radius from its source region (if it is unimpeded by a boundary or stratification). Therefore, if the Burger number is much less than one, or more particularly, if $\sqrt{Bu} \ll 1$, there is plenty of room for the mixed fluid to spread unimpeded. In the present experiments, $\sqrt{Bu} < 0.05$, so this relationship is satisfied. The Burger number is not expected to be important beyond this criterion[2].

[1] The Reynolds number, as it is defined here, may also be thought of as proportional to the square root of the Grashof number ($Gr = Ra/Pr$).

[2] Another interpretation of the Burger number is that it represents the square of the ratio of the Rossby radius to the frontal length, $2\pi r_c$. If there is a thermal wind balance across the front, then baroclinic instability will lead to eddies forming along the front. The scale of these eddies is the

A similar argument applies to the forcing Rossby number. In the present experiments, the forcing Rossby number was always small ($Ro < 0.1$). The small forcing Rossby numbers meant that the horizontal acceleration terms *due to the lid forcing* were negligible in the momentum equations. Subsequently, the value of the forcing Rossby number was unimportant. Note that this is not to imply that the acceleration terms in the momentum equation were unimportant when convection was occuring. They were, though they depended on the *convective* Rossby number, ϵ.

The convective events in the experiments were turbulent. Production of mixed fluid is expected to occur primarily through turbulent mixing processes, rather than through molecular diffusion. Therefore, the results are not expected to be highly dependent on the molecular diffusivity, or in terms of dimensionless parameters, the Prandtl number is not important. This is not to imply that viscosity is also unimportant. The influence of viscosity is expected to be seen through the Reynolds number.

To summarise, the mixed fluid production results are not expected to depend heavily on the Burger, forcing Rossby or Prandtl numbers. As it is not possible to distinguish between the effects of the Burger number and ϵ, in the following sections it is assumed the influence of the Burger number is negligible. It was possible to analyse the dependence of forcing Rossby and Prandtl numbers, so those parameters have been included in the analysis.

8.2.2 Mixed water mass increase

In this section we investigate the increase in the mass of mixed fluid in the tank resulting from a lid forcing event. There are a variety of methods to measure the mass of mixed fluid between two nearly homogeneous layers. Two methods were chosen, and are illustrated in figure 8.3, where two identical vertical density profiles are shown to represent a partially mixed two-layer fluid. Before mixing, the upper layer density was ρ_1, while the lower layer had density ρ_2.

The first method, which I call MixMass1, is simply the integration of the density

---

Rossby radius, so the Burger number is inversely related to the number of eddies that lie along the front. However, the forcing events of these experiments are sufficiently short that baroclinic instability does not play a significant role during the convective event. Thus, this interpretation of the Burger number is mostly irrelevant to the present experiments.

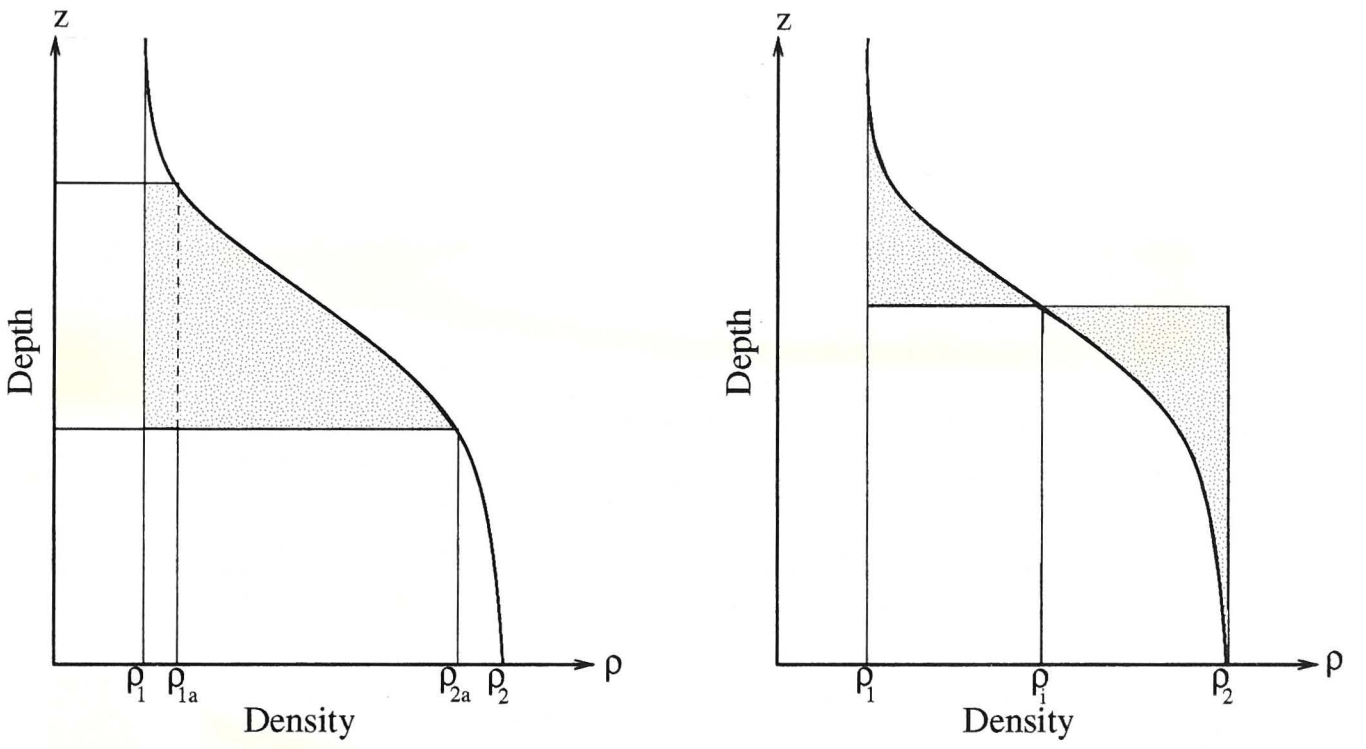

Figure 8.3: Schematic of two different ways of measuring the mass of mixed fluid. The shaded area on the left represents MixMass1, while the shaded area on the right represents MixMass2.

field (or more precisely $\rho - \rho_1$) between two isopycnals of density ρ_{1a} and ρ_{2a}. The second method, called MixMass2, is an integration of the difference between the actual density profile and a hypothetical unmixed density field. The unmixed density field is given by

$$\rho_i = \begin{cases} \rho_2 & \text{if } \rho > \rho_i \\ \rho_1 & \text{otherwise} \end{cases} \tag{8.7}$$

For the results I have used $\rho_i = (\rho_1 + \rho_2)/2$.

Figure 8.4 shows an example of an artificially coloured digital picture taken 50 minutes into experiment 35, before a lid forcing event has taken place. The raw pixel intensity is processed to produce a density image, which is then used to calculate MixMass1 and MixMass2. Figure 8.5 shows an image similarly processed, but taken 120 minutes into the same experiment and 30 minutes after a one minute forcing event. The increased amount of mixed fluid near the frontal region is clearly visible.

In both methods of calculating the mass of mixed fluid, the density fields were assumed axisymmetric, and were integrated over the volume of the tank. This yielded the mass of the mixed fluid, which was nondimensionalised using the Ekman layer anomalous mass transport across the initial position of the front, M, defined by

$$M = Q_{\text{Ek}}\, \Delta\rho\, t_f = \pi r_c^2\, \omega\, \delta\, \Delta\rho\, t_f. \tag{8.8}$$

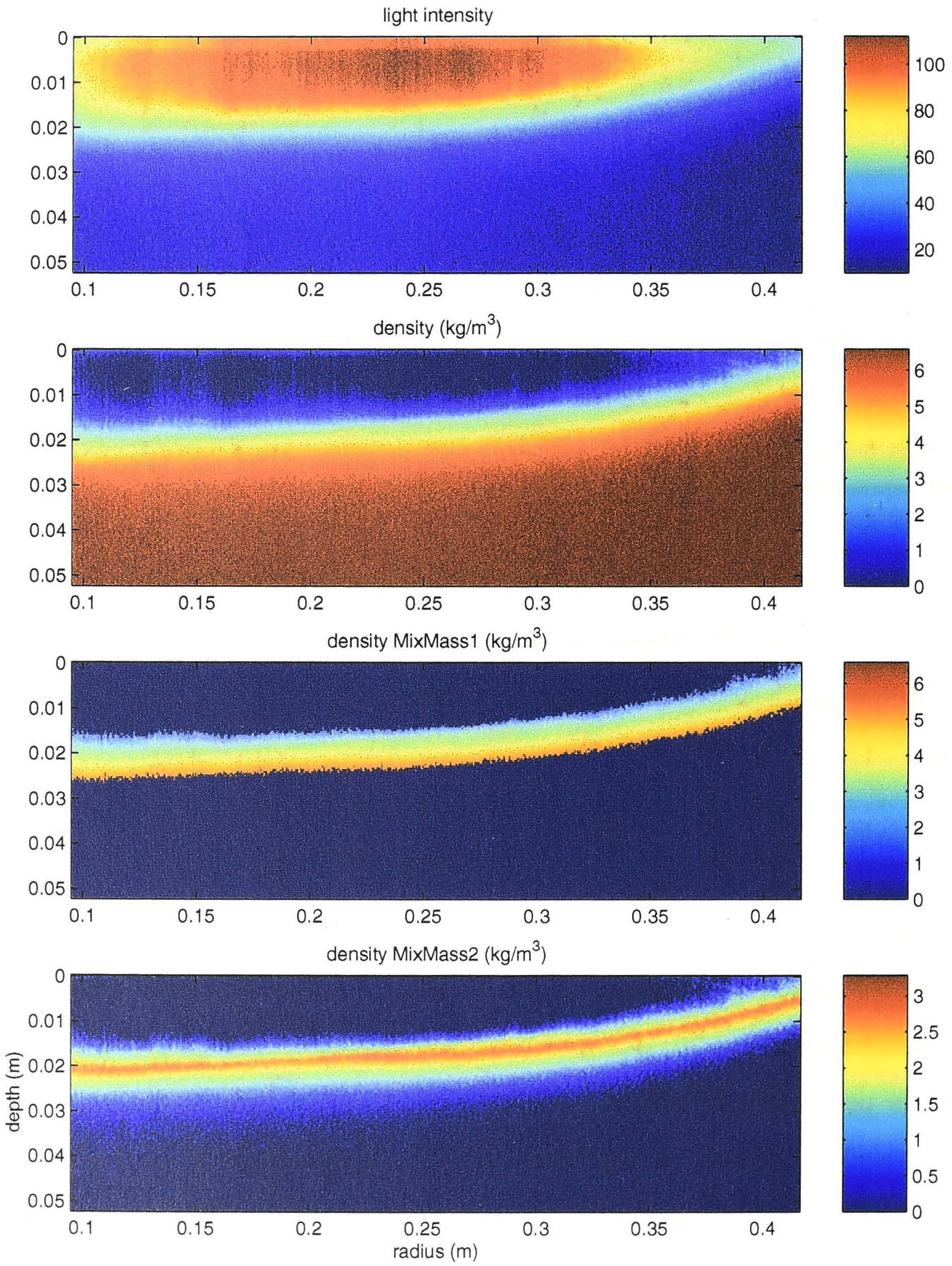

Figure 8.4: An example of an image taken from experiment 35 before the forcing event. The original pixel intensity is used to calculate the density field of the tank, which in turn is used to calculate the mass of mixed fluid using either of the two methods MixMass1 and MixMass2. This image was taken 50 minutes into the experiment, which was before the minute-long forcing event, which occurred 90 minutes into the experiment.

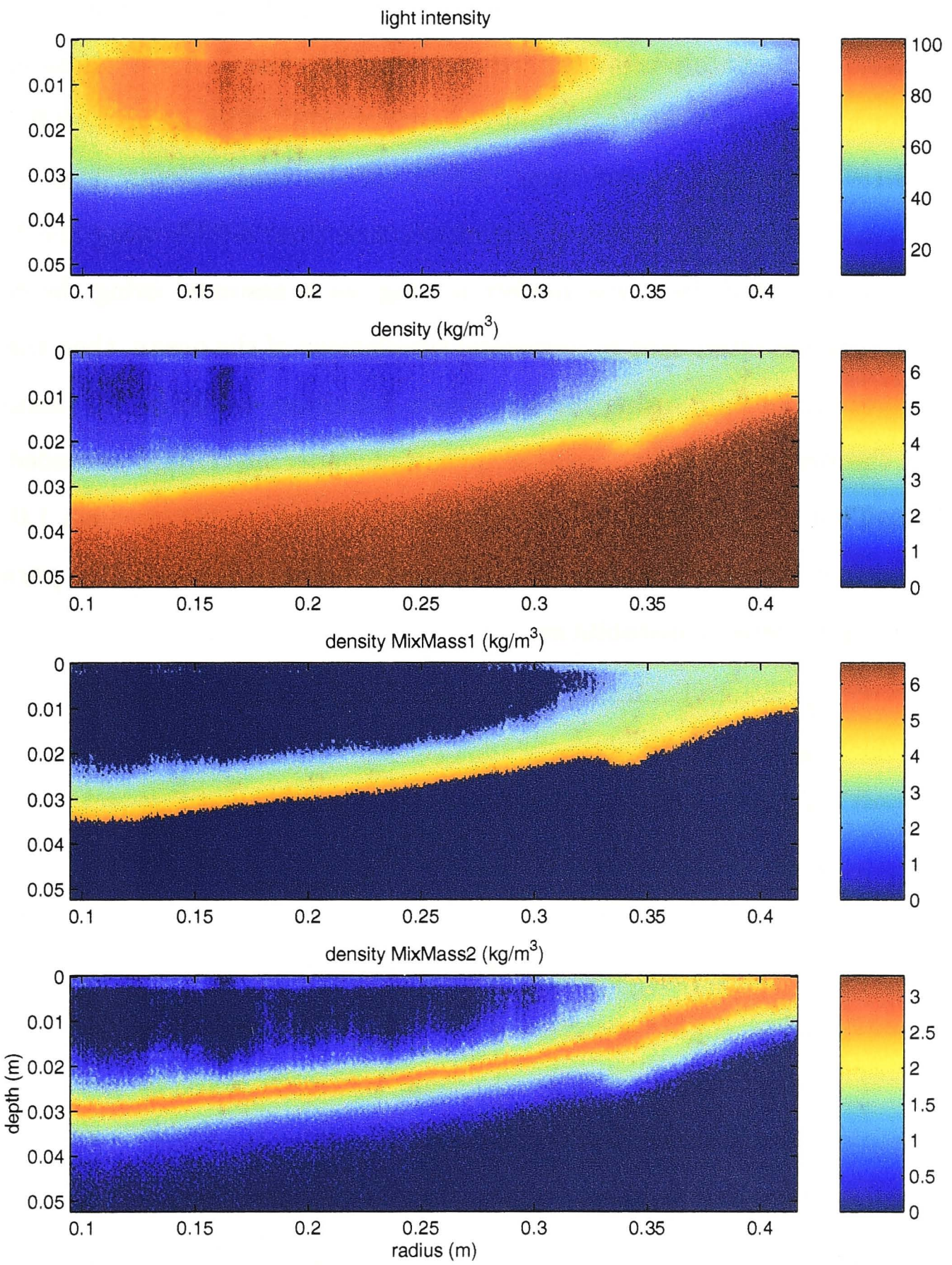

Figure 8.5: An example of an image taken from experiment 35 after the forcing event. The original pixel intensity image is used to calculate the density field of the tank, which in turn is used to calculate the mass of mixed fluid using either of the two methods MixMass1 and MixMass2. This image was taken 120 minutes into the experiment, 30 minutes after the minute-long forcing event, which occurred 90 minutes into the experiment.

A value for this non-dimensional mass was calculated at 5 minute intervals throughout each experiment. Figure 8.6 shows an example from experiment 36, which had a one minute forcing event 62 minutes into the experiment. The increase in the mass of mixed fluid immediately after the forcing event is clear. The dimensionless mass increases for all the experiments, obtained from graphs similar to figure 8.6, are given in Table 8.1. The values ranged from 10-53% (of the total Ekman layer anomalous mass transport) using the MixMass1 definition, and from 6-36% using the MixMass2 definition. Note that if there was perfect mixing, as is assumed using the convective adjustment schemes often used in numerical simulations of the ocean, then the increase in the mass of mixed fluid, using the MixMass1 definition, would be 1.0 (assuming the density of the perfectly mixed vertical column of upper layer fluid exceeded ρ_{1a}, see figure 8.3). That the experiments indicate a value significantly less than 1.0 suggests that a better method than the convective adjustment scheme is required to parameterise vertical mixing of density instabilities.

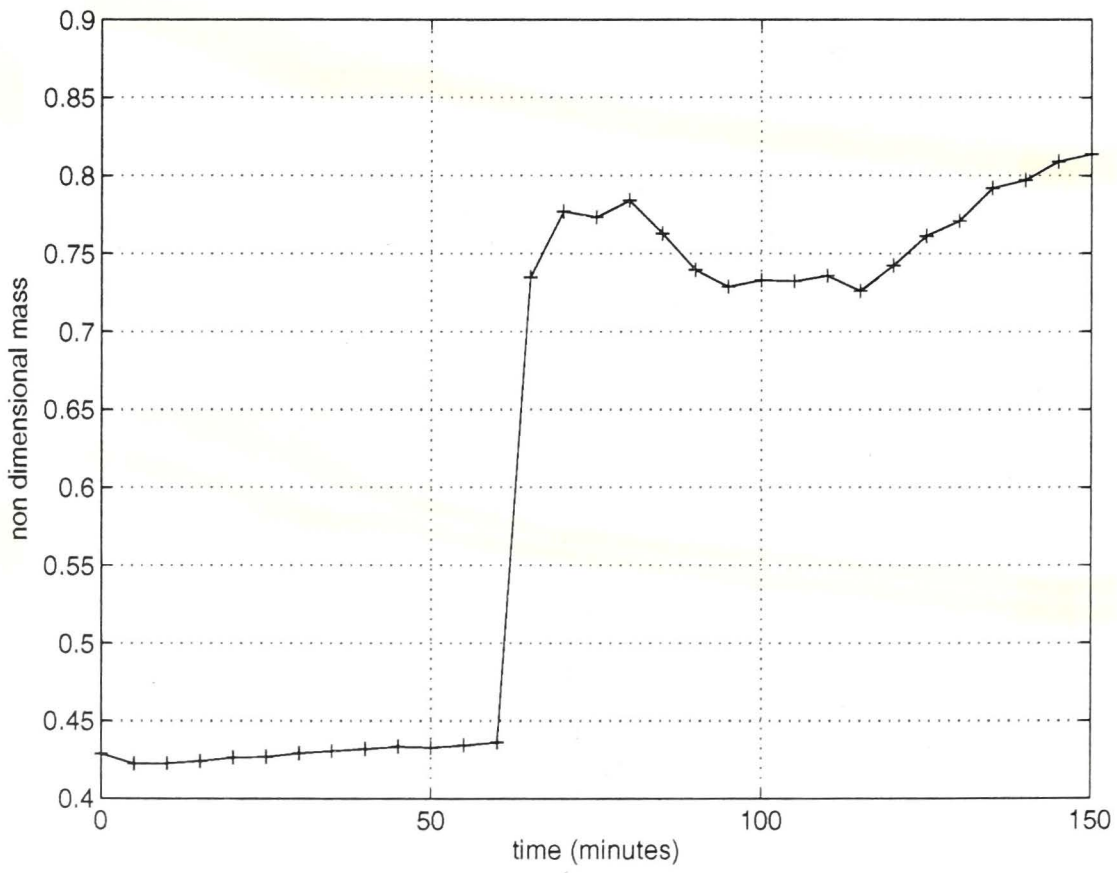

Figure 8.6: Plot showing the mass of the mixed fluid throughout experiment 36, using the MixMass2 definition. There was a one minute forcing event 62 minutes into the experiment.

In the experiments the parameters varied were the density difference $\Delta\rho$ between the two layers, the lid speed ω, the diffusivity κ, and the fluid viscosity ν. A power law of the form $\Delta\rho^{\alpha}\omega^{\beta}\kappa^{\gamma}\nu^{\delta}$ was fitted to the empirical values of the increase in mass of the mixed

fluid. The coefficients of the power law exponents are displayed in Table 8.2. It was assumed that the power law functional form would provide a reasonable description of the results over the range of parameters studied, and the resulting empirical exponents provide us with insight into the behaviour of the mixing. As is apparent from Table 8.2, the exponents for the power law fit were similar for both the MixMass1 and MixMass2 data. The parameter upon which they depended most strongly was viscosity, with a negative exponent indicating that increasing the viscosity of the fluid decreased the amount of mixed fluid produced. This may be explained by the fact that increasing the viscosity reduced the turbulence of the convection.

The variable that played the next most dominant role is the density difference $\Delta\rho$, with an exponent -0.41 and -0.36 for the MixMass1 and MixMass2 data respectively. The negative sign of the exponent may seem surprising, as one would expect a greater density difference to drive stronger convection, which would presumably lead to greater production of mixed fluid. However, a greater density difference also leads to convection developing more rapidly (as seen in section 8.1), which confines convection to a smaller region adjacent to the front. Thus the volume of fluid undergoing convection was reduced. A greater density difference also presented a larger potential energy barrier for mixing to overcome.

The normalised mass of mixed fluid produced also tended to increase as the lid rotation rate was increased, as evidenced by the lid rotation's positive exponent. There wasn't a strong dependence, and there was a large uncertainty in the exponent. Similarly, increasing the diffusivity also produced an increase in the normalised mass of mixed fluid, though the exponent was small, and its magnitude uncertain.

As discussed in section 8.2.1, the four variables in these experiments can be represented by four dimensionless numbers: the convective Rossby, Reynolds, Rossby and Prandtl numbers. A power law of the form $\epsilon^{\alpha} Re^{\beta} Ro^{\gamma} Pr^{\delta}$ was fit to the experimental data for MixMass1 and MixMass2. The best fitting exponents are given in Table 8.2. The convective Rossby number was the most influencial on the results, with the exponent being approximately -1.0 for both MixMass1 and MixMass2 data. The negative sign may seem surprising, as we have seen in figure 8.2 that the growth rate of the convective mixed region increases with increasing ϵ. Stronger convection at larger con-

Quantity	Best fitting power law
MixMass1	$\nu^{-0.45\pm.04}\Delta\rho^{-0.41\pm.08}\omega^{0.10\pm.12}\kappa^{0.01\pm.27}$
	$\epsilon^{-1.03\pm.34}Re^{0.25\pm.23}Ro^{0.11\pm.12}Pr^{-0.20\pm.25}$
	$\epsilon^{-1.27\pm.16}Re^{0.43\pm.03}$
MixMass2	$\nu^{-0.59\pm.03}\Delta\rho^{-0.36\pm.08}\omega^{0.16\pm.11}\kappa^{0.24\pm.20}$
	$\epsilon^{-1.07\pm.28}Re^{0.36\pm.17}Ro^{0.17\pm.10}Pr^{-0.22\pm.18}$
	$\epsilon^{-1.29\pm.15}Re^{0.56\pm.03}$
Mixed volume	$\nu^{-0.43\pm.03}\Delta\rho^{-0.36\pm.06}\omega^{0.11\pm.09}\kappa^{0.09\pm.17}$
	$\epsilon^{-0.79\pm.21}Re^{0.14\pm.14}Ro^{0.13\pm.09}Pr^{-0.30\pm.16}$
	$\epsilon^{-1.15\pm.12}Re^{0.40\pm.03}$
Potential energy	$\nu^{-0.41\pm.02}\Delta\rho^{-0.25\pm.03}\omega^{0.18\pm.05}\kappa^{0.19\pm.08}$
	$\epsilon^{-0.65\pm.13}Re^{0.16\pm.08}Ro^{0.20\pm.06}Pr^{-0.24\pm.08}$
	$\epsilon^{-1.04\pm.07}Re^{0.40\pm.03}$

Table 8.2: Power law fit to experimental data, as a function of dimensional and dimensionless experimental parameters. The dimensionless numbers are defined in equations (8.5).

vective Rossby number also leads to increased heat transfer in rotating Raleigh-Bénard simulations (Cabot et al., 1992). I postulate that the increasing importance of rotation in experiments with small ϵ leads to greater vorticity in the convective plumes, which entrains more of the ambient fluid and produces greater levels of mixing. Indeed, the convection is slower *because* of the complicated plume structures that produce more mixing at smaller convective Rossby numbers.

Similarly, increasing the Reynolds number increases the turbulence, which also leads to a greater mass of mixed fluid. This is confirmed by the positive exponent given in Table 8.2 for the Reynolds number, which the results suggest is the second most important parameter.

It was predicted in section 8.2.1 that the forcing Rossby number and Prandtl numbers would not play a dominant role in the production of mixed fluid. Table 8.2 indicates that increasing the forcing Rossby number and decreasing the Prandtl number increased the mass of mixed fluid produced. However, there is a large degree of uncertainty in the exponents, and they are the least important of the four parameters studied. The possibility that the increase in mass of the mixed fluid might be independent of forcing Rossby and Prandtl number led us to find the best fitting power law of the form $\epsilon^{\alpha} Re^{\beta}$. The result is also shown in Table 8.2, and is plotted in Figure 8.7. As with the four parameter case, an increase in ϵ (at constant Re) leads to a smaller mass of mixed fluid being produced, while an increase in Re (at constant ϵ) leads to a greater mass produced. The exponents increase in magnitude when the influence of forcing Rossby and Prandtl numbers is ignored.

Figure 8.8 shows the same data as figure 8.7, though the x axis now incorporates the effect of changing both ϵ and Re, through the quantity $\epsilon^{-1.29} Re^{0.56}$. If the power law given in Table 8.2 fit the data exactly, then all the data points would collapse onto a straight line.

8.2.3 Volume of the mixed water

The volume of mixed fluid was defined to be the volume of fluid which has a density between the same two limits used to define MixMass1 in the previous section. These volumes were then non-dimensionalised by the Ekman volume flux crossing the density

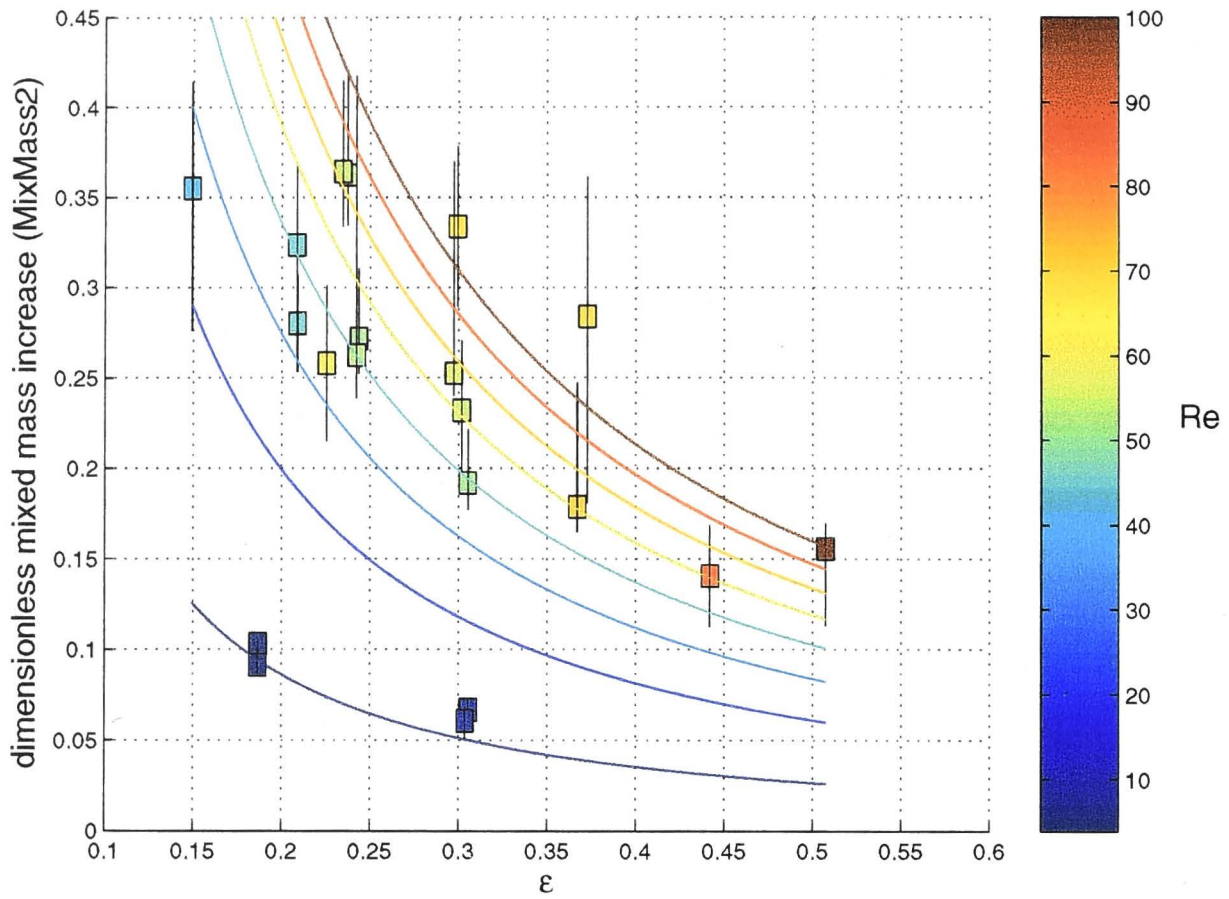

Figure 8.7: The dimensionless increase in the mass of mixed fluid due to the forcing event, versus the convective Rossby number. Each data point is coloured according to the Reynolds number, as determined by the colour bar. The family of curves are the best fitting power law curves, as given in Table 8.2, coloured in the same fashion as the data points.

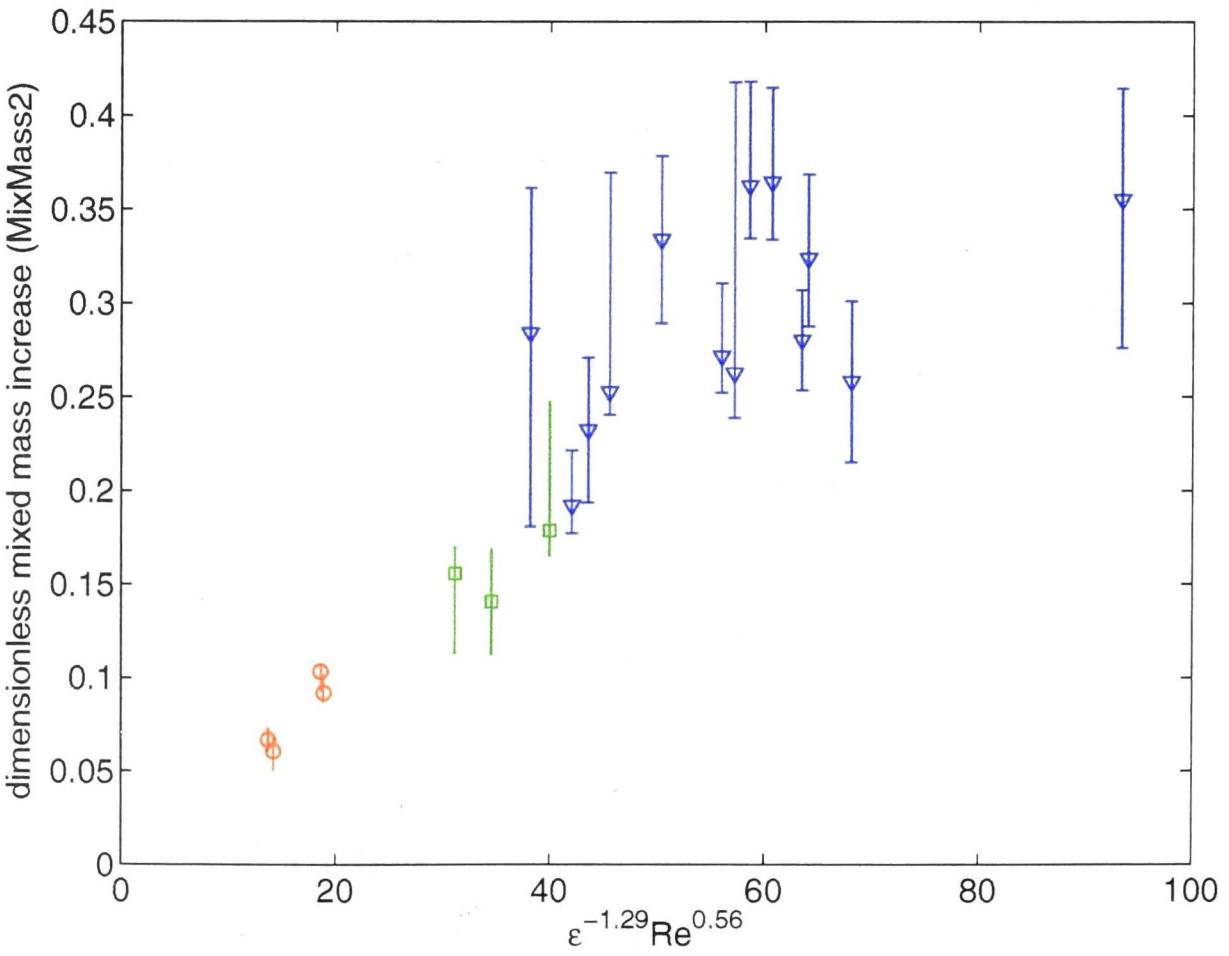

Figure 8.8: The dimensionless increase in the mass of mixed fluid due to the forcing event, versus $\epsilon^{-1.29}Re^{0.56}$. The red data (circles) represent experiments with increased viscosity ($\nu = 9 \times 10^{-6}\mathrm{m}^2/\mathrm{s}$), green (squares) represents reduced diffusivity data ($\kappa = 0.61 \times 10^{-9}\mathrm{m}^2/\mathrm{s}$), while the blue (triangles) data points have standard viscosity and diffusivity ($\nu = 1 \times 10^{-6}\mathrm{m}^2/\mathrm{s}$ and $\kappa = 1.5 \times 10^{-9}\mathrm{m}^2/\mathrm{s}$).

front (7.26), multiplied by the forcing time:

$$Q_{\mathrm{Ek}}\, t_f = \pi\, r_c^2\, \omega\, \delta\, t_f. \tag{8.9}$$

The measured dimensionless volume increases are shown in Table 8.1. They ranged from 0.2 to 0.87. Thus the increase in volume of mixed fluid due to the lid forcing event is 20-85% of the cross frontal Ekman layer volume flux during that forcing event[3]. The dimensionless volume increases are approximately twice the corresponding MixMass1 values. This is because the average density of the mixed fluid using the MixMass1 data is approximately $\Delta\rho/2$.

As in the previous section, the best fitting power law curves to the data were determined for the dimensionless volume increase of mixed fluid. The resulting exponents are displayed in Table 8.2. The exponents are similar to those obtained from the dimensionless mass of mixed water data. The increase in the volume of mixed fluid decreased with increasing viscosity and density difference, but increased with increasing diffusivity and lid rotation rate. In terms of dimensionless numbers, the volume of mixed fluid decreased with increasing convective Rossby and Prandtl numbers, and increased with increasing Reynolds and forcing Rossby numbers. For an explanation of these results the reader is referred to section 8.2.2.

The expectation that the dimensionless volume increases were independent of forcing Rossby and Prandtl numbers, led us to analysing the data in terms of only convective Rossby and Reynolds numbers. The results are shown in Table 8.2, and in figures 8.9 and 8.10. Although it is difficult to predict from these two figures that the degree of fit of the data to the power curves is any worse than the corresponding figures from the MixMass2 data, the exponents for Ro and Pr in Table 8.2 suggest that the forcing Rossby and Prandtl number played a more significant role in the volume data than they did in the MixMass data. Figure 8.11 therefore shows the influence of all four variables on the one plot, with the x axis data obtained from $\epsilon^{-0.79} Re^{0.14}$, and the data coloured according to $Ro^{-0.13} Pr^{-0.30}$.

[3]Note that it is possible to obtain dimensionless volume increases of greater than 100%. For example if there was perfect mixing between the entire Ekman volume flux and an equal volume of upper layer fluid, then the dimensionless increase in the volume of mixed fluid would be 200%

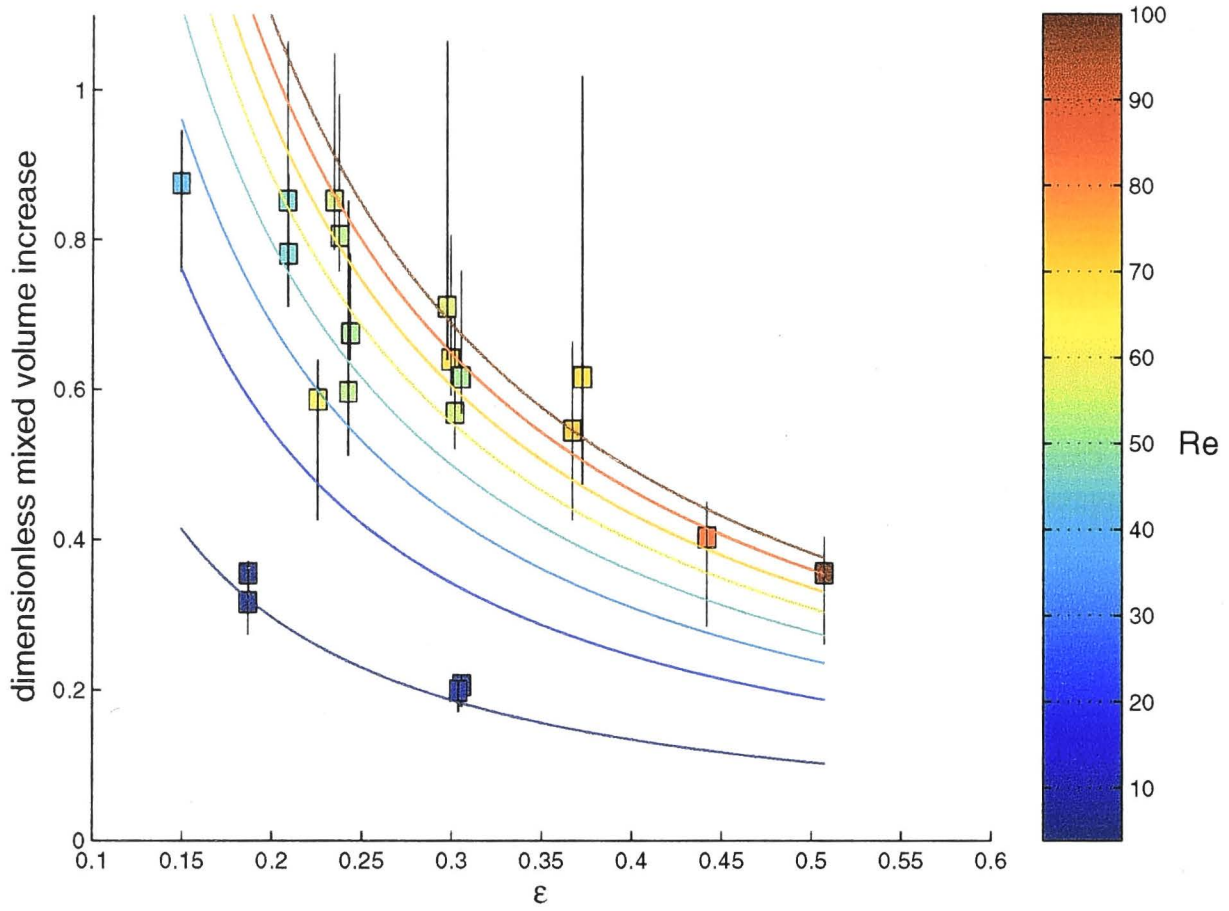

Figure 8.9: The dimensionless increase in the volume of mixed fluid due to the forcing event, versus the convective Rossby number. Each data point is coloured according to the Reynolds number, as determined by the colour bar. The family of curves are the best fitting power law curves, as given in Table 8.2, coloured in the same fashion as the data points.

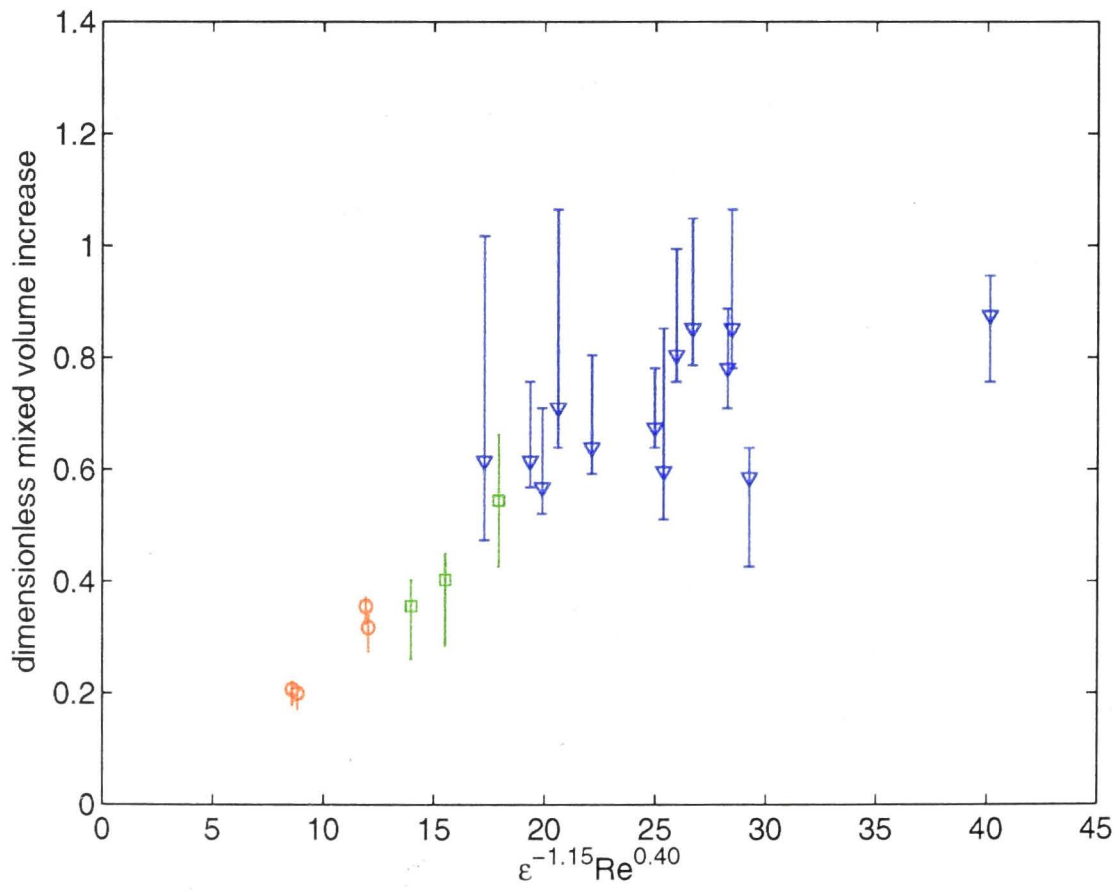

Figure 8.10: The dimensionless increase in the mass of mixed fluid due to the forcing event, versus $\epsilon^{-1.15}Re^{0.40}$. The red data (circles) represent experiments with increased viscosity ($\nu = 9 \times 10^{-6}\mathrm{m}^2/\mathrm{s}$), green (squares) represents reduced diffusivity data ($\kappa = 0.61 \times 10^{-9}\mathrm{m}^2/\mathrm{s}$), while the blue (triangles) data points have standard viscosity and diffusivity ($\nu = 1 \times 10^{-6}\mathrm{m}^2/\mathrm{s}$ and $\kappa = 1.5 \times 10^{-9}\mathrm{m}^2/\mathrm{s}$).

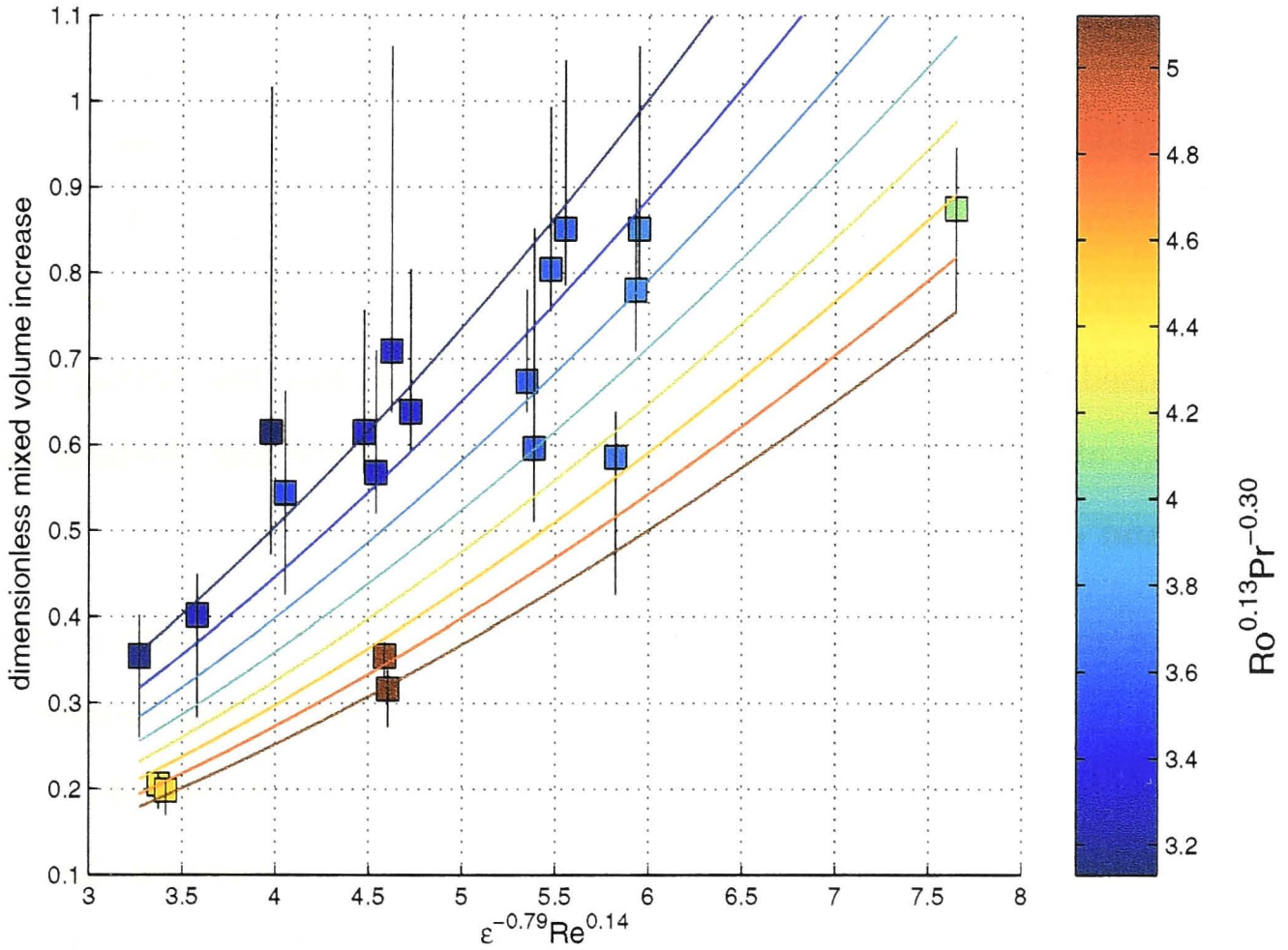

Figure 8.11: The dimensionless increase in the mass of mixed fluid due to the forcing event, versus $\epsilon^{-0.79}Re^{0.14}$. Each data point is coloured according to the value of $Ro^{-0.13}Pr^{-0.30}$ as determined by the colour bar. The family of lines are the best fitting power law curves, as given in Table 8.2, coloured in the same fashion according to the value of $Ro^{-0.13}Pr^{-0.30}$.

8.2.4 The potential energy of the system and "mixing efficiency"

Conventionally, the potential energy of the system would be regarded as

$$PE = \int_{-H}^{0} \int_{0}^{R} 2\pi\rho g z^* r \, \mathrm{d}r \, \mathrm{d}z, \tag{8.10}$$

where the $z^* = z - \Omega^2 r^2/(2g)$ term is to adjust for curvature of the equipotential surfaces due to the centrifugal force.

However, it was difficult to obtain meaningful values of the potential energy using this formula, because of optical distortions and other effects that caused the apparent position of the front to move from one measurement to the next. Equation (8.10) provided more information about the position of the interface than it did about whether mixing had raised the potential energy of the fluid. It was like trying to find the potential energy of a weakly stratified tank whose free surface was sloshing backwards and forwards and dwarfing any effect of the stratification.

I describe a method below to remove the influence of the position of the fluid interface on the estimate of the potential energy of the system. This method shall first be demonstrated by considering an idealised one dimensional density field consisting of two layers of differing density separated by a mixed region of thickness Δh, where the density increases linearly from the lower to higher density. The density field is given by the formula

$$\rho = \begin{cases} 0 & h + \frac{\Delta h}{2} < z \leq H \\ -\frac{\Delta\rho}{\Delta h}(z - (h + \frac{\Delta h}{2})) & h - \frac{\Delta h}{2} < z \leq h + \frac{\Delta h}{2} \\ \Delta\rho & 0 \leq z \leq h - \frac{\Delta h}{2} \end{cases} \tag{8.11}$$

and is sketched in figure 8.12.

A vertical integration of the density field gives the mass per unit cross-sectional area to be $M_c = h\Delta\rho$, which is assumed to remain constant under the presence of mixing. The mass of the mixed region, between $h - \Delta h/2$ and $h + \Delta h/2$, is given by $M_{c,m} = \Delta\rho\Delta h/2$. The potential energy per unit cross-sectional area of this system is

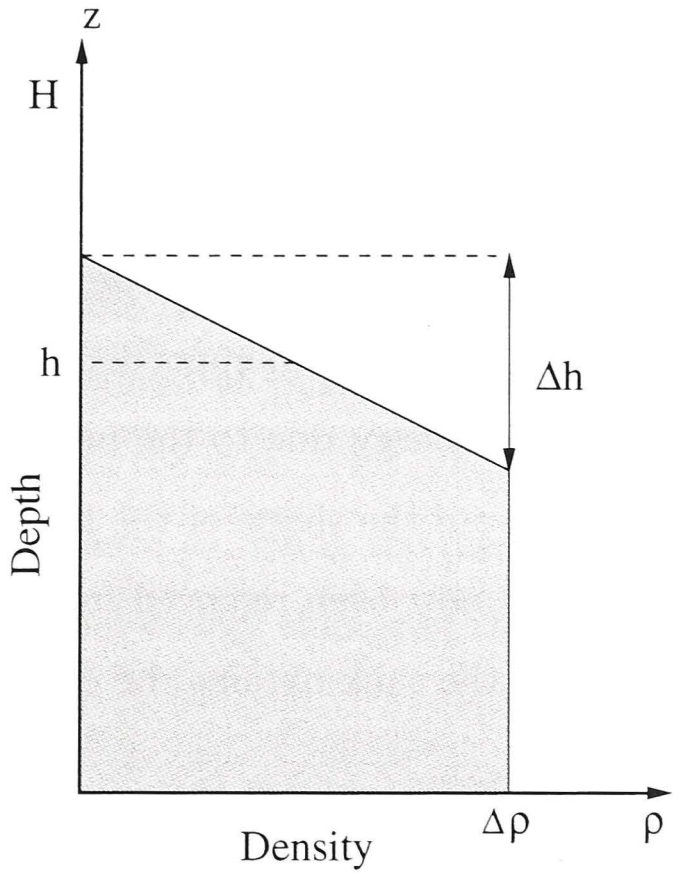

Figure 8.12: A simple density profile.

given by

$$PE_c = \int_0^H \rho g z \, \mathrm{dz} = g\Delta\rho \left(\frac{h^2}{2} + \frac{\Delta h^2}{24} \right) = \frac{g}{2\Delta\rho} \left(M_c^2 + \frac{1}{3} M_{c,m}^2 \right), \tag{8.12}$$

where the c subscripts refer to the fact that these quantities are for the fluid column of unit cross-sectional area. The first term on the right hand side of (8.12) is the potential energy of the fluid column when there is no mixing. The second term represents the increase in the potential energy due to the layer of mixed fluid. The coefficient of this second term is highly dependent on both the density field of the mixed layer (for example, for a density field that has the shape of an error function, the coefficient is 50% larger), and also on how one defines the mixed layer. Thus it is unrealistic to try to derive the gain in potential energy due to the presence of the mixed layer solely from the mass of the mixed layer. However, the coefficient of the first term is not dependent on the density distribution, and thus it is possible to subtract this term from the potential energy of the fluid column to get the contribution of mixing to the potential energy field

$$PE_{m,c} = \int_0^H \rho g z \, \mathrm{d}z - \frac{g M_c^2}{2\Delta\rho}. \tag{8.13}$$

Notice that the height of the zero potential energy contour has been chosen to be at the base of the fluid column at $z = 0$. This choice is to be consistent with my assertion that the potential energy of the unmixed system is given by the second term in (8.13). It turns out that the above equation is true whatever height is chosen for the zero potential energy contour, as shown in appendix B. Thus, it is now possible to calculate the increase in potential energy due to the presence of mixed fluid without it being swamped by the signal from the shape of the interface (ie. the height of the zero potential energy contour has now been removed from the equation). Integrating (8.13) over the horizontal area of the tank obtains the desired formula

$$PE_m = 2\pi g \int_0^R \left(\int_0^H \rho g z \, \mathrm{d}z - \frac{g M_c^2}{2\Delta\rho} \right) r \, \mathrm{d}r. \tag{8.14}$$

In the previous two sections, there was a logical choice for the method of non-dimensionalising both the mass and the volume of the mixed fluid, using the cross frontal Ekman layer mass and volume fluxes, respectively. The situation is more complicated when normalising the potential energy change. Many experiments that measure the increase in the potential energy of a system define a mixing efficiency, which is the potential energy increase nondimensionalised by the energy input to the system. In this experiment, the energy input into the tank during the forcing event is the work done by the lid in exerting a stress on the surface of the fluid. The problem here is that the lid is exerting a stress on the fluid well away from the frontal region, which presumably is doing little to promote mixing between the fluids. For example, if the radius of the lid (and tank) was doubled and the radius of the front left unchanged, the work done by the lid would increase by a factor of 16 (the mean stress would quadruple, as would the area over which it acts), while presumably there would be little effect on the rate of production of mixed fluid. Linden (1979) alludes to a similar problem when considering the case of mixing produced by dropping a grid through a density interface. The potential energy increase in that case was nondimensionalised by the potential energy lost by the grid as it falls. However, it is unlikely that dropping the lid from a height of 100m would produce any more mixing than dropping it from a height of 50m, as most of the potential energy lost would have been dissipated in the

fluid well before or after it passed through the density interface. Hence the grid was dropped from the same height for each experiment so that the energy dissipated away from the interface was at least a constant.

For the present experiments the potential energy change has been normalised by the energy that would be required to push the fluid in the Ekman layer all the way across the front to the center of the tank. This is equivalent to the potential energy lost by that fluid as it falls a distance h_0, being the depth of the upper layer at the centre of the tank. Thus the potential energy change of the system is nondimensionalised by the amount

$$W_{\text{lid}} = Q_{\text{Ek}} \Delta \rho g h_0 t_f, \tag{8.15}$$

where Q_{Ek} is the Ekman layer volume flux defined in equation (7.26). In appendix C it is shown that the resultant dimensionless potential energy increase, or mixing efficiency, has a maximum value of 0.5, as was the case with Linden and Redondo (1991). In order to achieve this maximum efficiency we require not only perfect mixing, but it must also happen where the upper layer has a depth h_0. This is only possible at the centre of the tank. A more realistic upper bound for the mixing efficiency is found if we assume perfect mixing between the Ekman layer anomalous mass flux, and the entire upper layer. This leads to a maximum value of 1/6.

Measurements of the potential energy of the system were made at 5 minute intervals throughout the duration of each experiment. The increase in the potential energy due to the lid forcing event were then determined and non-dimensionalised using the method described above. The results are shown in Table 8.1, and the exponents of the best fitting power law curves in terms of both dimensional variables and dimensionless parameters are given in Table 8.2. Qualitatively, the results are similar to the mixed water mass and volume measurements. Decreasing the viscosity or density difference increased the potential energy jump due to the forcing event. Increasing the diffusivity or lid velocity also increased it. In terms of dimensionless parameters, the potential energy increase was boosted by decreasing the convective Rossby and Prandtl numbers, while the opposite occurred through increasing the Reynolds and forcing Rossby number. It was again assumed that the convective Rossby and Reynolds numbers were

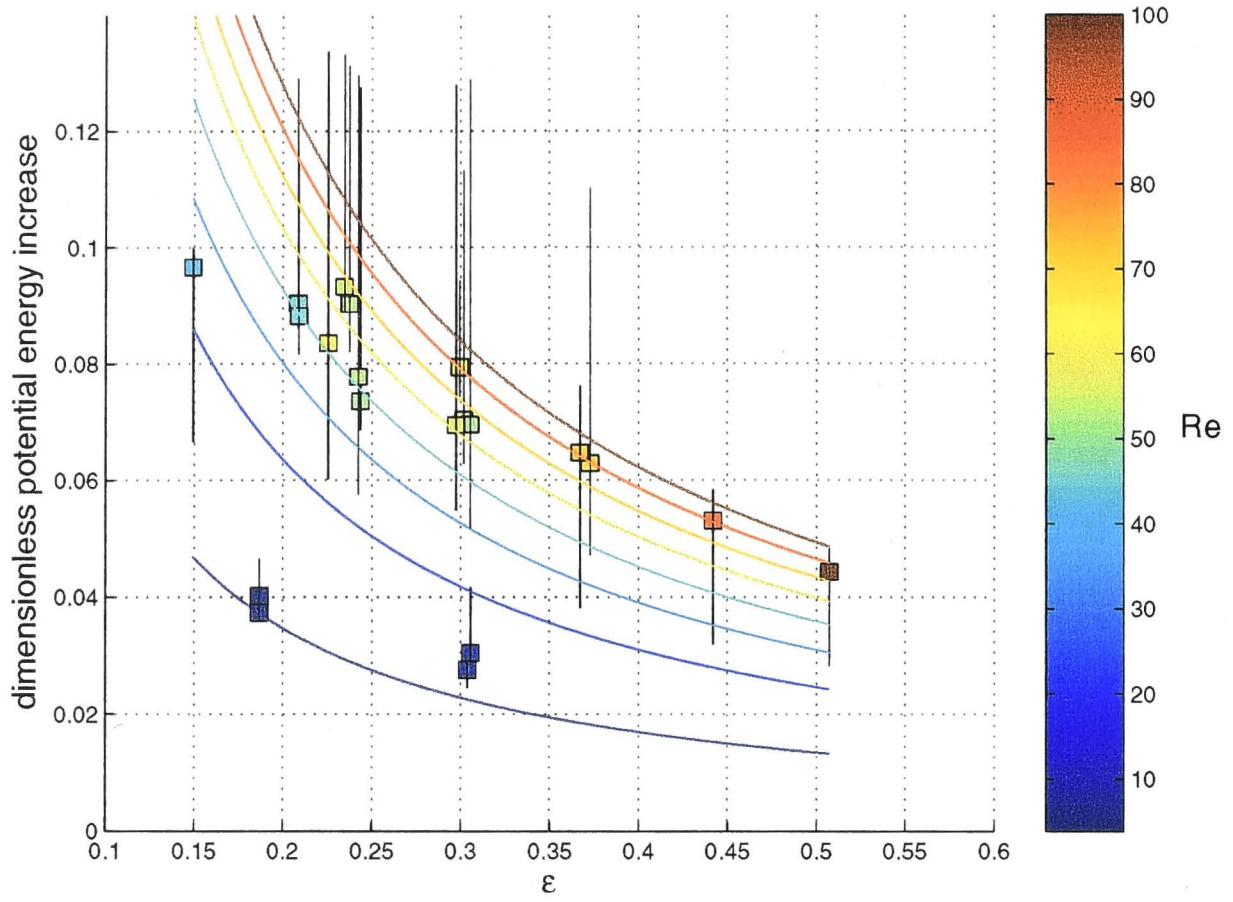

Figure 8.13: The dimensionless increase in the potential energy due to the forcing event, versus the convective Rossby number. Each data point is coloured according to the Reynolds number, as determined by the colour bar. The family of curves are the best fitting power law curves, as given in Table 8.2, coloured in the same fashion as the data points.

the dominant parameters in producing figure 8.13 and figure 8.14. However, the exponents in Table 8.2 suggest that both the forcing Rossby and Prandtl numbers are more important than the Reynolds number, and figure 8.15 is included to show the influence of all four prarameters.

The magnitude of the dimensionless potential energy increase is also worth noting. These values may be thought of as mixing efficiencies, and values in the range of 0.028-0.10 were obtained. This is significantly less than the $1/6 \approx 0.17$ acheived though uniform perfect mixing over the entire upper layer, which again highlights the possible problems in using the convective adjustment scheme. In relative terms, the normalised potential energy increases represent 17-60% of the theoretical maximum possible mixing efficiency. To compare, Linden and Redondo (1991) achieved mixing efficiencies of approximately 0.3, which was 60% of the theoretical maximum (0.5). It is difficult to make a direct comparison between their experiments and the present ones. The absence of rotation in their experiments results in infinite values of the convective Rossby, Burger and forcing Rossby numbers. It is clear that their experiments are in

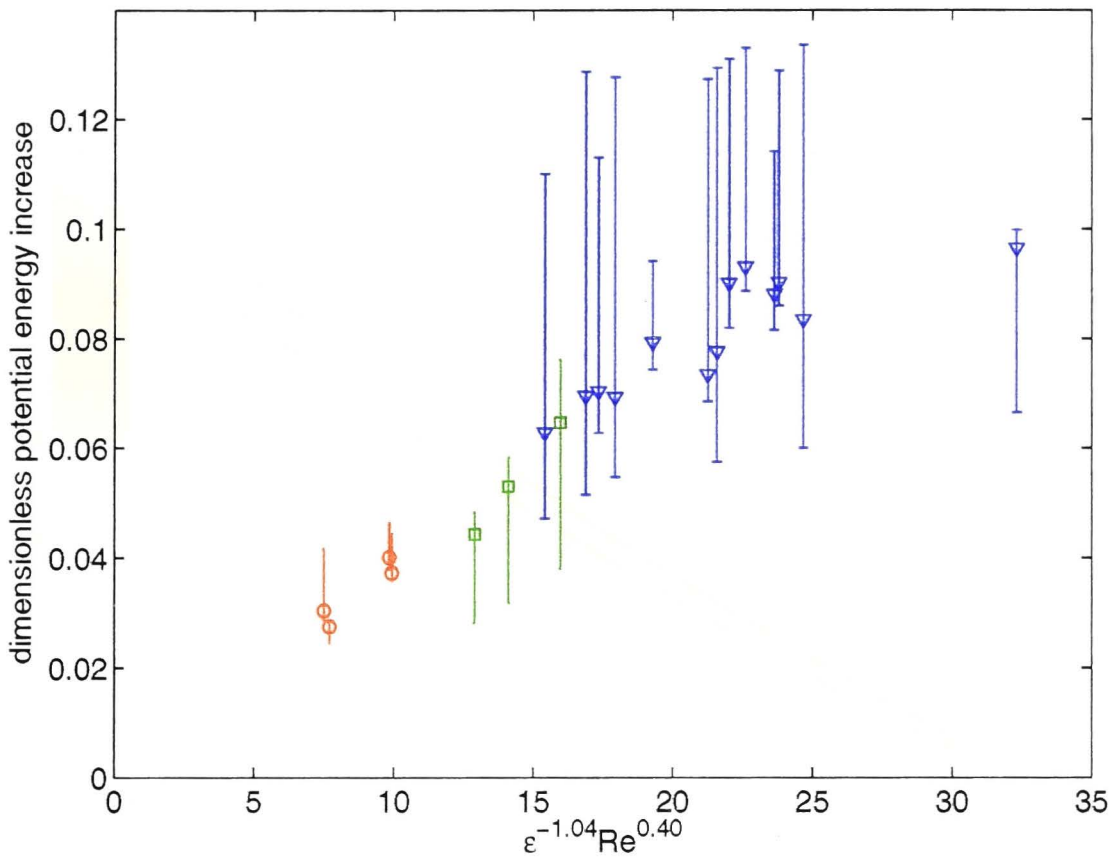

Figure 8.14: The dimensionless increase in the potential energy due to the forcing event, versus $\epsilon^{-1.04}Re^{0.40}$. The red data (circles) represent experiments with increased viscosity ($\nu = 9 \times 10^{-6}\mathrm{m}^2/\mathrm{s}$), green (squares) represents reduced diffusivity data ($\kappa = 0.61 \times 10^{-9}\mathrm{m}^2/\mathrm{s}$), while the blue (triangles) data points have standard viscosity and diffusivity ($\nu = 1 \times 10^{-6}\mathrm{m}^2/\mathrm{s}$ and $\kappa = 1.5 \times 10^{-9}\mathrm{m}^2/\mathrm{s}$).

a different regime to the present experiments.

It was mentioned earlier that there was not a clear logical choice for normalising the potential energy increases measured in these experiments. It was decided to use the potential energy that would be lost by by the anomalously dense water falling a distance h_0. An alternative method of nondimensionalising the potential energy increase would be to use the kinetic energy of the fluid in the Ekman layer as it crossed the front. This is given by

$$\mathrm{KE} = \pi\rho\omega^3 r_c^4 d/30. \tag{8.16}$$

If we had used this quantity to normalise the potential energy increases, the best fitting power laws to the resultant data would have had the form

$$\mathrm{PE} \sim \nu^{-0.51\pm.03}\Delta\rho^{0.74\pm.06}\omega^{-2.04\pm.11}\kappa^{0.40\pm.16} \tag{8.17}$$

The exponents in this formula bear little resemblence to those obtained for the mixed water mass and volume results. Additionally, the dimensionless potential energy in-

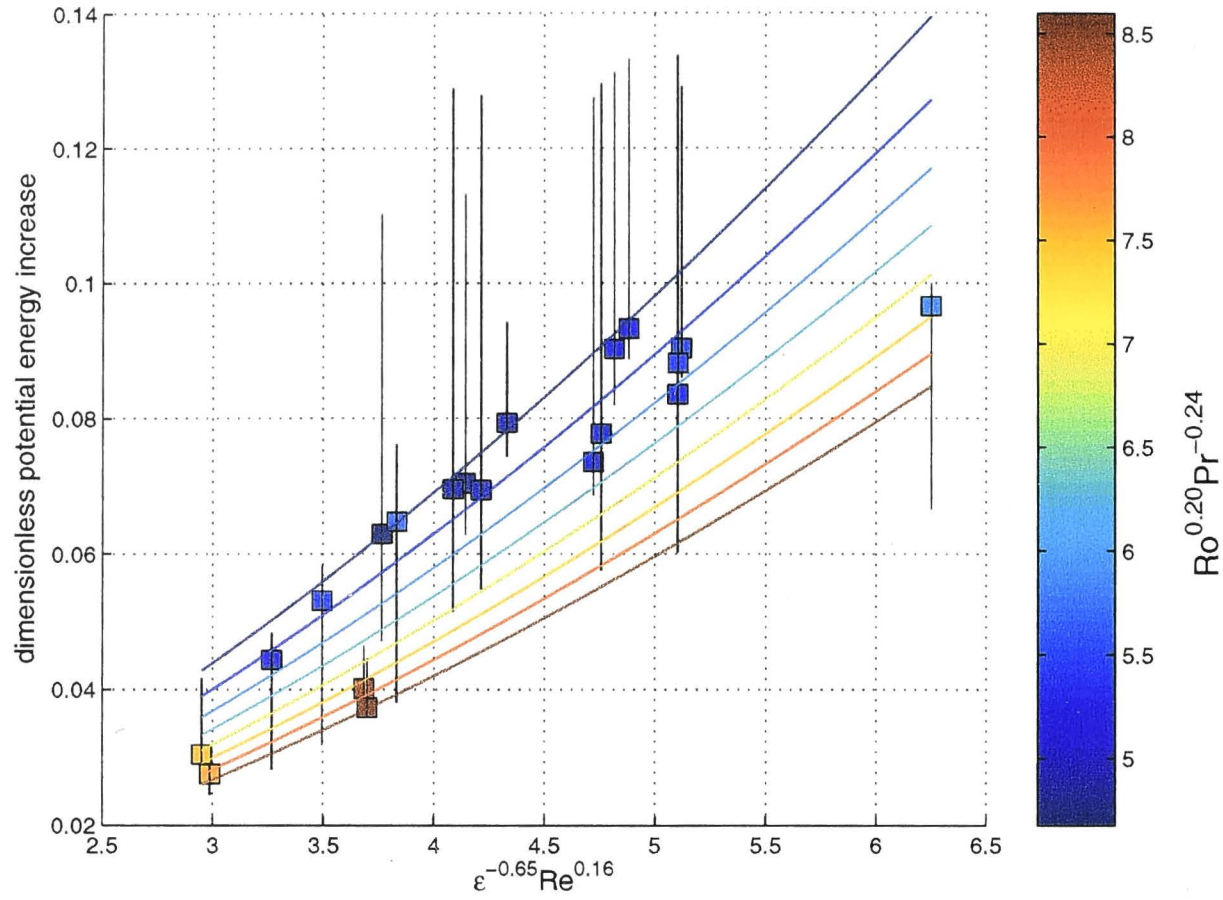

Figure 8.15: The dimensionless increase in potential energy due to the forcing event, versus $\epsilon^{-0.65}Re^{0.16}$. Each data point is coloured according to the value of $Ro^{-0.20}Pr^{-0.24}$ as determined by the colour bar. The family of lines are the best fitting power law curves, as given in Table 8.2, coloured in the same fashion according to the value of $Ro^{-0.20}Pr^{-0.24}$.

crease using this method of nondimensionalisation is predicted to *decrease strongly* when the lid rotation rate is *increased.* It is clear that the original method of normalising the potential increase using (8.15) is preferable to using the kinetic energy of the Ekman transport across the front.

Chapter 9

Oceanic implications and conclusions

9.1 Comparison with ocean fronts and convection regions

The design of the experiments presented in this thesis was possibly the simplest method to simulate wind-driven convection at density fronts. This highly idealised two layer model, in which the front was maintained through centrifugal force, bears little resemblence to real geophysical fronts. In this section we discuss aspects that must be considered when trying to apply our results to real geophysical situations.

9.1.1 The ocean Ekman layer

The Ekman layer that formed in the experiments presented in this thesis was laminar, was mostly unaffected by the two layer stratification present in the tank, and had an upper boundary that was non-slip and always moving in a direction parallel to the front. These conditions all change in real geophysical situations.

Turbulence in the ocean causes momentum to be transferred from the sea surface to the interior by turbulent eddies, rather than by molecular viscosity. Turbulence transports the momentum much more effectively, and the resulting Ekman layer is two to three orders of magnitude larger than the $O(0.1)$ m predicted by (7.24) for the ocean.

Stratification hinders vertical turbulent motion, and thus to a small extent counters the thickening of the Ekman layer due to the turbulent transport of momentum. In particular, if the thermocline happens to be relatively shallow, the large vertical density gradients there will confine most of the Ekman layer to the fluid above the thermocline.

Despite the two opposing effects of turbulence and stratification, the velocity structure and thickness of the ocean Ekman layer remain significantly altered from that given by equations (7.21)-(7.23). However, one important result that remains valid from the homogeneous, laminar Ekman layer equations is the solution for the net horizontal transport of water in the Ekman layer,

$$U = \frac{\tau}{\rho_0 f}, \tag{9.1}$$

where τ is the wind stress exerted on the surface of the ocean, $f = 2\Omega \sin\phi$, is the Coriolis parameter and ϕ is the latitude of the front. In the deep ocean, the direction of the net transport is perpendicular and to the right (left) of the wind in the Northern (Southern) hemisphere.

The Ekman layer in the ocean also retains a general 'spiral-like' pattern to the velocity structure, so that each water column contains fluid moving in a variety of directions relative to the wind. This means that winds directed at a large range of angles relative to the front can lead to water at some depth being advected across the front. To illustrate this point, appendix D shows the advection of isopycnals by the velocity field satisfying the homogeneous, laminar Ekman layer equations, produced by a wind at a variety of angles to the front. It also shows the time scale it would take for the density instabilities to occur, as a function of wind angle. In this highly idealised model, the maximal cross-frontal mass flux occurs when the wind is blowing parallel to the front, though convection occurs most rapidly when the wind direction is normal to the front, from the dense to light side. As was found in section 7.1.3, the timescale for an unstable density profile to be produced was much less than the Ekman layer formation time.

9.1.2 Properties of the SAMW formation region

It has been postulated that Ekman transport across the Subantarctic front (SAF) leads to the formation of Subantarctic Mode Water (SAMW) (England et al., 1993; Hirst and Godfrey, 1993; Rintoul and England, 2002). The SAF is the strongest front associated with the Antarctic circumpolar current (ACC) (Sokolov and Rintoul, 2002).

The strong temperature and salinity gradients associated with this front are mostly density compensating, though a small density difference of approximately $0.1\,\mathrm{kg/m^3}$ is often present.

The SAMW formation region is associated with a large region of near uniform density (pycnostad) to the north of the SAF. A comparison of the properties of the pycnostad associated with the SAMW formation region[1] and those of our experiments is given in Table 9.1. The dimensionless numbers relevant to our mixing experiments are also shown in this table.

Property/parameter		Laboratory	SAMW pycnostad
Reduced gravity	g'	$0.017 - 0.170\,\mathrm{m/s^2}$	$0.001\,\mathrm{m/s^2}$
Kinematic viscosity	ν	$(1.0 - 9.0) \times 10^{-6}\,\mathrm{m^2/s}$	$0.01\,\mathrm{m^2/s}$
Diffusivity	κ	$(0.61 - 1.5) \times 10^{-9}\,\mathrm{m^2/s}$	$0.01\,\mathrm{m^2/s}$
Coriolis parameter	f	$4.4\,\mathrm{s^{-1}}$	$10^{-4}\,\mathrm{s^{-1}}$
Frontal radius	r_c	$0.37\,\mathrm{m}$	5×10^5 m
Upper layer thickness	h_0	$33.2\,\mathrm{mm}$	500 m
Convective Rossby number	ϵ	$0.15 - 0.51$	14
Reynolds number	Re	$3.9 - 100$	1400
Rossby number	Ro	$0.027 - 0.091$	4×10^{-3}
Prandtl number	Pr	$670 - 6000$	1
Burger number	Bu	$(2 - 16) \times 10^{-4}$	2×10^{-4}

Table 9.1: Comparision of properties for the laboratory experiments and the Subantarctic Mode Water formation region. See the text in section 9.1.2 for more details.

The upper layer of the ocean is turbulent, regardless of whether or not convection is occuring. There is a turbulence at all length scales from mixed layer depth down to millimetre, and therefore at scales much less than that associated with convection. For this reason, when calculating the Reynolds and Prandtl numbers of ocean convection, we need to use turbulent values for the kinematic viscosity and diffusivity, and the corresponding Prandtl number is one.

The interpretation of the frontal radius is not immediately clear when considering ocean fronts. However, in the definition of the Burger number, which for the ocean has

[1]The SAMW formation region values for r_c, h_0 and g' were estimated from the data obtained from WOCE, section SR3 (July 1995) shown in figure 2 of Rintoul and England (2002).

the form

$$Bu = \frac{g' h_0}{f^2 r_c^2}, \tag{9.2}$$

r_c was interpreted as the width of the pycnostad located on the less dense side of the front, through which the dense water convects (see section 8.2.1). Similarly, h_0 is interpreted to be the thickness of the pycnostad. For the SAMW formation region, we estimated $r_c \approx 500$ km and $h_0 \approx 500$m. These values lead to a Burger number of order 2×10^{-4}. In the laboratory experiments, $Bu < 0.002$. Thus in both situations, the Rossby radius is much smaller than the width of the body of water the mixed fluid is spreading into, and it is expected that this implies the Burger number is not important to the production rate of mixed fluid.

The Rossby number must also be revised slightly, so that it may be applied to the ocean. For the oceans we use

$$Ro = \frac{2U}{r_c f}, \tag{9.3}$$

where U is a typical cross frontal water velocity. We have used the value $U = 0.1$ m/s in calculating the oceanic Rossby number. Like the experimental values, this value is much less than one, and we expect that this makes the Rossby number unimportant to the production rate of mixed fluid.

For the ocean the convective Rossby number is given by

$$\epsilon = \frac{1}{f}\sqrt{\frac{g'}{h_0}}. \tag{9.4}$$

For the SAMW formation region, the computed value for this number is of order 14. It was predicted in section 8.1 that when the convective Rossby number is less than a critical value, $\epsilon < \epsilon_c$, then rotation would influence convection. The theory predicted $\epsilon_c \sim (2\pi^2 \alpha_0)^{-1/2} \approx 1$. Although this was only a scale estimate of the critical convective Rossby number, when $\epsilon = 14$, it is probably safe to conclude that rotation is not going to affect significantly the flow. To emphasise this, equation (7.40), with $\alpha = 0.05$, predicts that it will take approximately 75 minutes for a growing instability to engulf the 500 m thick pycnostad associated with the SAMW formation region. This compares with an inertial period of $2\pi/f \approx 16$ hours for a latitude of 50^o.

Given the large value of ϵ calculated for the SAMW pycnostad, it might seem logical to use the non-rotating value $\alpha = \alpha_0 = 0.05$ when calculating the corresponding Reynolds number. However, to be consistent with the Reynolds numbers calculated for the laboratory experiments, we shall continue to use the value $\alpha = 0.003$. In possible future studies involving a wider range of values for the convective Rossby number, or in particular for $\epsilon > 1$, it might be more appropriate to use the value α_0 (or leave it out entirely) in the Reynolds number definition.

It is clear from Table 9.1 that the oceanic values of most of the dimensionless numbers governing the production of mixed fluid are considerably different from the laboratory experimental counterparts. Even worse, we know that the two processes operate in different regimes, as the convection that occurs in the SAMW formation region is little affected by rotation, whereas our experiments were heavily influenced by the tank rotation. Thus, it is not possible to make predictions relating to the ocean with any great degree of confidence by interpolating from the experimental results. Nevertheless, we shall try, by making a series of assumptions. We shall assume that the Prandtl, Rossby and Burger numbers are not important in determining the increase in mass and volume of mixed water, or the mixing efficiency. We shall also assume that the power law fits to the experimental data continue to hold to the much larger Reynolds number appropriate to the ocean, and also for the convective Rossby number up to $\epsilon = 1$. For values of $\epsilon > 1$, we assume the results are independent of the convective Rossby number, as under these circumstances rotation is no longer important in the convective process. In the absence of experimental data for $\epsilon > 1$ I believe the above assumption is most reasonable. Using the values $Re = 1400$ and $\epsilon = 1$, we obtain $\epsilon^{-1.29} Re^{0.56} \approx 58$, $\epsilon^{-1.15} Re^{0.40} \approx 18$ and $\epsilon^{-1.04} Re^{0.40} \approx 18$. From figures 8.8, 8.10 and 8.14 we see that these values all fall within the experimental limits. Moreover, the dimensionless mass (MixMass2), volume and potential energy increases are predicted to be approximately 0.3, 0.6 and 0.08 respectively. However, these predictions are all sensitive to the value of ϵ. The assumption that mixing at $\epsilon > 1$ is the same as the mixing predicted by using $\epsilon = 1$ in relationships established only for $\epsilon < 1$ leaves a great deal of uncertainty in the predicted values of the dimensionless mass, volume and potential energy increases. Nevertheless, the extrapolation does indicate that ocean

mixing may be far from perfect mixing, with the predicted volume of mixed water production only 60% of the Ekman layer transport.

9.2 Discussion and Future work

It is clear from section 9.1.2 that there is a need to conduct experiments with larger convective Rossby numbers if we want to apply the results to wind-driven convection in the ocean. However, it is not feasble to achieve oceanic values of $\epsilon \sim 14$ using the experimental techniques used in the present experiments. To demonstrate this, we recall that setting up this experiment required a compromise between maximising the volume of the upper layer to minimise the effects of diffusion and mixing during spin-up, and having the interface outcrop on the lid. The former may be better expressed by considering the initial thickness of the upper layer before spin-up, h_i. This is related to the upper layer volume through the equation $V = \pi R^2 h_i$, where R is the tank radius. The second requirement may be expressed through the dimensionless frontal radius, $\sigma = r_c/R$. For the interface to outcrop on the lid to form a front, we require $\sigma \leq 1$. The fronts in the present experiments were maintained through centrifugal force. This means that the form of the density interface is given by equation (7.9), and the volume of the upper layer by $V = \pi h_0 r_c^2/2$. With these definitions and relationships, the convective Rossby number may now be rewritten in terms of h_i and σ:

$$\epsilon = \frac{\sigma^3 R A^{1/2}}{4 h_i}. \tag{9.5}$$

Thus, the convective Rossby number may be increased by increasing the dimensionless frontal radius, the tank radius or the Atwood number, or by reducing the initial upper layer thickness (pre spin-up). Experimental difficulties are encountered by attempting any of these changes to a significant degree.

For our experiments the dimensionless frontal radius was $\sigma = 0.75$. The outer wall of the tank was not visible to the camera without using an oblique viewing angle. Increasing the frontal radius would come at a cost of having to further increase the viewing angle of the camera from perpendicular to the tank sidewall. This would result

in an increased amount of optical distortion, complicating the image analysis. Even without this problem, increasing the dimensionless frontal radius to $\sigma = 1$ would only increase the convective Rossby number by a factor of 2.4, significantly short of the order of magnitude increase required to increase the present experimental convective Rossby numbers to $\epsilon \gg 1$.

Similarly, there is little scope for significantly increasing the convective Rossby number by increasing the Atwood number. The largest density difference used in these experiments was $\Delta\rho \approx 17.6\text{kg/m}^3$. For this relatively large density difference, the refractive index of the two layers needed to be matched. The bottom layer used a 7.67% (by weight) Epsom salt solution. Practically, increasing the density difference by a factor of nine would be difficult, and this would increase ϵ only by a factor of 3.

The initial thickness of the upper layer before spin-up, h_i, was 9.3 mm. Halving this thickness would result in salt having diffused from the lower layer into most of the upper layer by the time the experiment was spun up to solid body rotation. Unless a stratifying agent with a much smaller diffusivity than sodium chloride is used, there is little room to reduce this upper layer thickness and still have two distinct layers at the commencement of the forcing period.

The problems relating to increasing the tank radius by an order of magnitude or more are obvious. Thus, it appears that simulating wind driven convection in the ocean using the current experimental set-up is very difficult. One alternative is to use a thermal wind balance to help the density interface outcrop on the lid. A larger volume of upper layer fluid could be used, so that when the tank and fluid are at solid body rotation the interface did not outcrop on the lid. However, when the lid was turned on anticyclonically, after a time interval equal to the spin-down time of the upper layer $h_0(\nu\Omega)^{-1/2}$, the upper layer would be approximately rotating at the reduced lid speed. The change in velocity across the density interface would be related to a steepening of the interface though the thermal wind balance. The formula for the density interface is given by

$$h = h_0 + \frac{\Omega^2 r^2}{2g}\left(1 + \frac{Ro}{A}\right) \tag{9.6}$$

As we saw in section 7.1.2, the second term in the brackets on the right hand side

of equation (9.6) was much greater than one for our experiments, indicating that the thermal wind balance can have a greater influence on the steepness of the parabolic density interface than does the centrifugal force.

If the upper layer volume was set to an appropriate value, then the new position of the density interface would outcrop at the boundary between the lid and sidewall (ie. $\sigma = 1$). In this position, none of the lower layer would be exposed to the rotating lid. The Ekman layer underneath the lid shuts down once the upper layer slows down to the lid speed, as there would no longer be a speed differential between the two. Thus, the base state is no longer one in which the tank and fluid are in solid body rotation, instead the water is in a geostrophic balance.

The forcing event could be achieved by reducing the lid speed further (greater anticyclonic forcing). During this forcing event, dense fluid would be entrained in the upper Ekman layer, and subsequently transported across the front.

The convective Rossby number for this technique is given by

$$\epsilon = \frac{\sigma^3 R A^{1/2}}{4 h_i} \left(1 + \frac{Ro}{A} \right). \tag{9.7}$$

Convective Rossby numbers of order 14 are now feasible with the current experimental set-up, so an improved simulation of wind-driven convection in the ocean appears possible.

This experiment will be complicated by baroclinic instabilities. The steepened interface between the two layers involves an increase in the potential energy of the system. This potential energy can feed the growth of eddies along the interface. This is exactly what happens along ocean fronts, so in this sense the proposed experiments may be more realistic than those presented in this thesis. However, the presence of these eddies, in addition to the more complex geostrophic base state, will greatly complicate the measurement of mixing in what is already a difficult experiment.

9.3 Summary

An experiment was designed in an attempt to study the effects of wind driven convection at ocean density fronts. A cylindrical tank was filled with a two layer density stratification, and spun at a sufficiently high speed so that the density interface outcropped on the lid of the tank. Once solid body was achieved, the lid was turned on for a limited period of time in an anticyclonic fashion, which created a radially inward directed Ekman current, moving dense water across the front and over the top of light water. After some time, the unstable density profile generated convection, which created mixing between the two layers of the experiment.

Theoretical arguments presented in chapter 7 indicate that the standard Ekman layer flow solutions should apply up until the onset of convection despite the presence of the density front. The time interval between turning on the lid and convection first engulfing the upper layer was predicted to be given by (7.40). This was in good agreement with the measured experimental timescales presented in chapter 8. It was found the growth rate of the growing instabilities was significantly slower than what has previously been measured in standard, non-rotating Rayleigh-Taylor experiments. This was thought to be caused by the strong importance of rotation in our experiments. The importance of rotation was measured using the convective Rossby number, ϵ, which is inversely proportional to the convection timescale normalised by the inertial period (8.3). All of our experiments had $\epsilon < 0.52 < 1$, indicating that rotation was important to the convection.

Measurements of the increase in mass and volume of mixed fluid due to the forcing event were presented in section 8.2. The mass of mixed fluid was found to increase by between 10% and 53% of the Ekman layer anomalous mass transport across the front using the MixMass1 definition, and by between 6% and 36% using the MixMass2 definition. The volume of mixed fluid increased by between 20% and 87% of the Ekman layer volume transport across the front. It was found that the convective Rossby number had the greatest influence on the dimensionless amount of mixed fluid produced. An increase in the convective Rossby number reduced the production of mixed fluid. This was thought to be due to the increased levels of relative vorticity

present in the convecting plumes, which more efficiently entrained surrounding fluid. Increasing the Reynolds number also boosted the production of mixed fluid, as did increasing the forcing Rossby number or decreasing the Prandtl number.

Nondimensional values of the potential energy increase due to the forcing event were found to range between 0.028-0.10. This represented mixing efficiencies of between 18% and 60% of the theoretical maximum. Again the convective Rossby number was found to be the most influential, with an increasing convective Rossby number reducing the mixing efficiency.

Significant extrapolation was required to apply these results to wind-driven convection in the ocean. The predictions have a high level of uncertainty, primarily due to differing levels of importance of rotation. While the experimental values of the convective Rossby number ranged from 0.15 to 0.51, for the SAMW formation region $\epsilon \approx 14$. This indicates that rotation played a significant role in the laboratory convection, but is not important to the oceanic convection. It appears unlikely that the experimental technique used in the experiments presented in this thesis could achieve the oceanic convective Rossby number range. Proposed experiments that use a thermal wind balance to steepen the parabolic interface between the two-layer density stratification could achieve the relevant convective Rossby number, but would involve significant difficulties in accurately measuring the production of mixed water due to the forcing event.

Appendix A

PLIF calibration

Planar laser-induced fluorescence (PLIF) was used to visualise the experiments presented in chapter 6. This involved dying the upper layer of fluid with sodium fluorescein, illuminating the fluid with a vertical sheet of laser light, and viewing the illuminated fluid from an angle perpendicular to the laser sheet using a digital video camera. From the pictures taken, we were able to estimate the density field of the tank. This appendix describes the method used in this last step.

The relationship between the intensity of the image of the fluoresced light and the dye concentration is given by (Ferrier et al., 1993; Atsavapranee and Gharib, 1997)

$$S_{ij} = B_{ij} + G(IC) I_{ij} C_{ij}, \tag{A.1}$$

where S_{ij} is the image intensity recorded on the i'th vertical and j'th horizontal pixel, B_{ij} is the background intensity, $G(IC)$ is the gain, I_{ij} is the local laser light intesity and C_{ij} is the dye concentration. We have assumed the gain is the same for all pixels, though it may depend on the fluoresced light intensity.

The laser sheet propagates vertically downwards through the viewed field. As it is absorbed by the sodium fluorescien, it becomes less intense. This is expressed mathematically through the Bouguer-Lambert-Beer Law (Wagner, 1961), which states that the local laser light intensity decays exponentially with penetration distance. Thus

$$I_{ij} = I_{0j} \exp\left[-\sum_{i'=0}^{i-1} \left(\eta_w + \epsilon_0 C_{i'j} \right) \Delta y \right], \tag{A.2}$$

where η_w is the absorption coefficient of the water, ϵ_0 is the extinction coefficient of

the sodium fluorescien, and Δy is the vertical pixel resolution.

To perform the calibration, the value of the parameters B_{ij}, $G(IC)$, I_{0j}, η_w and ϵ_0 needed to be determined. This was done by observing the image intensity of a tank filled with a variety of constant dye concentrations $C_{ij} = C$. Equations (A.1) and (A.2) predict that the observed image should have an intensity field given by

$$S_{ij} = B_{ij} + G(IC)CI_{0j}e^{-[(\eta_w+\epsilon_0 C)\Delta y\ i]}. \tag{A.3}$$

The first process in the calibration was to determine the background intensity, B_{ij}. This was done by observing a tank filled with water containing no dye. For this case, $C = 0$ and (A.3) predicts $S_{ij} = B_{ij}$. The next step was to determine the value of the product of the gain and the initial laser intensity, $G(IC)I_{0,j}$. We called this product the gain function, and note that it depends on the horizontal pixel number j. Equation (A.3) indicates that a plot of $S_{0j} - B_{0j}$ versus C should reveal a line with slope equal to the gain function, if that gain function is constant. Figure A.1 is such a plot, with two lines representing two different values of j. One line was calculated using small values of j, for which the pixel lies near the left edge of the picture. The second used values of j placing the pixel near the centre.

The laser sheet has a Gaussian intensity profile, which caused the centre of the image to be illuminated more than the edges. Hence the slope of the line taken from the centre of the plot is steeper than the plot from the edge, as the value of $G(IC)I_{0,j}$ was larger in the centre. It is clear from figure A.1 that above a dye concentration of about 5×10^{-7} mol/L, the relationship between the pixel intensity and the dye concentration is no longer linear, suggesting that the gain is not constant, but rather depends on the light intensity. This is from a combination of the camera nearing saturation, and from increased amounts of reabsorption of fluoresced light occuring between the illuminated sheet of fluid and the camera. For this reason, we restricted the dye concentrations of our experiments to 5×10^{-7} mol/L, so that we could assume a constant gain factor G, rather than one that depends on light intensity $G(IC)$.

By plotting $S_{0j} - B_{0j}$ versus C for all values j, and finding the slope, we were able to determine the entire gain function GI_{0j}. In practice, pixel intensities were averaged

over a range, both horizontally and vertically, to determine the quantities $S_{0j} - B_{0j}$ so as to reduce the noise present in the gain functions.

The final step in the PLIF calibration was to determine the coefficients η_w and ϵ_0. This was achieved by noting that the natural logarithm of equation (A.3),

$$\log(S_{ij} - B_{ij}) = log(GCI_{0,j}) - (\eta_w + \epsilon_0 C)\Delta y\, i, \tag{A.4}$$

predicts that a plot of the left hand side versus vertical pixel number i should reveal a straight line with slope $-(\eta_w + \epsilon_0 C)\Delta y$. The y intercept of this line should be different for each horizontal pixel number j, though the slope should be the same. By averaging over all the horizontal pixels, and calculating the slope of the best fitting line, we are able to determine the quantity $-(\eta_w + \epsilon_0 C)\Delta y$. By repeating this process for a variety of dye concentrations, C, the individual coefficients η_w and ϵ_0 are able to be determined.

With all the required parameters now known, it was possible to determine the unknown and nonuniform dye concentrations found in our experiments by analysing the pixel intensities of pictures taken during the experiment. The process is as follows. Equation (A.1), now with a constant gain function, was used to determine the dye concentration of the fluid captured by the top row of pixels using the formula

$$C_{0j} = \frac{S_{0j} - B_{0j}}{GI_{0j}}. \tag{A.5}$$

Knowing C_{0j} allowed us to calculate the laser intensity for the next row, I_{1j}, using equation (A.2). This in turn allowed us to calculate C_{1j} using equation (A.1), and so on until the entire dye concentration of the fluid captured by the camera was known. The final step was to determine the density field from the dye concentration field using the formula

$$\rho_{ij} = \rho_2 - \Delta\rho \frac{C_{ij}}{C_I} \tag{A.6}$$

where C_I was the initial dye concentration of the upper layer.

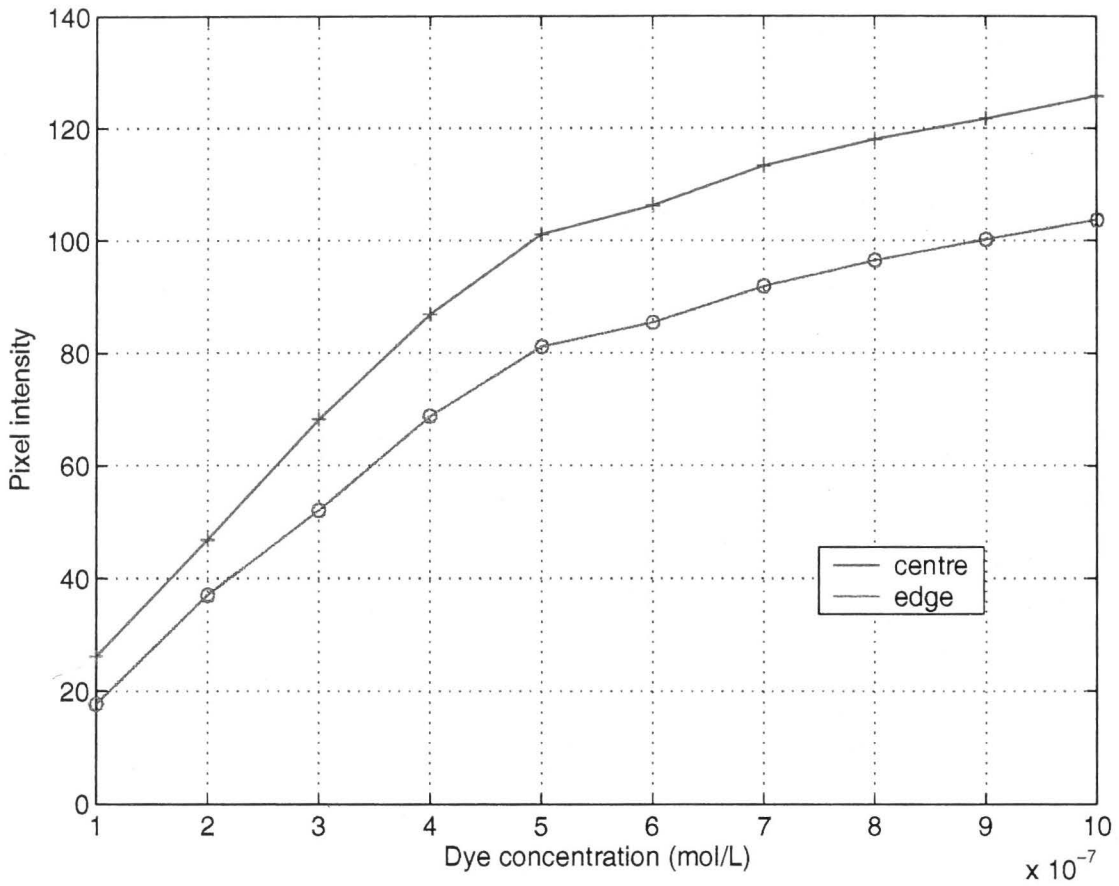

Figure A.1: A plot of pixel intensity versus dye concentration. The pixel intensities for the top curve were averaged over many pixels near the top and centre of the image where the laser intensity is virtually unchanged from its initial strength, before it has travelled through much dye. The data for the second curve were obtained from pixels near the top left hand side of the image.

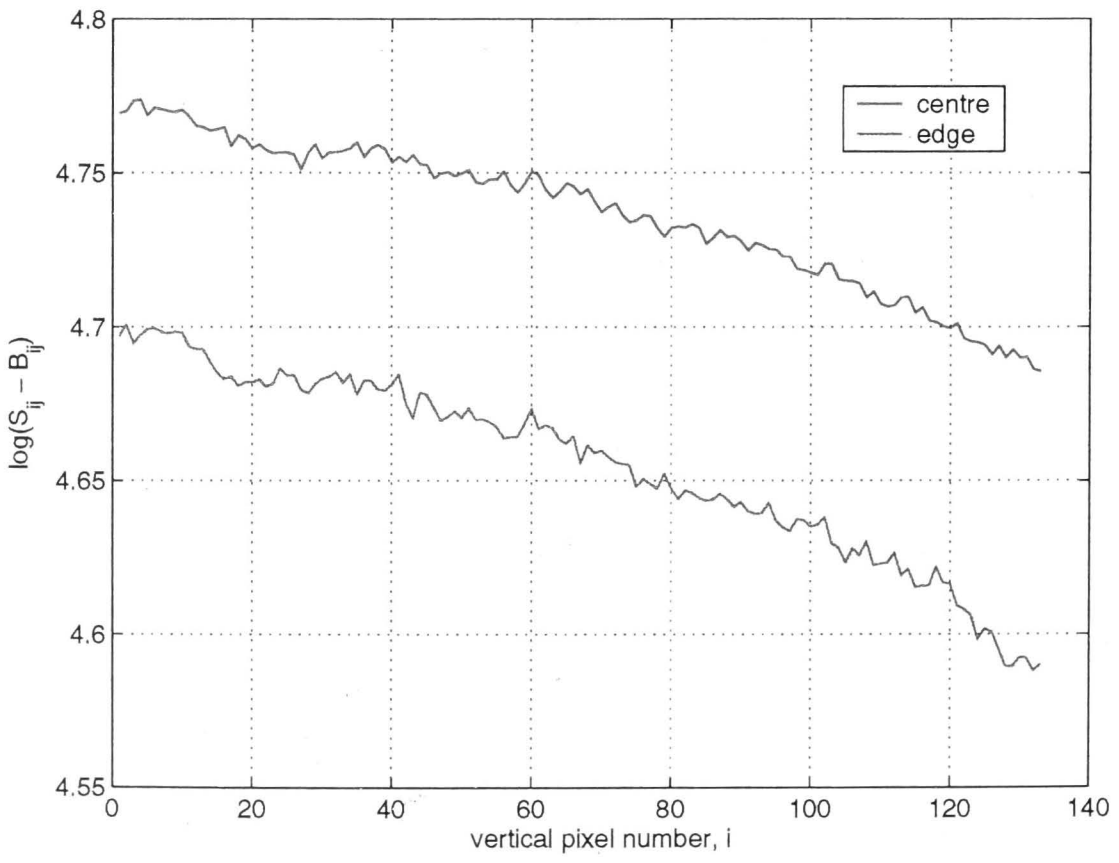

Figure A.2: A plot of the logarithm of the pixel intensity versus vertical pixel number. The top curve was taken from pixel intensities near the center of the image. The lower curve was taken using pixel intensities nearer the edge of the image.

Appendix B

Increase in potential energy due to mixing

In section 8.2.4 we introduced a method of calculating the increase in the potential energy of a fluid column due to the formation of mixed fluid. In the following theory we show that this increase is independent of the choice of the zero height potential surface.

Consider a fluid column with density $\rho(z)$ located between $z = 0$ and $z = H$. For potential energy calculations, let us define the height of the zero potential to be $z = z0$. The potential energy for this fluid column is thus given by

$$PE = \int_0^H \rho g(z - z_0)\,\mathrm{d}z = \int_0^H \rho g z\,\mathrm{d}z - g z_0 M_c \tag{B.1}$$

where M_c is the mass of that fluid column.

Now, let us consider the potential energy of the system if no mixing is present. In this situation, the density field is given by

$$\rho = \begin{cases} 0 & H_0 < z \leq H \\ \Delta\rho & 0 \leq z \leq H_0 \end{cases} \tag{B.2}$$

where $H_0 = M_c/\Delta\rho$ is the height of the interface between the two unmixed layers. The potential energy is given by

$$PE_0 = \int_0^{h_0} \Delta\rho g(z - z_0)\,\mathrm{d}z = g\Delta\rho(H_0^2/2 - z_0 H_0) = \frac{g M_c^2}{2\Delta\rho} - g z_0 M_c \tag{B.3}$$

The difference between the potential energy of the fluid column and the potential energy of the unmixed system is due to the mixing of the density field, and is given by

$$PE - PE_0 = \int_0^H \rho g z \, \mathrm{d}z - \frac{g M_c^2}{2\Delta\rho}, \tag{B.4}$$

and is thus independent of z_0, the height of the zero potential energy contour.

Appendix C

Mixing efficiency limits

Let us consider the mixing efficiency if perfect mixing occurs. We start off by considering an individual fluid column, pictured in figure C.1. It originally has density $\rho = 0$ and height h. During the forcing period, the Ekman layer brings an additional volume of dense fluid over the top, with $\rho = \Delta\rho$, that falls down through this fluid column. The added volume is a fraction γ of the original volume.

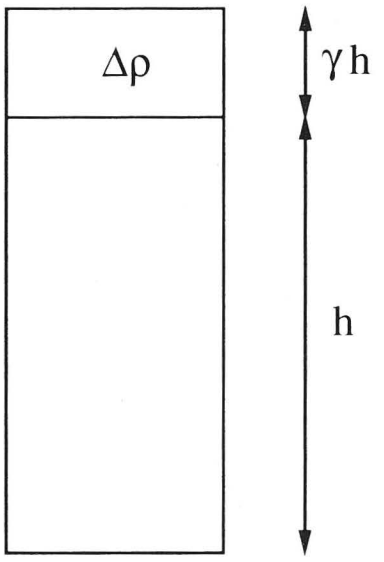

Figure C.1: A fluid column, where dense fluid has been introduced at the top.

If the introduced volume of fluid mixes perfectly with the fluid underneath it, then the uniform density of the perfectly mixed fluid will be given by

$$\rho = \frac{\gamma}{1+\gamma}\,\Delta\rho. \tag{C.1}$$

According to equation (8.13), the increase in potential energy due to the mixing is given by

$$PE_{m,c} = \int_0^h \rho g z \,\mathrm{d}z - \frac{g M_{c,m}^2}{2\Delta\rho} \tag{C.2}$$

where $M_{c,m} = \gamma \Delta \rho h$ is the mass of the fluid column. Substituting (C.1) into (C.2) we obtain

$$PE_{m,c} = \frac{\gamma(1+\gamma) g \Delta \rho h^2}{2} - \frac{\gamma^2 g \Delta \rho h^2}{2} = \frac{\gamma g \Delta \rho h^2}{2} = \frac{M_{c,m} g h}{2}. \tag{C.3}$$

The total potential energy increase is obtained by integrating (C.3) over all fluid columns. Mixing efficiency values are then obtained by dividing potential energy increase by $M_m g h_0$ (see equation 8.15), where M_m is the total anomalous mass, found by integrating $M_{c,m}$ over all fluid columns. It is clear that the maximum mixing efficiency obtainable is 0.5, which is what occurs if this perfect mixing were all to occur at a radius where $h = h_0$ (ie. the centre of the tank). A more restrictive upper bound of the mixing efficiency is found by assuming the entire upper layer mixed uniformly (ie. γ is a constant, or not dependent on radius). Using

$$h = h_0 - \frac{\Omega^2}{2g} = \frac{\Omega^2}{2g}(r_c^2 - r^2), \tag{C.4}$$

we find that the total potential energy increase due to the mixing is given by

$$PE_m = 2\pi \int_0^{r_c} \frac{\gamma g \Delta \rho h^2}{2} \, r \, \mathrm{d}r = \frac{\pi \gamma g \Delta \rho r_c^6}{6} \left(\frac{\Omega^2}{2g} \right)^2. \tag{C.5}$$

However, the total mass of mixed fluid is given by

$$M_m = 2\pi \int_0^{r_c} \gamma \Delta \rho h r \, \mathrm{d}r = \pi \gamma \Delta \rho r_c^4 \left(\frac{\Omega^2}{2g} \right). \tag{C.6}$$

and therefore the total potential energy increase is given by

$$PE_m = \frac{1}{6} M_m g h_0. \tag{C.7}$$

which results in a mixing efficiency of 1/6. Theoretically this value could be exceeded by having more mixing towards the centre of the tank (ie. have γ decrease with radius). However, we can use 1/6 as an upper bound for the mixing efficiency, as physically γ will increase with radius, as convection will be concentrated near the front.

Appendix D

Wind-driven advection of isopycnals by a laminar Ekman layer

Let us consider a simple front, where the density field has a constant horizontal and vertical gradient, given by

$$\rho = \rho_0(1 - \alpha x - \beta z). \tag{D.1}$$

Here, the x axis is perpendicular to the front, and is directed towards fluid of reduced density. To maintain such a density field, where the surfaces of constant density (isopycnals) are tilted from horizontal, we require a vertical gradient in the velocity to balance the horizontal gradient in density.

$$v = v_0 + \frac{\alpha g z}{f}, \tag{D.2}$$

This is the thermal wind balance.

Let us consider how the isopycnals are advected when a wind exerts a stress with magnitude τ on the surface of this fluid. We assume the flow is laminar (or a constant eddy viscosity), slow (small Rossby number), and that the wind is sufficiently strong or the front sufficiently weak so that the standard (homogeneous) Ekman layer solutions apply despite the presence of a horizontal density gradient[1]. The steady state horizontal

[1] from equation (7.18), we see that this assumption requires $\frac{\partial \rho}{\partial x} \ll \frac{\rho_o f u_0}{g\delta}$, where u_0 is a typical surface cross-frontal current.

velocities are given by

$$u = \frac{\sqrt{2}}{\rho_0 f \delta} e^{z/\delta} \left[\tau^x \cos(z/\delta - \pi/4) - \tau^y \sin(z/\delta - \pi/4)\right] \tag{D.3}$$

and

$$v = V_0 + \frac{\alpha g z}{f} + \frac{\sqrt{2}}{\rho_0 f \delta} e^{z/\delta} \left[\tau^x \sin(z/\delta - \pi/4) + \tau^y \cos(z/\delta - \pi/4)\right], \tag{D.4}$$

where $\delta = \sqrt{2\nu/f}$ is the Ekman layer thickness and τ^x and τ^y are the components of the wind stress in the positive x and y directions respectively.

The density field will be advected by these velocities according to the density equation

$$\frac{\partial \rho}{\partial t} = -\vec{u} \cdot \nabla \rho, \tag{D.5}$$

where we have ignored diffusion. Substituting the velocity field given by (D.3)-(D.4) yields the time dependent density field:

$$\rho = \rho_0 \left[1 - \beta d \left\{x^* + z^* - \frac{t^* e^{z^*}}{\sqrt{2}} \left(\cos\theta \cos(z^* - \pi/4) - \sin\theta \sin(z^* - \pi/4)\right)\right\}\right], \tag{D.6}$$

where the stars indicate dimensionless parameters, and we have nondimensionalised x by $\beta\delta/\alpha$, z by δ and t by $\beta\rho_0\nu/\alpha\tau$. We have also used θ for the angle between the wind and the x axis, so that $\tau_x = \tau\cos\theta$ and $\tau_y = \tau\sin\theta$. This density field is graphed in Figure D.1 for various wind directions, and at different times.

The vertical gradient in the cross-frontal velocity affects the slope of the isopycnals, and at some time makes more dense water overflow less dense water, which can be seen in the later times of Figure D.1. The formula for the time it takes for the unstable density stratification to form is given by

$$\lambda = -\left.\frac{\partial x}{\partial z}\right|_{\rho=\text{const.},t=0} \left(\frac{\partial u}{\partial z}\right)^{-1}. \tag{D.7}$$

This is a function of depth, but we are only interested in the minimum time it takes for instabilities to occur, which is given by

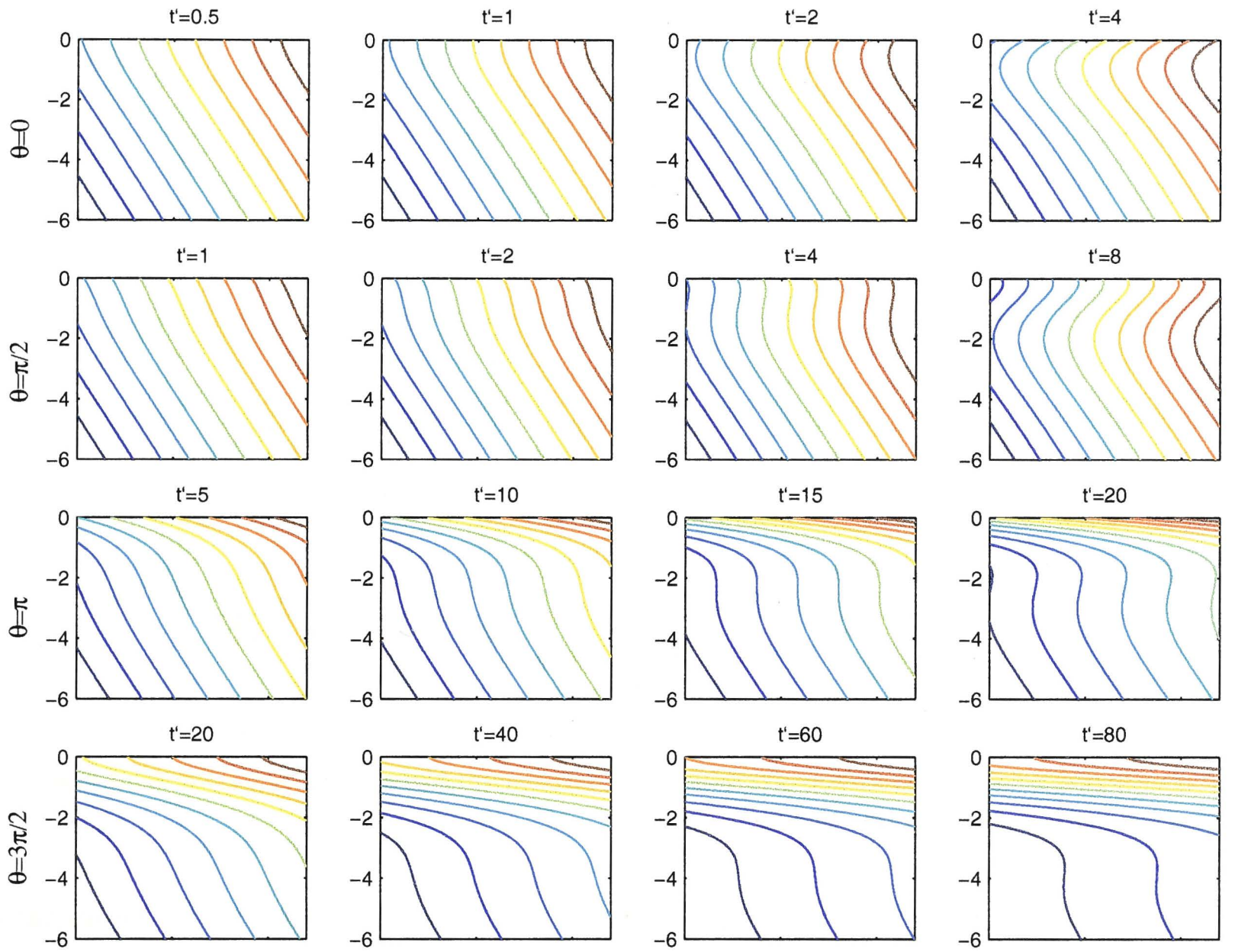

Figure D.1: Advection of the isopycnals by the Ekman layer (D.6). Time increases from left to right, while the angle between the wind direction and the original density gradient increases from top to bottom. The plots have been drawn assuming the Coriolis parameter is positive (ie. northern hemisphere sense)

$$\frac{\lambda}{\lambda_0} = \begin{cases} \sec\theta & -\gamma < \theta < \pi/4 \\ \sqrt{2}\, e^{\theta - \pi/4} & \pi/4 \le \theta \le 2\pi - \gamma, \end{cases}$$

where $\gamma = 1.5571... \approx \pi/2$, and

$$\lambda_0 = \frac{\beta \rho_0 \nu}{\alpha \tau} \tag{D.8}$$

is the characteristic time scale of the problem. If we assume the initial slope of the isopycnal is 1 in 100 ($\alpha/\beta = 0.01$), a constant eddy viscosity of $\nu = 10^{-2}\mathrm{m}^2/\mathrm{s}$ and the wind stress is $\tau = 0.1\,\mathrm{N/m}^2$, then we find $\lambda_0 \approx 10^4\mathrm{s}$, or just under 3 hours, significantly

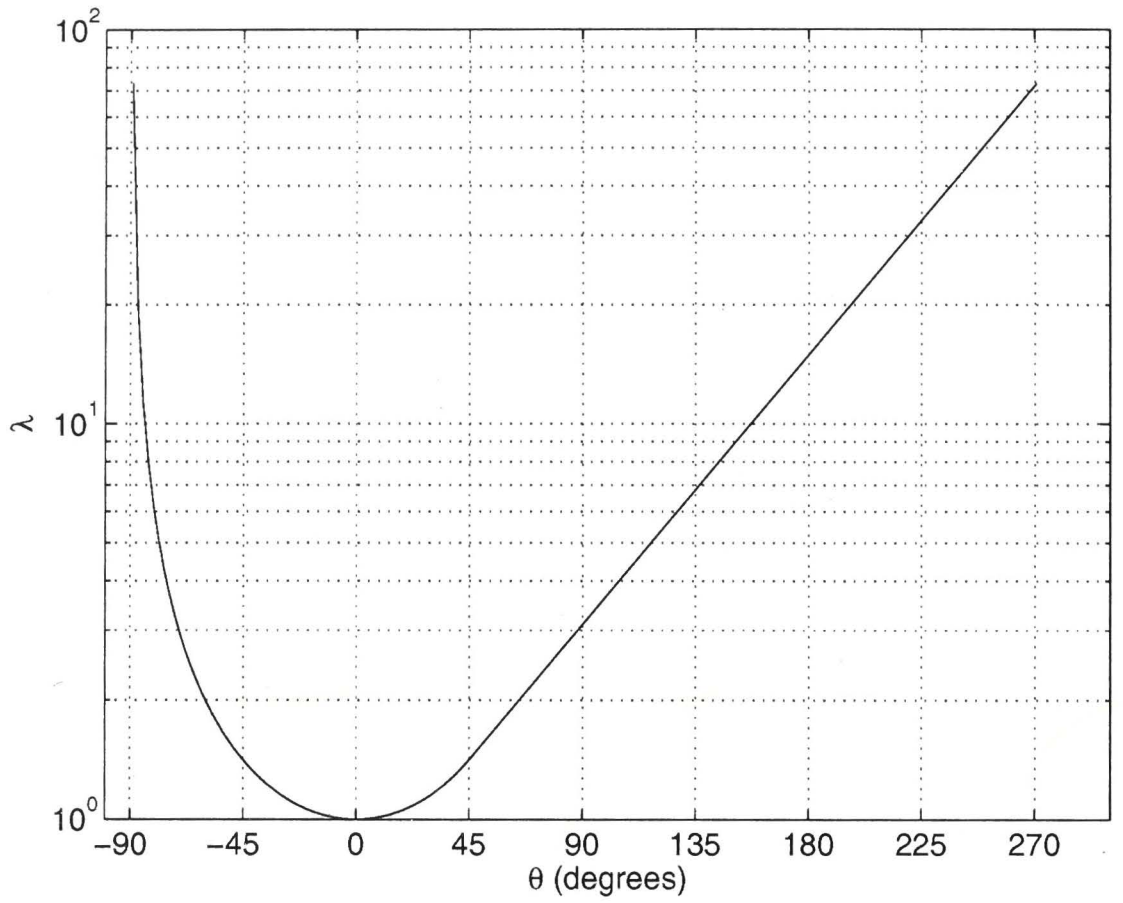

Figure D.2: The unstable density stratification formation timescale (λ), versus the wind angle (θ). The timescale has been normalised by λ_0 (D.8).

faster than the inertial period. Figure D.2 shows the variation of λ with θ. An unstable density profile is formed fastest (in a time λ_0) if the wind direction is perpendicular to the front, from the dense to light side. In the northern hemisphere, if the wind is blowing in a direction parallel to the front, with the higher density water on the left ($\theta = \pi/2$), then $\lambda \approx 3\lambda_0$. A wind in the opposite direction leads to $\lambda \approx 80\lambda_0$.

Bibliography

Atsavapranee, P. and Gharib, M. 1997. Structures in stratified plane mixing layers. *J. Fluid Mech. 342*, 53–86.

Balmforth, N. J., Burbidge, A. S., Craster, R. V., Salzig, J., and Shen, A. 1999. Visco-plastic models of isothermal lava domes. *J. Fluid Mech.* (submitted).

Benton, E. R. and Clarke, A. 1974. Spin-up. *Ann. Rev. Fluid Mech. 6*, 257–280.

Blake, S. 1990. Viscoplastic models of lava domes. In J. H. Fink Ed., *Lava Flows and Domes: Emplacement Mechanisms and Hazard Implications*, Volume 2 of *IAVCEI Proc. in Volcanology*, pp. 88–128. Springer-Verlag.

Boubnov, B. M. and Golitsyn, G. S. 1986. Experimental study of convective structures in rotating fluids. *J. Fluid Mech. 167*, 503–531.

Bryden, H. L. 1983. The southern ocean. In A. Robinson Ed., *Eddies in Marine Science*, pp. 265–277. Berlin: Springer.

Cabot, W., Hubickyj, O., Pollack, J. B., Cassen, P., and Canuto, V. M. 1992. Direct numerical simulations of turbulent convection: I. variable gravity and differential rotation. *Geophys. Astrophys. Fluid Dyn. 53*, 1–42.

Chandrasekhar, S. 1961. *Hydrodynamic and hydromagnetic stability.* Oxford University Press, London.

Coussot, P. and Proust, S. 1996. Slow, unconfined spreading of a mudflow. *J. Geophys. Res. 101*, 25217–25229.

Coussot, P., Proust, S., and Ancey, C. 1996. Rheological interpretation of deposits of yield stress fluids. *J. Non Newtonian Fluid Mech. 66*, 55–70.

DEACON, G. E. R. 1937. The hydrology of the Southern Ocean. *Discov. Rep. 15*, 1–124.

EKMAN, V. W. 1905. On the influence of the earth's rotation on ocean currents. *Arch. Math. Astron. Phys. 2*, 1–52.

ENGLAND, M. H., GODFREY, J. S., HIRST, A. C., AND TOMCZAK, M. 1993. The mechanism for Antarctic Intermediate Water renewal in a world ocean model. *J. Phys. Ocean. 23*, 1553–1560.

FERRIER, A. J., FUNK, D. R., AND ROBERTS, P. J. W. 1993. Application of optical techniques to the study of plumes in stratified fluids. *Dyn. Atmos. Oceans 20*, 155–183.

FINK, J. H. AND GRIFFITHS, R. W. 1990. Radial spreading of viscous-gravity currents with solidfying crust. *J. Fluid Mech. 221*, 485–510.

FINK, J. H. AND GRIFFITHS, R. W. 1992. A laboratory analog study of the morphology of lava flows extruded from point and line sources. *J. Volcanol. Geotherm. Res. 54*, 19–32.

FINK, J. H. AND GRIFFITHS, R. W. 1998. Morphology, eruption rates, and rheology of lava domes: Insights from laboratory models. *J. Geophys. Res. 103*, 527–545.

GILMAN, P. A. 1977. Nonlinear dynamics of Boussinesq convection in a deep rotating spherical shell. *Geophys. Astrophys. Fluid Dyn. 8*, 93–135.

GLIMM, J., GROVE, J. W., LI, X. L., W., O., AND SHARP, D. H. 2001. A critical analysis of Rayleigh-Taylor growth rates. *J. Comp. Phys. 169*, 652–677.

GREENSPAN, H. P. 1968. *The theory of rotating fluids.* Cambridge University Press, Cambridge.

GRIFFITHS, R. W. 2000. The dynamics of lava flows. *Ann. Rev. Fluid Mech. 32*, 477–518.

GRIFFITHS, R. W. AND FINK, J. H. 1993. Effects of surface cooling on the spreading of lava flows and domes. *J. Fluid Mech. 252*, 667–702.

GRIFFITHS, R. W. AND FINK, J. H. 1997. Solidifying Bingham extrusions: a model for the growth of silicic lava domes. *J. Fluid Mech. 347*, 13–36.

HIDE, R. 1956a. The character of the equilibrium of a heavy, viscous, incompressible rotating fluid of variable density. I. General theory. *Quart. J. Mech. Appl. Math. 9*, 22–34.

HIDE, R. 1956b. The character of the equilibrium of a heavy, viscous, incompressible rotating fluid of variable density. II. Two special cases. *Quart. J. Mech. Appl. Math. 9*, 35–50.

HIRST, A. C. AND GODFREY, J. S. 1993. The role of Indonesian throughflow in a global ocean GCM. *J. Phys. Ocean. 23*, 1057–1086.

HULME, G. 1974. The interpretation of lava flow morphology. *Geophys. J. R. Astron. Soc. 39*, 361–383.

HUPPERT, H. E. AND MANINS, P. C. 1973. Limiting conditions for salt-fingering at an interface. *Deep-Sea Res. 20*, 315–323.

IVEY, G. N., WINTERS, K. B., AND COATES, M. J. 2000. Modelling upwelling in the coastal ocean. In G. A. LAWRENCE, R. PIETERS, AND N. YONEMITSU Eds., *Proc. Int. Symp. on Stratified Flow*, pp. 679–684. UBC: Department of Civil Engineering.

JELLINEK, M. A., KERR, R. C., AND GRIFFITHS, R. W. 1999. Mixing and compositional layering produced by convection. part 1. the experiments, and their application to the earth's core and mantle. *J. Geophys. Res. 104*, 17183–7201.

JULIAN, K., LEGG, S., MCWILLIAMS, J., AND WERNE, J. 1996. Rapidly rotating turbulent convection. *J. Fluid Mech. 322*, 243–273.

KERR, R. C. 1994. Melting driven by vigorous compositional convection. *J. Fluid Mech. 280*, 255–285.

LINDEN, P. F. 1979. Mixing in stratified fluids. *Geophys. Astrophys. Fluid Dyn. 13*, 3–23.

LINDEN, P. F. AND REDONDO, J. M. 1991. Molecular mixing in Rayleigh-Taylor instability. part 1: Global mixing. *Phys. Fluids A 3*, 1269–1277.

LISTER, J. R. 1992. Viscous flow down an inclined plane from point and line sources. *J. Fluid Mech. 242*, 631–653.

LISTER, J. R. AND KERR, R. C. 1989. The effect of geometry on the gravitational instability of a buoyant region of viscous fluid. *J. Fluid Mech. 202*, 577–594.

LYMAN, A. W., KOENIG, E., AND FINK, J. H. 2002. Predicting yield strengths and effusion rates of lava domes from morphology and underlying topography. *jgr* (submitted).

MACCREADY, P. AND RHINES, P. B. 1991. Buoyant inhibition of Ekman transport on a slope and its effect on stratified spin-up. *J. Fluid Mech. 223*, 631–661.

MCCARTNEY, M. S. 1977. Subantarctic Mode Water. In M. ANGEL Ed., *A Voyage of Discovery: George Deacon 70th Anniversary Volume*, pp. 103–119. Oxford: Pergamon.

MCCARTNEY, M. S. 1982. The subtropical recirculation of mode waters. *J. Mar. Systems. 40*, 427–464. suppl.

MCDOUGALL, T. J. 1979. Elimination of refractive-index variations in liquid flows. *J. Fluid Mech. 93*, 83–96.

METZL, N., TILBROOK, B., AND POISSON, A. 1999. The annual CO_2 cycle and air-sea CO_2 flux in the sub-Antartic Ocean. *Tellus 51*, 849–861.

NYE, J. F. 1952. Mechanics of glacier flow. *J. Glaciol. 2*, 82–93.

OSMOND, D. I. AND GRIFFITHS, R. W. 2001. The static shape of yield strength fluids slowly emplaced on slopes. *J. Geophys. Res. 106*, 16241–16250.

PATERSON, W. S. B. 1994. *The physics of glaciers* (third ed.). Pergamon, Oxford.

PEDLOSKY, J. 1987. *Geophysical fluid dynamics.* Springer, New York.

PHILLIPS, O. M. 1970. On flows induced by diffusion in a stably stratified fluid. *Deep-Sea Res. 17*, 435–443.

POISSON, A., METZL, N., BRUNET, C., SCHAUER, B., BRES, B., RUIZ-PINO, D., AND LOUANCHI, F. 1993. Variability of sources and sinks of CO_2 in the Western Indian and Southern Oceans during 1991. *J. Geophys. Res. 98*, 22759–22778.

RIBBE, J. AND TOMCZAK, M. 1997. On convection and the formation of Subantarctic Mode Water in the Fine Resolution Antarctic Model (FRAM). *J. Mar. Systems. 13*, 137–154.

RINTOUL, S. R. AND ENGLAND, M. H. 2002. Ekman transport dominates local air-sea fluxes in driving variability of Subantarctic Mode Water. *J. Phys. Ocean. 32*, 1308–1321.

ROSSBY, C. G. 1937. On the mutual adjustment of pressure and velocity distributions in certain simple current systems I. *J. Mar. Res. 1*, 15–20.

ROSSBY, C. G. 1938. On the mutual adjustment of pressure and velocity distributions in certain simple current systems II. *J. Mar. Res. 2*, 239–263.

SCHMITT, R. W. 1999. Spice and the demon. *Science 283*, 498–499.

SOKOLOV, S. AND RINTOUL, S. R. 2002. Structure of southern ocean fronts at 140°E. *J. Mar. Systems. 37*, 151–184.

SOLOVIEV, A., LUKAS, R., AND MATSUURA, H. 2002. Sharp frontal interfaces in the near-surface layer of the tropical ocean. *J. Mar. Systems. 37*, 47–68.

TOMCZAK, M. AND HAO, D. M. 1989. Observations of the time-dependent planetary boundary layer. *Ocean Sciences Institute Report 38*, 196–212.

WAGNER, W. 1961. Bouger-Beer law. In S. G. MONISMITH, J. R. KOSEFF, J. K. THOMPSON, C. A. O'RIORDAN, AND H. M. NEPF Eds., *Encyclopaedic Dictionary of Physics*, pp. 481. New York: Pergamon.

WILSON, S. D. R. 1998. The steady spreading flow of a rivulet of mud. *J. Non Newtonian Fluid Mech. 79*, 77–85.

YOUNGS, D. L. 1984. Numerical simulation of turbulent mixing by Rayleigh-Taylor instability. *Physica D 12*, 32–44.